

NOVEL PROCESSING OF MgO-Y₂O₃ NANOCOMPOSITES FOR
IR WINDOW APPLICATIONS

BY

COLBY MICHAEL BRUNET

A THESIS
SUBMITTED TO THE FACULTY OF

ALFRED UNIVERSITY

IN PARTIAL FULFILLMENT OF THE REQUIREMENTS
FOR THE DEGREE OF

MASTER OF SCIENCE

IN

CERAMIC ENGINEERING

ALFRED, NEW YORK

SEPTEMBER 2012

Alfred University theses are copyright protected and may be used for education or personal research only. Reproduction or distribution in any format is prohibited without written permission from the author.

NOVEL PROCESSING OF MgO-Y₂O₃ NANOCOMPOSITES FOR
IR WINDOW APPLICATIONS

BY

COLBY BRUNET

B.S. ALFRED UNIVERSITY (2009)

SIGNATURE OF AUTHOR _____

APPROVED BY _____ (Signature on File)

DR. OLIVIA A. GRAEVE, ADVISOR

(Signature on File)

DR. WILLIAM CARTY, ADVISORY COMMITTEE

(Signature on File)

DR. C. SCOTT NORDAHL, ADVISORY COMMITTEE

(Signature on File)

CHAIR, ORAL THESIS DEFENSE

ACCEPTED BY _____ (Signature on File)

DR. DOREEN D. EDWARDS, DEAN
KAZUO INAMORI SCHOOL OF ENGINEERING

ACKNOWLEDGMENTS

This thesis would not have been possible without the fearless guidance of my advisor, Dr. Olivia Graeve and the gratuitous assistance from Dr. Scott Nordahl and Dr. Rick Gentilman. Dr. William Carty has been a large influence on my desire to succeed and I would like to thank him for inspiring me throughout the many years in Alfred. A big thanks goes to Gerry Wynick for pushing the limits of everything, every time I see him.

I would like to show my gratitude to everyone at Alfred University for providing a wonderful place to perform research. I am forever indebted to Seth Fuller, who has helped me with my never ending list of tasks. I would especially like to thank Kate Glass and Mike Saterlie for providing their moral support through the roller coaster of life. The members of my lab group have been crucial in providing insight on my project and other aspects of life. Thank you James Kelly, Dr. Raghunath Kanakala, Hoorshad Fathi, Braeden Clark, Kasey Hanson, and Sarai Escalante. Thank you to the University at Buffalo for providing their high resolution imaging equipment and expertise.

I wouldn't be here if it wasn't for my family, giving me all the brains and reasons to stay in school. Michael, Cheryl, Lief, Mallory, and Eli, you guys rock! Grandpa Don, you've always encouraged me and supported me 100%, this one is for you! Finally, it is my honor to be able to confer upon my father, Michael Brunet, the title of "Master Craftsman."

TABLE OF CONTENTS

	Page
Acknowledgments	iii
Table of Contents	iv
List of Tables.....	vii
List of Figures	viii
Abstract	xiii
I INTRODUCTION.....	1
II BACKGROUND	6
A. Synthesis of Magnesium Oxide.....	6
B. Synthesis of Yttrium Oxide	8
C. Synthesis and Importance of the Magnesia-Yttria System.....	9
D. Reverse Micelle Synthesis of Oxide Ceramics in the AOT-Isooctane-Water System.....	11
E. Spark Plasma Sintering of Optical Ceramics.....	14
1. SPS of Optical Ceramic Oxides.....	16
III EXPERIMENTAL PROCEDURE.....	19
A. Solution Synthesis	19
1. Chemical Precipitation.....	19
2. Spray Precipitation.....	20
3. Collection and Washing.....	20
4. Milling	20
5. Reverse Micelle Synthesis	20
6. Heat Treatment	21
B. Spark Plasma Sintering.....	22
1. Conventional Low Pressure SPS	22
2. High Pressure SPS	24
C. Characterization.....	26
1. Powder	26
a. Dynamic Light Scattering	26
i. Precipitation Synthesis	26
ii. Reverse Micelle System Stability	27

b.	Thermogravimetric Analysis.....	27
c.	X-ray Diffraction	27
i.	Phase separation.....	27
ii.	Time-resolved XRD at Varying Temperatures	28
d.	Brunauer, Emmett, and Teller (BET) Surface Area.....	28
e.	High Resolution Imaging.....	28
i.	Transmission Electron Microscopy.....	28
ii.	Scanning Electron Microscopy	28
f.	Density Measurements.....	29
IV	RESULTS.....	30
A.	Chemical Precipitation Synthesis	30
1.	Magnesium Oxide.....	30
2.	Yttrium Oxide.....	34
3.	Magnesium Oxide-Yttrium Oxide Composite.....	36
B.	Spray Precipitation Synthesis	39
C.	Reverse Micelle Synthesis.....	46
1.	Stability Studies	46
2.	Precipitation in Reverse Micelles and Characterization	49
D.	Spark Plasma Sintering.....	56
1.	Low Pressure Sintering.....	56
2.	High Pressure Sintering	57
V	DISCUSSION	61
A.	Reverse Micelle Stability.....	61
B.	Collection and Washing.....	62
1.	Importance of Solvents	62
2.	Inhomogeneity	63
3.	Reverse Micelle Washing	64
C.	Calcination Studies	64
1.	Thermogravimetric Analysis	64
2.	X-ray Diffraction	65
3.	Importance of Calcination Temperature	65
D.	Comparison of Powders by Different Synthesis Methods.....	67
E.	Spark Plasma Sintering.....	69
1.	Low Pressure SPS.....	69

2. High Pressure SPS	70
3. Comparison of Results.....	71
VI SUMMARY AND CONCLUSIONS.....	74
VII FUTURE WORK.....	76
REFERENCES.....	78

LIST OF TABLES

	Page
Table I. List of Chemicals Used and Their Suppliers.....	19

LIST OF FIGURES

	Page
Figure 1. Diagram of reverse micelle water domains in a continuous oil phase.	4
Figure 2. Spark plasma sintering mechanism, in which pressure and current are simultaneously applied for the fast sintering of powders.	4
Figure 3. Phase diagram of the magnesia-yttria system. ⁵⁹	10
Figure 4. The effect of particle size and morphology of GeO ₂ based on varying water-to-surfactant ratio during synthesis. ⁹⁵	12
Figure 5. Tangling of surfactant chains during centrifugation leading to agglomeration. ¹⁰⁰	14
Figure 6. High pressure SPS die. ¹²⁸	18
Figure 7. Picture of the spark plasma sintering apparatus.	23
Figure 8. Normal graphite die setup.	23
Figure 9. Schematic of a sintering profile for the normal graphite die setup.	24
Figure 10. Die arrangement for high pressure SPS experiments.	25
Figure 11. Schematic of the sintering profile for high pressure experiments.	26
Figure 12. TGA plot showing the weight loss with respect to temperature, indicating decomposition temperature of magnesium hydroxide into magnesium oxide.	31
Figure 13. XRD pattern showing the crystallinity and mineralogy of heat-treated MgO. Peaks indicated by circles are representative peaks for the MgO PDF 00-045-0946.	31
Figure 14. DLS data of MgO dispersed in water, acetone, and ethanol.	32

Figure 15. DLS of MgO synthesized by chemical precipitation before and after heat treatment.....	33
Figure 16. TEM of as-synthesized and heat-treated MgO synthesized by chemical precipitation method.	33
Figure 17. DLS data of as-synthesized and heat-treated Y ₂ O ₃ synthesized by chemical precipitation method.....	34
Figure 18. TGA plot showing the weight loss with respect to temperature, indicating decomposition temperature of yttrium hydroxide into yttrium oxide.....	35
Figure 19. XRD pattern showing the purity, crystallinity, and mineralogy of heat-treated Y ₂ O ₃ synthesized by chemical precipitation method. Peaks indicated by circles are representative peaks for the Y ₂ O ₃ PDF 00-041-1105 with intensities of four or greater.....	35
Figure 20. DLS data of as-synthesized and heat-treated MgO-Y ₂ O ₃ composite powders synthesized by chemical precipitation method.....	36
Figure 21. TGA plot showing the weight loss with respect to temperature, indicating decomposition temperature of the composite hydroxides into the MgO-Y ₂ O ₃ composite powders synthesized by chemical precipitation.	37
Figure 22. XRD pattern showing the purity, crystallinity, and biphasic nature of heat-treated MgO-Y ₂ O ₃ composite powders. Peaks indicated by circles are representative peaks for the Y ₂ O ₃ PDF 00-041-1105 with intensities of eight or greater. Peaks indicated by stars are representative peaks for the MgO PDF 00-045-0946.....	38
Figure 23. TEM micrographs of as-synthesized and heat-treated MgO-Y ₂ O ₃ composite powders synthesized by normal precipitation, showing morphology.....	38
Figure 24. DLS of as-synthesized and heat-treated MgO-Y ₂ O ₃ composite powders synthesized by spray precipitation.....	39
Figure 25. TGA plot showing the weight loss with respect to temperature, indicating decomposition temperature of the composite hydroxides into MgO-Y ₂ O ₃ composite powders synthesized by spray precipitation.....	40

Figure 26. XRD pattern showing the purity, crystallinity and biphasic nature of heat-treated MgO-Y ₂ O ₃ composite powders synthesized by spray precipitation. Peaks indicated by circles are representative peaks for the Y ₂ O ₃ PDF 00-041-1105 with intensities of eight or greater. Peaks indicated by stars are representative peaks for the MgO PDF 00-045-0946.....	40
Figure 27. In-situ XRD patterns of as-synthesized MgO-Y ₂ O ₃ composite powders synthesized by spray precipitation technique. Circled peaks indicate peaks corresponding to a particular phase and mineralogy as shown in the legend.....	41
Figure 28. Graph displaying the crystallite growth, from XRD, with respect to temperature.	42
Figure 29. TEM micrographs of as-synthesized and heat-treated MgO-Y ₂ O ₃ composite powders synthesized by spray precipitation, showing morphology.	43
Figure 30. SEM of sintered specimen showing inhomogeneity as a result of poor dispersion of starting powders.....	44
Figure 31. Graph showing the relative amounts of MgO and Y ₂ O ₃ as collected from the top and bottom of centrifuge vials.....	44
Figure 32. DLS after milling, before and after heat treatment of the MgO-Y ₂ O ₃ composite powders synthesized by spray precipitation.	45
Figure 33. SEM of sintered specimen showing improved homogeneity after milling of the MgO-Y ₂ O ₃ composite powders synthesized by spray precipitation.	45
Figure 34. DLS data showing the effect of ion concentration of magnesium nitrate on the size of a reverse micelle in the AOT-isooctane-water system.	46
Figure 35. Graph displaying the change of micelle size with varying magnesium nitrate salt concentrations in the AOT-isooctane- water system with a $\omega_o=10$	47
Figure 36. Representative picture of unstable reverse micelle solutions, for a molarity greater than 1, showing water coalescence on the bottom of beaker.....	48

Figure 37. The effect of yttrium nitrate concentration on micelle size for $\omega_0=10$, $\omega_0=12.5$, and $\omega_0=15$. Arrows pointing to the concentration at which the solution is unstable for the particular ω_0	48
Figure 38. Change of micelle size after MgO-Y ₂ O ₃ composite synthesis at 0.1 M, 0.2 M, and 0.3 M.....	49
Figure 39. The influence of washing cycles on the mean particle size of synthesized MgO-Y ₂ O ₃ composite powders synthesized by reverse micelle technique. (a) before calcination (dried), (b) after calcination at 1000°C.	50
Figure 40. TGA plot showing the weight loss with respect to temperature, indicating decomposition of the composite hydroxides into MgO-Y ₂ O ₃ composite powders synthesized by reverse micelle technique.	51
Figure 41. In-situ high-temperature (ranging from room temperature to 1000°C) XRD patterns of as-synthesized MgO-Y ₂ O ₃ composite powders synthesized by reverse micelle technique. Circled peaks indicate peaks corresponding to a particular phase and mineralogy as shown in the legend.....	52
Figure 42. Graph displaying the crystallite growth, from XRD, with respect to temperature.	53
Figure 43. XRD pattern of calcined MgO-Y ₂ O ₃ composite powders synthesized by reverse micelle technique calcined at 1000°C for one hour. Peaks indicated by circles are representative peaks for the monoclinic phase of Y ₂ O ₃ . Peaks indicated by stars are representative peaks for the MgO PDF 00-045-0946.....	53
Figure 44. DLS of as-synthesized and heat-treated (600°C and 1000°C) MgO-Y ₂ O ₃ composite powders synthesized by reverse micelle technique.....	54
Figure 45. TEM micrographs of (a) as-synthesized and (b) 600°C and (c) 1000°C calcined MgO-Y ₂ O ₃ composite powders synthesized by reverse micelle technique.	55
Figure 46. TEM micrograph of a composite powder particle with the size of a reverse micelle.	55

Figure 47. BSE SEM of SPS sintered composite, synthesized by spray precipitation. A temperature of 950°C and pressure of 75 MPa was used. Density is 85% and grain size is about 90 nm.....	56
Figure 48. Fracture surface SEM of MgO-Y ₂ O ₃ composite powders synthesized by spray precipitation, sintered using high-pressure SPS technique at (a) 300 MPa, (b) 350 MPa, (c) 400 MPa, (d) 450 MPa, and (e) 500 MPa.....	58
Figure 49. Fracture surface SEM of MgO-Y ₂ O ₃ composite powders synthesized by reverse micelle technique, sintered using high-pressure SPS technique at 500 MPa (a) small grain microstructure (b) mixed microstructure.....	59
Figure 50. Graph showing the effect of pressure on the density of high-pressure SPS sintered samples.	60
Figure 51. Graph showing the effect of pressure on the final grain size of high-pressure SPS sintered samples.....	60
Figure 52. Diagram of a reverse micelle shrinking in size due to charge effects, eventually causing an unstable micelle solution.....	61
Figure 53. Proposed mechanisms of agglomeration when surfaces of a hydroxide contain water versus ethanol. ¹³¹	63
Figure 54. Change in mean particle size before and after characterization for (1.) MgO by chemical precipitation (2.) Y ₂ O ₃ by chemical precipitation (3.) MgO-Y ₂ O ₃ by chemical precipitation (4.) MgO-Y ₂ O ₃ by spray precipitation (5.) MgO-Y ₂ O ₃ by spray precipitation, milled (6.) MgO-Y ₂ O ₃ by reverse micelle synthesis.....	66
Figure 55. Comparison of particle size to crystallite size for (1.) MgO by chemical precipitation (2.) Y ₂ O ₃ by chemical precipitation (3.) MgO-Y ₂ O ₃ by chemical precipitation (4.) MgO-Y ₂ O ₃ by spray precipitation (5.) MgO-Y ₂ O ₃ by reverse micelle synthesis (Note: Y ₂ O ₃ crystallite size was not measured)	67
Figure 56. DLS comparison of the final composite powders synthesized by all three methods.....	68

ABSTRACT

Polycrystalline ceramics used for infrared transparent windows have a great advantage over their single crystal counterparts. In these materials, grain size plays an important role on the transparency and mechanical durability of the windows. Through the use of unique nanomaterial processing techniques, a magnesium oxide - yttrium oxide nanocomposite material has been studied.

The main purpose of this study was to establish a correlation between powder characteristics and the final grain size of a sintered compact. Powders synthesized by two methods were studied. First, a common hydroxide precipitation method was used to synthesize the MgO-Y₂O₃ nanocomposite powders. Second, a reverse micelle synthesis method was used to prepare the MgO-Y₂O₃ nanocomposite powders. The stability of the reverse micellar system was explored and correlations were established between the solution molarities and successful powder synthesis. It was discovered that a molarity of 0.3 M in the AOT-isooctane-water system was within stable parameters. Both methods were successful in the synthesis of powders with mean particle sizes less than 100 nm.

After synthesis, the powders were characterized by X-ray diffraction (XRD) for phase, purity, and crystallite size; dynamic light scattering (DLS) for particle size; transmission electron microscopy (TEM) for powder morphology; and BET for surface area. The powders were then consolidated.

The sintering of the powders was accomplished by spark plasma sintering (SPS), using high pressures, between 300 and 500 MPa. Densities were measured by using an immersion technique. High resolution scanning electron microscopy (SEM) was performed on fracture surfaces to analyze grain size. The high pressure SPS method resulted in densities of approximately 90% of theoretical and final grain sizes of about 60 nm.

INTRODUCTION

Many materials have been successfully used for infrared (IR) sensor protection applications, however, they can often be difficult to manufacture and/or expensive. Cheaper and easily processed materials can be processed into IR transparent windows and domes, but their durability and/or stability is often poor for the conditions these windows must endure.¹⁻⁷ Windows and domes on missiles are more than likely to be exposed to abrasive materials while flying through the air at high velocity, which can cause erosion and other damage on the surface of the window. Surface roughness can contribute to a loss of IR transmission and can also result in larger more catastrophic failure of the window component.

Since materials will only transmit a range of IR radiation, the proper material must be chosen for a given application. For missile guidance systems the 3-5 μm range of the IR spectrum is the range in which the homing device of passive IR 'heat seeking' missiles is designed to operate. Detectors will recognize the IR signature of the target, perhaps an aircraft, since this is the range of radiation given by the jet engine exhaust plume. For greater thermal tracking devices, the detector must operate within the 8-12 μm range. The range of 8-12 μm is known as the "thermal imaging" region.⁸ This is the region in which sensors can obtain a completely passive picture based on only thermal emissions and requiring no external light.

An extensive review of materials used for IR windows has been conducted by Harris.¹ This review focuses on the properties of 3-5 μm infrared-transmitting window materials, with an emphasis on durable materials for applications in environments involving moisture, solid and liquid particle impact, elevated temperatures and rapid heating rates. The optical, mechanical, and thermal properties are compared for MgF_2 , aluminum oxynitride, sapphire, spinel, MgO , Y_2O_3 , calcium aluminate, SiO_2 , CaF_2 , LiF , ZnS , ZnSe , GaAs , GaP , Si and Ge .

Magnesium oxide can be used as an IR window material, since it transmits IR radiation within the range of 3-5 μm and begins absorbing radiation around 6 μm . The mechanical properties, however, tend to be lower than some of the other choice materials.

From Knoop hardness indentation, MgO has a hardness of 690 kg/mm².⁹ The coefficient of thermal expansion (CTE) is $11 \times 10^{-6} \text{ K}^{-1}$, which has an impact on the thermal shock resistance.

Yttrium oxide is another common material used for IR window applications. The IR transparency range is similar to MgO. Ytria will transmit radiation between 3-5 μm . The Knoop hardness has been observed up to 720 kg/mm², similar to the hardness of MgO, and the CTE is around $6.5 \times 10^{-6} \text{ K}^{-1}$.¹⁰

Due to the lower CTE of Y₂O₃, making a composite of MgO and Y₂O₃ will improve the thermal shock resistance of the window. A bi-phase compact will aid in the hindrance of grain growth during sintering. In a composite material, composed of materials with a large index of refraction difference, the grain size plays an important role on the IR transmission behavior. It is known that the lower range of IR transmission can be extended in media that have a feature size of less than one-twentieth the wavelength of interest. In the case of these consolidated polycrystalline materials, the feature size is the diameter of the grains. For a polycrystalline isotropic single-phase material, the optical properties are not impacted by grain size. The optical properties of a polycrystalline anisotropic material will behave similarly to those of a composite material, in that grain size will have an effect on the transmission range.

Nanomaterials are known to possess novel or improved properties due to enhancements associated with grain-boundary/surface phenomena. The materials of interest may exhibit enhanced mechanical, magnetic, high-temperature, and/or optical properties, as well as excellent catalytic properties. Seal *et al.*¹¹ and Mayo *et al.*¹² discuss the challenges that must be overcome for wide-spread use of nanomaterials. Namely, new manufacturing techniques are required for these materials that are both economical and capable of producing large amounts of nanopowders, proper handling and storage procedures need to be developed, and investigation of current sintering techniques as well as development of new sintering techniques are required.

Mayo *et al.*¹² describe the scale-up of two synthesis processes used for making larger quantities of nano-powder, namely gas phase condensation and wet-chemical techniques. Both processes can produce large quantities and are easily scalable. Gas phase condensation is often done in a flame, requiring oxygen to burn, which is beneficial

for the formation of oxides. The two most popular wet-chemical techniques are precipitation of hydroxides from salts and alkoxide hydrolysis (sol-gel synthesis). Precipitation is, by far, one of the simplest methods to achieve nano-size particles. Magnesium oxide, doped with zinc oxide, has been precipitated in water and ethanol, but at temperatures around 80°C to change reaction kinetics.¹³

Reverse micelle synthesis is a recent novel approach to achieve nano-size particles.^{14,15} Other specific techniques proven to be capable of synthesizing nanocrystalline oxide ceramics include chemical vapor synthesis¹⁶ and combustion synthesis,¹⁷ to name a few.

Reverse micelle synthesis is a technique that is being utilized because it can produce particle sizes in the nanoregime. This synthesis technique involves water, oil, and surfactant. Without the surfactant, these micellar structures cannot form.¹⁸ The surfactant surrounds the aqueous phase. It accomplishes this by surrounding the droplets of water with a hydrophilic head and a hydrophobic tail. If a greater quantity of water were present, the small oil droplets would be surrounded by the tails of the surfactant, creating a microemulsion.¹⁹ Since the purpose is to produce reverse micelles, the oil will make up the majority of the liquid phase. The surfactant will then surround the water droplets with the heads facing inward. These reverse micelles are much smaller, and the size is much easier to control. Figure 1 shows water domains with magnesium ions stabilized in a spherical arrangement by a surfactant within an oil matrix.

After synthesis, part of the challenge is keeping these materials nanograined when consolidated into a bulk specimen. In many cases, traditional sintering techniques are not suitable for doing this. Spark plasma sintering uses the simultaneous application of uniaxial pressure and an electric current, which creates rapid Joule heating and densification, schematically shown in Figure 2. The electric current has been shown to modify the reactivity of several solid-state systems, but is not a well understood phenomenon.²⁰ Important parameters include the peak temperature, heating rate, and the applied pressure. The work of Anselmi-Tamburini *et al.*²¹ showed that in the case of zirconia, the temperature was significant in determining densification and the final grain size. The heating rate and sintering time appeared to have little effect on the final density or the grain size. The pulsing pattern also had no influence, agreeing with the work of

Chen *et al.*²² The applied pressure had a significant influence on density, but not on the grain size in their study.

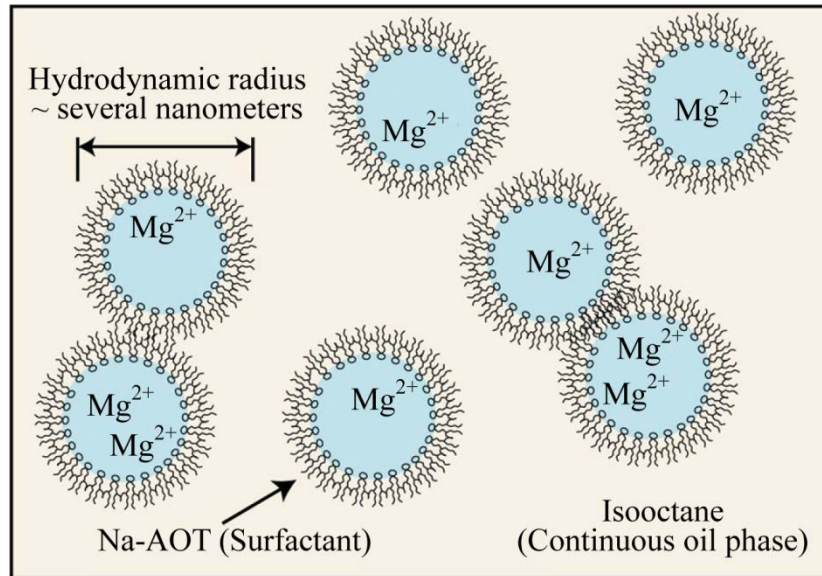


Figure 1. Diagram of reverse micelle water domains in a continuous oil phase.

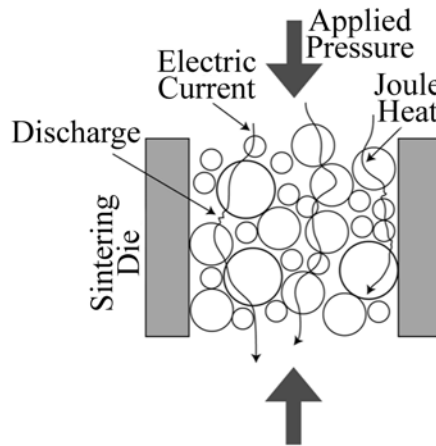


Figure 2. Spark plasma sintering mechanism, in which pressure and current are simultaneously applied for the fast sintering of powders.

Agglomeration has proven to be a problem with nano-sintering.^{23,24} This problem has been mostly addressed through better synthesis and processing of nano-powders. This may not be as much of an issue with spark plasma sintering, since under pressure-sintering, large pores can be eliminated rapidly. It has been shown that it is not possible

to attribute the closing of the inter-agglomerate pores to simply breaking of the agglomerates under pressure.¹² In the meantime, it has become apparent that the time of pressure application appears to be important. In some cases, high density can be achieved more easily if the pressure is applied after the sintering temperature has been achieved, since the sample will be more susceptible to plastic deformation at higher temperatures. However, other material systems may behave differently depending on their properties (e.g. temperature, strain rate, grain size, etc.).

When the nano-structure of materials is retained through consolidation, the properties are often improved. In particular, unusually high strengths can be achieved while maintaining reasonable ductility and toughness. Dutkiewicz *et al.*²⁵ showed that by decreasing the crystal size below 80 nm in titanium, a Ti-Ta-Nb alloy was capable of achieving yield strengths that were higher by a factor of 3 compared to the original material. In the case of nanocrystalline zirconia/spinel composites, strength was increased by a factor of 2.5 to a value of 2.2 GPa.²⁶ SPS of $ZrO_2(Y_2O_3)/Al_2O_3$ composites resulted in a nano-structured material with a hardness value of approximately 14 GPa, fracture toughness around $6.6 \text{ MPa}\cdot\text{m}^{1/2}$, and flexure strengths around 1 GPa.²⁷ Another study on zirconia showed that the best hardness and fracture toughness results were obtained for SPS conditions yielding the smallest grain size of less than 100 nm.²⁸

BACKGROUND

A. Synthesis of Magnesium Oxide

Historically, magnesium oxide is obtained from processing magnesite-containing materials, such as dolomite. The magnesium carbonate, from these materials, can be decomposed by thermally treating to temperatures above 400°C. These starting materials often contain impurities, so various chemical methods have been developed to leach and separate the impurities.²⁹⁻³³ Seawater is another magnesium containing source and can be used for the production of magnesium oxide.^{34,35} Magnesium metal can be another precursor material used in the production of magnesium oxide. The metal can be oxidized in air,^{34,36-38} or dissolved in an acid and precipitated.³⁹ Other methods capable of synthesizing magnesium oxide are from thermal decomposition of salts,⁴⁰ sol-gel,⁴¹⁻⁴⁴ and molten salts.⁴⁵

The most popular route for the production of magnesium oxide is the wet chemical precipitation method. Magnesium cations in solution combine with an oxygen containing anion, to form a solid precipitate, which can be collected and further processed, if needed. Magnesium salts, such as magnesium nitrate,^{32,46-50} magnesium chloride,⁴⁹⁻⁵¹ magnesium sulfate,^{32,49} and magnesium acetate,³² are dissolved in an aqueous solution or ethanol. An alkaline solution such as sodium hydroxide,⁵⁰ ammonium hydroxide,^{32,46,48,50,51} ammonium hydroxide carbonate,⁴⁷ or sodium carbonate,⁴⁹ is added to precipitate magnesium hydroxide or magnesium carbonate.

Additions of surfactants and polymers during the precipitation process can yield various final morphologies. The addition of cetyl trimethylammonium bromide, CTAB, leads to the formation of ordered arrays, namely platelets of 1 μm diameter and 100 nm thick.⁵² The addition of polyethylene glycol results in nanoplates of thickness 20 nm and a length of 100 nm, with the 001 plane being the larger surface.^{48,51} Additions of polyvinyl alcohol lead to nanosized platelet-like structures, but introduces porosity.⁴⁶ An addition of poly(vinylpyrrolidone) leads to flowerlike structures with high surface area.⁵³

Precipitation without the use of polymer additives can yield varying results in powder morphology as well. Final structures depend on the precursor materials used. In

the case of precipitation from magnesium salts and ammonium hydroxide, platelet structures are likely to form. Specific surface area and apparent density of final powders differs slightly. The trend in surface area and apparent density from magnesium containing salts is as follows: sulfate > nitrate > acetate, according to Alvarado *et al.*³² Another study on the effect of precursor materials by Henrist *et al.*⁵⁰ confirms platelet-like morphology through the use of nitrates, chlorides, and ammonium hydroxide. They find that a sulfate precursor leads to a “harder” agglomerated powder. Driving the synthesis with sodium hydroxide promotes a globular, cauliflower-like agglomerated powder. The work of Llama *et al.*⁴⁹ on catalytic properties of magnesium hydroxide, shows that calcined precipitates from magnesium nitrate, sulfate, and chloride have similar specific surface areas, when the synthesis is driven by sodium carbonate, but porosity is rather apparent.

There has been much research on the heat treatment temperature for the decomposition of magnesium hydroxide to magnesium oxide. Heat treatment temperature and conditions are important for obtaining high purity magnesium oxide free from hydroxide impurities. The most common characterization techniques used to study the decomposition are differential thermal analysis/thermo-gravimetric analysis (DTA/TGA),^{32,33,51,52} Fourier transform infrared spectroscopy (FTIR),^{48,49,52} and X-ray diffraction (XRD).^{32,33,48-52} DTA and TGA are often run simultaneously, and provide insight on weight loss and heat flow. FTIR analysis is able to distinguish particular bonds in a material, by obtaining absorption spectra affected by characteristic bond vibrations. These absorption spectra could, for instance, provide insight on the amount of hydroxide impurities in a sample, by studying the intensity of the hydroxide bond absorption peak. XRD characterization is useful for determining the phase purity of a specimen. Materials have a unique diffraction pattern depending on their crystal structure, therefore one may determine the phase present given a distinctive pattern. XRD can be used to confirm the phase purity and crystallite size.

A normal TGA curve will show an endothermic peak at temperatures less than 200°C, which corresponds to a dehydration process of surface adsorbed water. A second endothermic peak is seen at temperatures between 350 and 500°C. Depending on precursor materials used, this peak corresponds to the decomposition reaction. The

theoretical weight loss for the $\text{Mg}(\text{OH})_2$ to $\text{MgO}+\text{H}_2\text{O}$ decomposition reaction, which should occur at these temperatures, is 30.8%, confirmed by TGA analysis.^{32,33,51,52} This method is best used in conjunction with XRD, to confirm the complete decomposition and purity of final product.

The heat treatment temperature plays an important role on the powder's processing behavior and ultimately, the sinterability. Too high of a calcination temperature will lead to a significant amount of crystallite growth and particle necking (agglomeration), which can be unfavorable in certain situations. It has been found that heat treatment temperatures between 600 and 1000°C are adequate.^{32,33,54}

B. Synthesis of Yttrium Oxide

Yttrium oxide can also be synthesized by precipitation methods. This has been proven successful by many researchers.⁵⁵⁻⁵⁸ This method of synthesis involves the dissolution of large yttrium oxide particles in nitric acid and subsequent addition of a base to precipitate yttrium hydroxide. This hydroxide can then be calcined for the decomposition into Y_2O_3 with much smaller particle sizes than the starting material. Tool and Cordfunke⁵⁵ discovered that the precipitating agent (ammonium hydroxide or ammonium carbonate) and concentration plays a large role in the sinterability of the powder. This is likely due to difference in particle size between the powders prepared using the two different precipitating agents. However, the authors did not explore this effect.

Huang *et al.*⁵⁶ performed synthesis using the same method as described previously, however, they examined the particle size and morphology of the powders. They determined that pH during synthesis and calcination temperature plays an important role on the particle size and effectively on the sintering behavior. By using a pH of 8, particles had a narrow size distribution and were loosely agglomerated. Using a pH of 10 resulted in larger particles, large size distribution and severe agglomeration. A calcination temperature of 1000°C was determined to be optimum. Temperatures less than this resulted in powders so fine they were difficult to press to high green density. Temperatures greater than 1000°C resulted in large particles, broad size distributions, and

severe agglomeration. Having severe agglomeration lead to the formation of large pores during sintering.

Wen *et al.*⁵⁸ studied the effect of mixing process on the particle size and morphology of yttria. They discovered that when adding the precipitating agent to the solution containing the metal ions the particles were platelet-like and agglomerated. When reversing the mixing process the precipitated particles were less platelet-like, larger, and more agglomerated. In most cases, platelet-like powders sintered worse than spherical powders, due to packing inefficiencies. However, in this case, the platelet-like structure (made by adding the precipitating agent to the metal ion containing solution) did not seem to impact the sinterability of the powders, in fact they sintered better. This could be due to the small particle size and less severe agglomeration.

Sohn *et al.*⁵⁷ discovered that concentration of yttrium ions during synthesis affects the final particle size and morphology of the precipitated yttria. By using molarities between 0.005 and 0.025 M the final particle size is 65 to 140 nm, relatively uniform in size, and spherical. Increasing the concentration lead to agglomerated particles with a much larger particle size.

In summary, pure and sinterable yttria can be synthesized by simple precipitation methods. Precursor types, concentrations, and calcination temperature, are parameters that must be controlled for the fabrication of desired powders.

C. Synthesis and Importance of the Magnesia-Yttria System

A composite material is comprised of more than one phase material. These materials must not be soluble in one another and maintain minimum interaction. Phase diagrams are the most valuable resource when determining the interactions of multiple materials. The phase diagram for MgO and Y₂O₃ can be seen in Figure 3.⁵⁹ It shows that under 2110°C MgO and Y₂O₃ does not interact to form a significant solid solution. This means there is little interaction of the two phases, which makes it possible to form a composite.

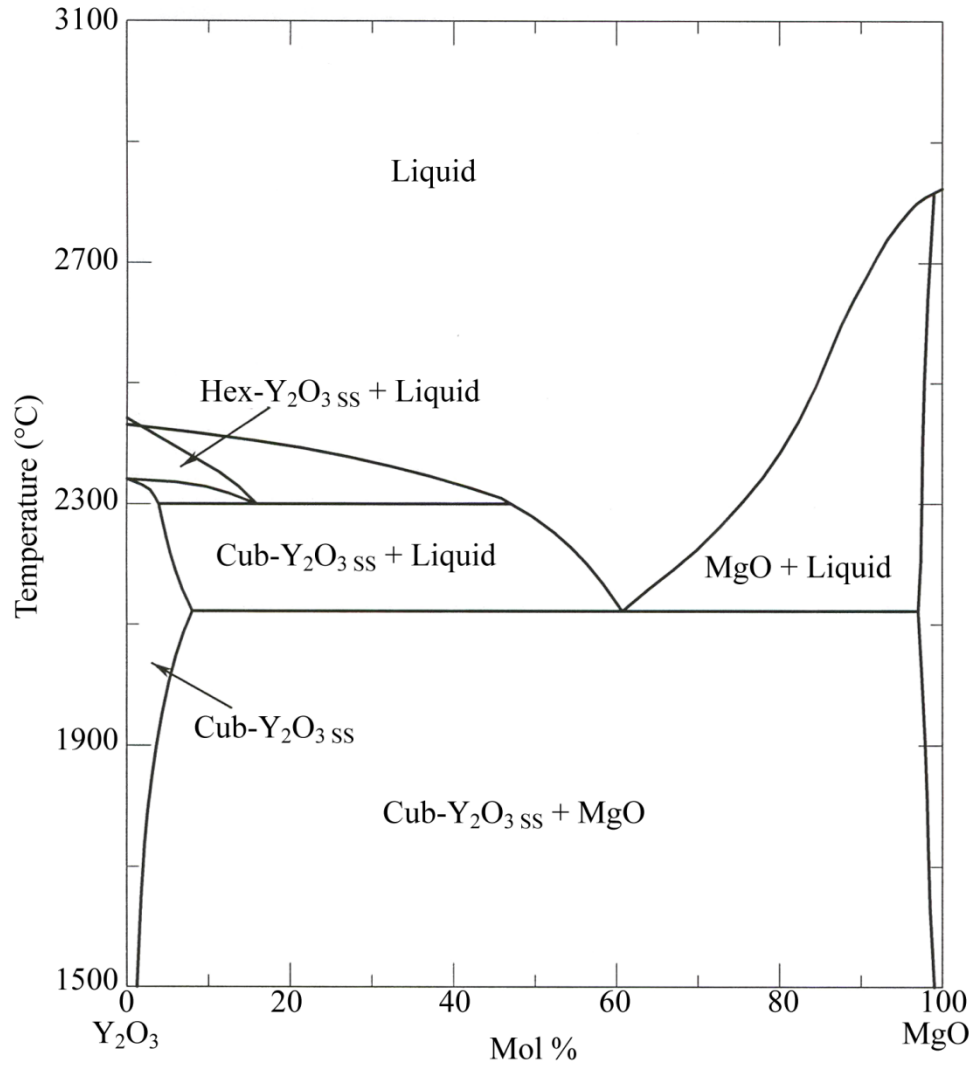


Figure 3. Phase diagram of the magnesia-yttria system.⁵⁹

The methods used for synthesizing nano-composite oxide ceramic systems are many and include spray pyrolysis, hydrothermal synthesis, chemical vapor deposition, solid-state reactions, hydroxide precipitation, combustion, thermal decomposition, and sol-gel. Some of these methods can be costly, complex, have low yields, or be difficult to control. There are significant challenges that must be overcome to provide precise control over composition, phase homogeneity, particles size distributions, and morphology.⁶⁰

The most common method utilized for the production of MgO/Y₂O₃ nano-composite powders is a combination of sol-gel and thermal decomposition.⁶¹⁻⁶⁵ Four

precursor materials are used: magnesium nitrate, yttrium nitrate, magnesium acetate, and yttrium acetate. A combination of two out of the four precursor materials, in the desired mixture ratio and dissolved in water will allow for ionic level mixing. The solution is then dried and calcined to decompose the precursor materials into an oxide.⁶¹⁻⁶⁴ This method produces a nanocomposite with extremely good mixing, however, the powders are agglomerated. This agglomeration appeared not to create difficulties during sintering to densities of 99.5% by hot isostatic pressing.⁶³ This leads one to assume that the agglomeration is soft and can be easily eliminated under high pressures.

Advantages to using a nano-composite are made evident by the improvement of the mechanical properties and the preservation of optical properties of a consolidated specimen. This has been seen in the case of the MgO/Y₂O₃ system, where the mechanical properties are greater than that of each individual constituent and the optical properties are maintained.^{61,62,66-70} By intermixing two phases, the grains of each phase will pin the boundaries of the other phase, thus inhibiting grain growth during high temperature consolidation.⁷¹

D. Reverse Micelle Synthesis of Oxide Ceramics in the AOT-Isooctane-Water System

Reverse micelle systems have been studied for many years, as made apparent through the multiple reviews available.⁷²⁻⁷⁷ The reverse micelle system, consisting of water droplets stabilized in an isooctane oil matrix through the use of sodium sulfosuccinate (AOT) surfactant, has been studied extensively.⁷⁸⁻⁸²

Due to the extremely small size and dynamic nature of a reverse micelle, obtaining an understanding of the system *in-situ* is difficult, therefore certain characterization techniques must be used. One such method is to synthesize a material inside the micelle, and study its structure and morphology after removal from the system. This method is possible, but due to the dynamic character of the system throughout the synthesis process, it is difficult to extract important information. One method that is becoming essential to the study of reverse micelle systems and microemulsions is dynamic light scattering (DLS).⁸³⁻⁸⁸ This technique allows for the dynamic testing of micelle sizes within the liquid system.

In all reverse micelle systems there are many factors that can control the behavior of a reverse micelle. The major parameters that can influence one particular system's behavior are water-to-surfactant ratio and ion concentration within the water droplet. Many have studied and confirmed the fact that water-to-surfactant ratio can change the size and shape of the particles.^{72-77,83,89-93} Gardner *et al.*⁹⁴ have performed molecular dynamic simulations to study reverse micelle size and shape as effected by the water-to-surfactant ratio of the AOT-isooctane-water reverse micelle system. All have found that when the amount of water increases in the system, the reverse micelle size increases. Bohidar *et al.*⁸³ performed a controlled DLS experiment displaying this trend.

Characterizing the change in shape of a micelle is a difficult task. The simplest way is by performing a precipitation reaction in the micelle and studying the resulting microstructure of the product. It has been seen that a change in water-to-surfactant ratio also plays a role on the shape of a precipitated material. It was discovered in the work by Chen *et al.*,⁹⁵ on the synthesis of GeO₂, that a low water-to-surfactant ratio results in small spherical particles, increasing the value increased the size of the particles, and increasing even further resulted in rod-like particles, as illustrated in Figure 4.

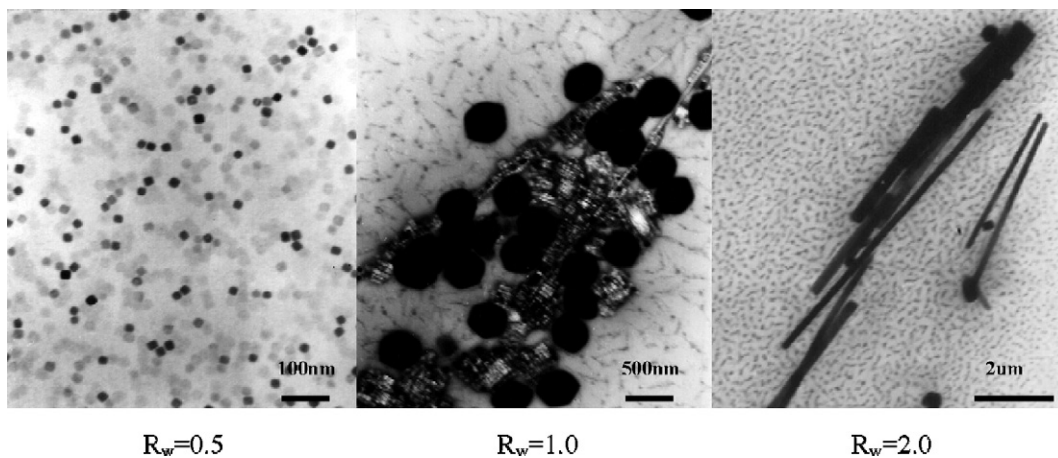


Figure 4. The effect of particle size and morphology of GeO₂ based on varying water-to-surfactant ratio during synthesis.⁹⁵

Although the majority of reverse micelle synthesis research has been focused on metals, oxides have been synthesized by this technique as well.^{14,84-88,91,93-99} Some of the

oxides that have been synthesized successfully include ZrO_2 ,^{84,85,94,100} GeO_2 ,^{93,95} Y_2O_3 ,^{14,88} ferrites,^{86,91,97} TiO_2 ,⁹⁶ BaTiO_3 ,⁸⁸ SnO_2 , CeO_2 , and ZnO .⁸⁵

One particular study of interest was performed by Sun *et al.*⁹⁸ where they were able to synthesize a $\text{WO}_3:\text{ZrO}_2$ biphasic material using the AOT-isooctane-water system. This procedure was identical to a normal synthesis involving only one precipitant. However, it included another reactant for the synthesis of the second component. This is important, since it demonstrates the ability to synthesize composite materials by the reverse micelle technique.

Collection of the materials synthesized within the micelle has proven to be a difficult task. Obtaining a nanoscale monodispersed material is simple, however, the removal from the reverse micellar system is the difficult part. The steps to extract the material from the system and remove impurities almost always leads to agglomeration of the powders.^{85,100} To synthesize and collect pure and unagglomerated oxide powders, a washing procedure is important. It was seen in the work by Singh and Graeve¹⁰⁰ that the solvent used during cleaning influenced the purity of the final powders. They found that hydrogen peroxide was effective at removing the AOT from the surface of the particles. However, the centrifugation steps cause agglomeration into larger particles. This is believed to be due to a tangling of the surfactant chains, as illustrated in Figure 5.

Something to note is that product yield is extremely small, due to the large volume of oil and small concentration of ions within the water. To perform characterization of the material that involves larger amounts of powder, a scale-up method must be developed to produce a sufficient amount of homogeneous product. Efforts to overcome this challenge are seen in the work by Morrison *et al.*¹⁰¹ Normal bench-top synthesis calls for less than 1 L of solution. Scale up has been successful to nearly 30 L of solution. The solvents, which make up most of the volume, can also be recycled up to 90% efficiency.

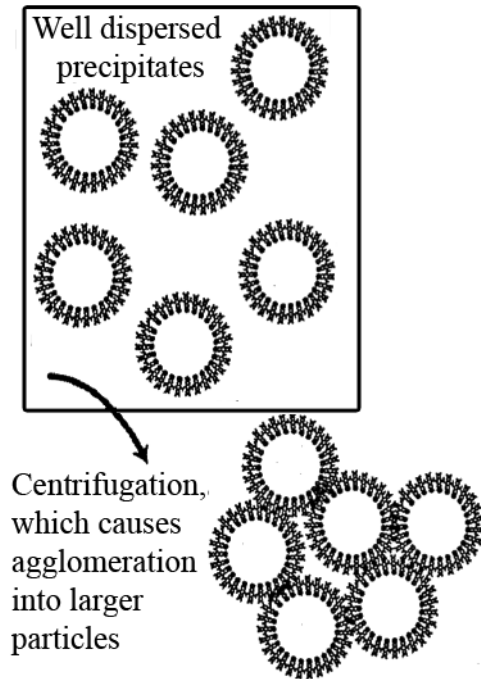


Figure 5. Tangling of surfactant chains during centrifugation leading to agglomeration.¹⁰⁰

E. Spark Plasma Sintering of Optical Ceramics

Spark plasma sintering (SPS) is a process that is comparable to hot-pressing (HP). Both cases use a cylindrical graphite die in which powder is loaded and a uniaxial pressure is applied while experiencing high temperatures at the same time. The main difference between HP and SPS is the heat source. For instance in HP, temperatures are obtained through resistance heating of the elements surrounding the die. On the other hand, SPS uses the application of current directly through the powder bed. High heating rates can be achieved through SPS up to 400°C/min, whereas the highest obtainable through HP is typically around 30°C/min.¹⁰²

A recent review paper by Munir and Quach¹⁰³ shows the trend of papers published about SPS to be rapidly increasing over the past three decades, starting at less than 10 in 1993 to over 400 in 2008. This paper also addresses and discusses the basic and important aspects of SPS. The most important aspects of SPS are the pressure, heating

rate, and current. It was concluded that the pulse pattern of the current had less of an effect on sintering.

Pressure exhibits an important role in sintering as has been demonstrated in the literature. Guillard *et al.*,¹⁰⁴ studying SiC, discovered applying pressure at different temperatures influenced different densification behavior. By applying a pressure of 75 MPa at the sintering temperature, higher densities were achieved compared to applying the pressure at a lower temperature. They attributed this to a difficulty in removing closed porosity after application of pressure. However, in a similar experiment, Chaim and Shen¹⁰⁵ found that the temperature at which pressure is applied during the consolidation of yttrium aluminum garnet had no effect on the density, but the temperature played a role in the final sintered grain size. Applying the pressure before a particular temperature (1375°C) resulted in a smaller final grain size. Pressures applied after that temperature resulted in large grains. They attributed this to particle coarsening at the lower temperatures and concluded that application of pressure at temperatures before substantial coarsening occurs would be beneficial for the suppression of grain growth in the dense specimen. Makino *et al.*,¹⁰⁶ investigated ultrafine alumina and discovered that pressures of 100 MPa would suppress grain growth during sintering, whereas 30 MPa would not.

In a spark plasma sintering study of yttria stabilized zirconia by Quach *et al.*,¹⁰⁷ it was discovered that pressure plays a role on the densification depending on what sintering temperature is used. They found that for a temperature of 980°C the pressure played a large role on final density, increasing from 78% to 96% when pressure was increased from 150 to 700 MPa. When a temperature of 1180°C was used the pressure had an insignificant effect on final density, going from 97% with 150 MPa, to 100% with 700 MPa.

Chaim and Margulis¹⁰⁸ developed SPS densification maps for nanocrystalline MgO. They modeled the case of MgO, at any given pressure, and assumed that the sintering is initially dominated by plastic flow, then by diffusion. In the first stage of sintering, the densely packed powders densify through deformation at the necks between adjacent particles. This increases the number of necks per grain until porosity is closed. In the second stage densification is dominated by plastic deformation, and diffusion

mechanisms through the lattice and along the grain boundaries. Grain growth mechanisms are ignored due to the short sintering cycles. Also, other non-densifying sintering mechanisms are neglected due to the relatively low temperatures used in SPS.

Heating rate also plays an important role in sintering. In theory, high heating rates reduce the time powders experience lower temperatures. Non-densifying grain coarsening mechanisms (e.g., surface diffusion and vapor transport) are dominant at lower temperatures.¹⁰³ In practice, conflicting results are seen. In one case, for the study of alumina, the heating rate (50-700°C/min) had no effect on final density.¹⁰⁹ In another, a negative effect was seen, meaning a high heating rate resulted in lower density.¹¹⁰ In both cases, an effect on grain size was seen, where higher heating rates resulted in a smaller final grain size. Under high-pressure conditions, in the sintering of YSZ, the heating rate had no effect on the densification, but also resulted in smaller grain sizes with higher heating rates.¹⁰⁷

Inconsistencies on the effect of pressure and heating rate are most likely due to differences in materials' properties (i.e. bonding type) and perhaps experimental uncertainties. Over the range of materials studied, the effective thermal and electrical conductivities vary, which gives rise to differing temperature gradients in the samples. The timing and rate of pressure application is likely to cause varying results as well.

1. SPS of Optical Ceramic Oxides

Optical transparency can be achieved in polycrystalline ceramic oxides if the material is fully densified and all scattering sites are minimized or removed completely. Spark plasma sintering has been used with success for the fabrication of transparent polycrystalline ceramics. Some optical materials being sintered by SPS include, but are not limited to, zirconia,^{102,111} alumina,¹¹²⁻¹¹⁶ yttrium aluminum garnet,¹¹⁷⁻¹¹⁹ magnesium aluminum spinel,^{120,121} aluminum nitride,¹²² hydroxyapatite,¹²³ mullite,¹²⁴ lutetium oxide,¹²⁵ magnesia,^{108,126} yttria,¹²⁷ and a magnesia:yttria composite.^{67,70}

Liu *et al.*⁶⁷ were able to sinter by SPS a 50:50vol% MgO:Y₂O₃ composite powder, with particle size around 100-300 nm, to densities higher than 97.5% and grain sizes around 180 nm. The pressures used were 50 MPa and 100 MPa, and a heating rate of 100°C/min, to temperatures of 1150-1350°C. This study determined the effect of powder agglomeration on the ability to achieve high densities. They discovered that as-

received agglomerated powders could only sinter to densities of 98.6%, however, when agglomeration was lessened and particle size was monodispersed, by ultrasonic horn treatment (USH), the highest achievable density was 99.4%. As expected, the sintered specimens of USH treated powders also displayed greater transmittance data than untreated powders. This is due to higher densities, small grain sizes, and uniform microstructure.

A similar study by Jiang and Mukherjee⁷⁰ determined that the infrared transmission results were excellent, which they attributed to small grain sizes and homogeneity of the microstructure in the same system. Temperatures used were between 1200-1600°C, heating rates of 80-200°C, and dwells between 3-8 minutes. The pressure used was 80 MPa. Longer dwells improved transmittance, but when an annealing step was implemented after sintering, the % transmittance values of the sintered specimens increased and were equal, regardless of the dwell time. They also determined that overly large grain size degraded the transmittance.

Since it was discovered that the smaller grain sizes lead to more desired optical characteristics of composites and anisotropic materials, methods to keep the grain size small during densification have been explored. With recent abilities to achieve pressures greater than 150 MPa in the SPS, the effect of high pressure was explored. After the introduction of a double die design utilizing graphite, silicon carbide, and tungsten carbide components, the pressures obtainable in the SPS increased dramatically.¹²⁸ A figure of the double die setup can be seen in Figure 6.

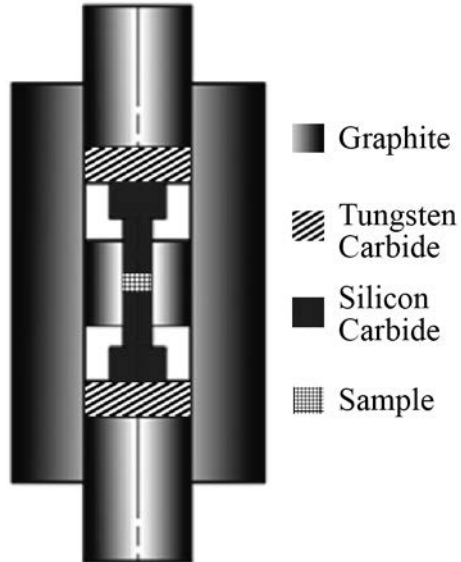


Figure 6. High pressure SPS die.¹²⁸

Some optical ceramic oxide materials being studied in high pressure SPS experiments include alumina,^{112,113} yttria-stabilized zirconia,¹²⁹ hydroxyapatite,¹²³ and zirconia.¹¹¹ Grasso *et al.*¹¹² discovered that fully-dense alumina could be obtained with no considerable grain growth using HIP and SPS at temperatures 200°C lower than conventional sintering methods, due to the pressure assistance in densification. When alumina was doped with magnesia, the grains grew significantly with an increase of pressure at 1200°C, but at a temperature of 1100°C the grain size was not affected by the pressure.¹¹³ Tamburini *et al.*,¹²⁹ studying YZS, obtained dense specimens with a final grain size of 50 nm by utilizing a pressure of 800 MPa. In the case of hydroxyapatite a pressure of 500 MPa could fully densify the material at 700°C whereas 1000°C was needed for 75 MPa. The grain growth was also limited greatly when using the higher pressures.¹²³

EXPERIMENTAL PROCEDURE

A. Solution Synthesis

1. Chemical Precipitation

The materials used for this synthesis process are listed in Table I. To synthesize MgO, magnesium nitrate is added to a beaker of de-ionized water to achieve a molarity of 1 M. To synthesize Y₂O₃, yttrium nitrate is added to a beaker of de-ionized water to achieve a molarity of 0.1 M. A combination of magnesium nitrate and yttrium nitrate is used as the precursor for the synthesis of a composite of MgO-Y₂O₃. A total molarity of 0.5 M is used for this case. These solutions are stirred for 30 minutes.

Table I. List of Chemicals Used and Their Suppliers

Chemical Name	Common name	Chemical Formula	Purity or Conc.
Magnesium (II) nitrate hexahydrate *		Mg(NO ₃) ₂ •6H ₂ O	98%
Yttrium (III) nitrate hexahydrate *		Y(NO ₃) ₃ •6H ₂ O	99.90%
Ammonium hydroxide *		NH ₄ OH	28-30% Conc.
2,2,4-trimethylpentane **	Isooctane	C ₈ H ₁₈	99+%
Docusate Sodium Salt **	Na-AOT	C ₂₀ H ₃₇ NaO ₇ S	meets USP testing specs

* Alfa Aesar, Ward Hill, MA 01835

** Sigma-Aldrich, St. Louis, MO 63103

An excess of five times the required amount (for complete hydroxylation of metal ions to a solid hydroxide) of ammonium hydroxide is then added drop-wise, via burette, to the stirring solution. Upon complete addition of ammonium hydroxide, stirring continues for 30 minutes.

2. Spray Precipitation

To synthesize the MgO-Y₂O₃ using spray precipitation, the magnesium nitrate and yttrium nitrate solution is prepared identically to chemical precipitation method. An excess of five times the required amount of ammonium hydroxide is added to de-ionized water to achieve a 50% dilute solution. The nitrate solution is sprayed into the stirring ammonium hydroxide solution, using a spray bottle. Upon complete addition, stirring continues for 30 minutes.

3. Collection and Washing

A high-speed centrifuge with a maximum rotor radius of 115 mm (Centrifuge 5810, Eppendorf, Hamburg, Germany) is used for the collection of powders. The solution is then poured into vials and centrifuged at 9000 rpm for 1 minute. The supernatant is then decanted and the precipitate is left on the bottom of the vial. Ethanol is added to the vials that are then shaken and ultrasonicated to de-agglomerate and remove any remaining ions. This is centrifuged again, and the solids are then scooped from the vials and allowed to dry. Upon significant drying, the hydroxide powders are ground using a pestle and mortar.

4. Milling

The uncalcined powders must be milled to homogenize the mixture of the two phases. Approximately 10 g of powder is added to 80 mL of methanol. This mixture is added to a polyethylene plastic bottle with 3 mm zirconia milling media added $\frac{1}{4}$ the height of the bottle. The speed is adjusted to the point where cascade milling occurs.

5. Reverse Micelle Synthesis

For reverse micelle synthesis a continuous oil phase is required, 2,2,4-trimethylpentane (isooctane) is used. Docusate sodium salt (Na-AOT) is used as the surfactant, which will create stable domains of water within the system. The ratio of isooctane to water is 28:1. A water-to-surfactant ratio of $\omega_o=10$ was chosen after a series of various ratios were tested ($\omega_o=10, 12.5, \text{ and } 15$). A molarity of 0.3 M was chosen for the synthesis conditions after multiple molarities (0.05-0.7 M) were explored.

To create the stable reverse micelle solution, two solutions were prepared and combined. The first solution was isooctane and Na-AOT. This was allowed to stir for 30

minutes. The second solution was water, magnesium nitrate and yttrium nitrate, which was also allowed to stir for 30 minutes. The nitrate solution was then added to isooctane solution. This combined solution was stirred for 2 hours, to ensure equilibrium had been reached. After 2 hours, the solution was translucent. DLS analysis of the solution at this point was conducted to measure the size of the reverse micelles.

To precipitate the Mg^{2+} and Y^{3+} to $Mg(OH)_2$ and $Y(OH)_3$ within the micelle, a third solution was made. Ammonium hydroxide was added to isooctane at a concentration of 0.03 M. The amount of isooctane used was equal to the volume used in the previous step. This solution was allowed to stir rapidly for 5 minutes. After stirring, this solution was added to the reverse micelle solution. Great care must be used to avoid the addition of water (from the ammonium hydroxide) settling on the bottom of the beaker, which is immiscible in isooctane.

To collect the precipitate, the solution was separated into vials and centrifuged at 11,000 rpm for 10 minutes, using the same centrifuge used in the precipitation synthesis techniques. A clear gel was collected at the bottom and the supernatant was decanted. Ethanol was added to the vial, which was shaken and ultrasonicated. This was then centrifuged again at 11,000 rpm for 10 minutes. The supernatant was then decanted and water was added to the vial, which was then shaken and ultrasonicated. The vial was then centrifuged again at 11,000 rpm for 10 minutes. This was followed by alternating two more ethanol and two more water washes, using the same technique and parameters. One final ethanol rinse was performed to remove any water from the surface of the particles. The entire washing sequence was ethanol, water, ethanol, water, ethanol, water, ethanol.

The collected hydroxide material was scooped from the vials and allowed to dry. Upon significant drying the hydroxide powders were ground, using a pestle and mortar.

6. Heat Treatment

Decomposition of $Mg(OH)_2$ and $Y(OH)_3$ into MgO and Y_2O_3 occurs at approximately 400 to 600°C. To ensure complete decomposition and crystallization, a temperature of 500°C for MgO and 600°C for Y_2O_3 and the MgO - Y_2O_3 composite was utilized for the heat treatment of the chemical precipitation powders. Spray precipitation composite powders and reverse micelle composite powders were calcined at 1000°C. A

thin layer of powder was placed in a crucible. The crucible was then placed in a set point controlled furnace (F1848, Lindberg, Riverside, MI) at low temperature (less than 100°C) and rapidly heated (approximately 60°C/min) to the specified temperature. After 1 hour the furnace was turned off and the door was opened to cool the powders rapidly in air.

B. Spark Plasma Sintering

1. Conventional Low Pressure SPS

A spark plasma sintering apparatus (HP D 25/2, FCT Systeme GmbH, Rauenstein, Germany) was used to sinter these materials. A picture of the equipment can be seen in Figure 7. Graphite molds (dies) with the configuration shown in Figure 8 were used for initial sintering experiments. These molds are capable of achieving pressures of 140 MPa, temperatures of 2200°C in vacuum and inert atmosphere, and heating rates of 400°C/min. The diameter of the mold is 18.5mm and the setup allows for the insertion of a graphite paper lining preventing reaction of material with the die wall, which leads to die degradation.

Approximately 5 g of powder is placed in the die. Whilst adding powder, tapping or vibrating the die must occur to evenly distribute powder in the die. Once all powder is added, the powders are pressed to 100 MPa.

The die configuration is wrapped with graphite felt, to provide insulation during the heating process, and placed inside the SPS furnace. The felt has a small hole so that focusing of the optical pyrometer on the outside wall of the die can be performed. The temperature is monitored by the optical pyrometer on the outside wall of the die.



Figure 7. Picture of the spark plasma sintering apparatus.

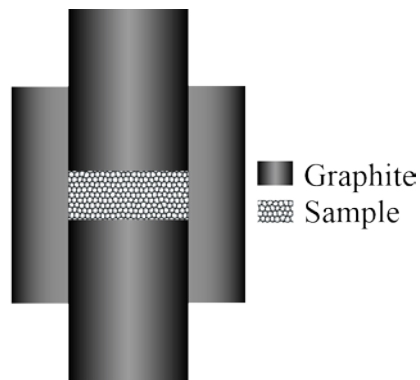


Figure 8. Normal graphite die setup.

Multiple temperatures, pressures, and heating rates have been used to determine the optimum sintering parameters. Low temperature, fast heating rates, short dwells, and high pressures should be used. Temperatures between 700 and 1300°C, heating rates of 50 to 300°C/min, dwells of 0-10 minutes, and pressures of 50-140 MPa were explored with this setup. Force was applied during the heating segment. A schematic of the sintering cycle can be seen in Figure 9.

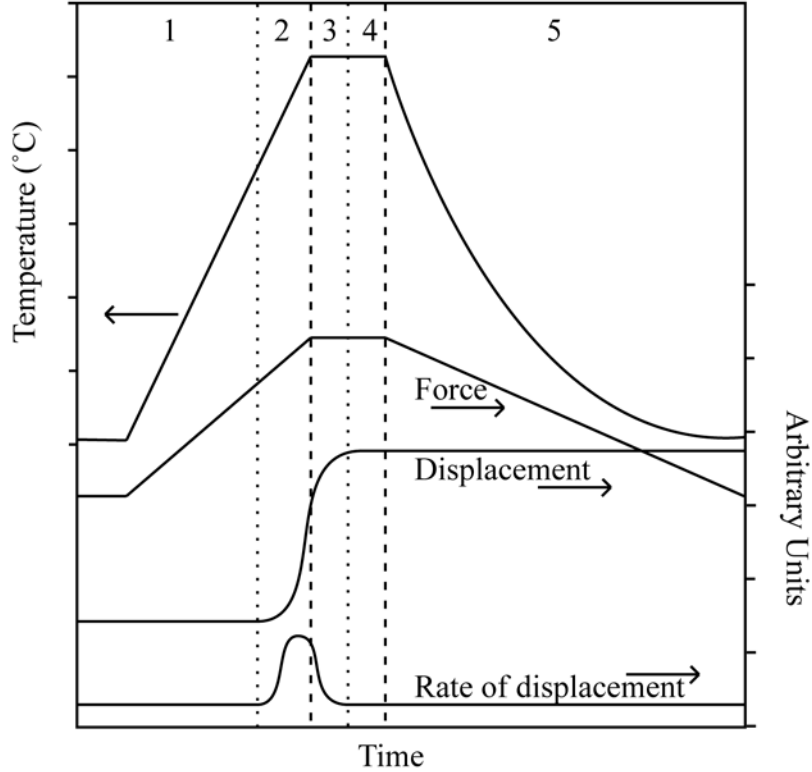


Figure 9. Schematic of a sintering profile for the normal graphite die setup.

2. High Pressure SPS

A die setup that allowed for higher pressures was necessary for complete densification of the MgO-Y₂O₃ composite. Modifications to the setup designed by Tamburini *et al.*¹²⁸ were made. The die consists of an outer graphite die, with inner diameter of 40 mm ϕ , two 40 mm ϕ solid graphite plungers, two silicon carbide pucks 20 mm ϕ \times 15 mm thick, two silicon carbide rods 10 mm ϕ \times 25 mm long, and one inner graphite die OD 40 mm ϕ and ID 10 mm ϕ . There is space between the silicon carbide rods and inner die wall for the use of a graphite paper lining of thickness 0.127 mm. A diagram of the setup can be seen in Figure 10. Squareness of all parts is crucial in regards to high-pressure application. Placing a thermocouple in the outer die 1 mm from the inner wall is used to monitor the temperature.

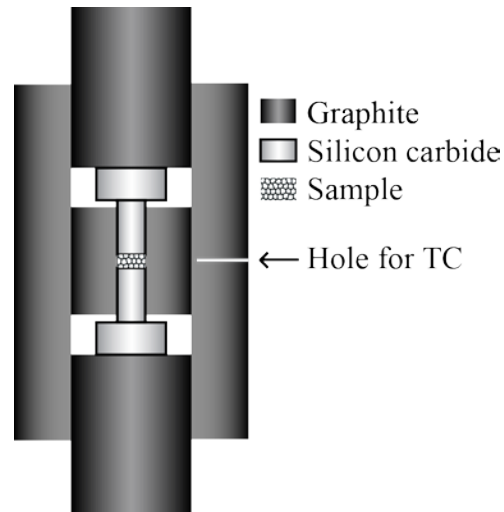


Figure 10. Die arrangement for high pressure SPS experiments.

Pressures of 300-500 MPa, using 50 MPa intervals, were explored. A temperature of 1000°C and a heating rate of 100°C/min was used. The force was held at 38 MPa until final sintering temperature was achieved. A dwell of 5 minutes was used to allow the die to obtain thermal equilibrium. After the 5-minute dwell the high pressures were applied slowly over a period of 1 minute. A dwell of 1 minute at high pressure was then used to allow for additional sintering. The dwell time at final sintering temperature was 7 minutes. One sample was sintered following the same heating schedule with a constant pressure of 38 MPa. A schematic of the high-pressure sintering cycle can be seen in Figure 11.

Approximately 1.2 g of spray-precipitated powder was added to the inner die and sintered. The reverse micelle powders were sintered at 1000°C and 500 MPa, following the same parameters as the prior high-pressure experiments.

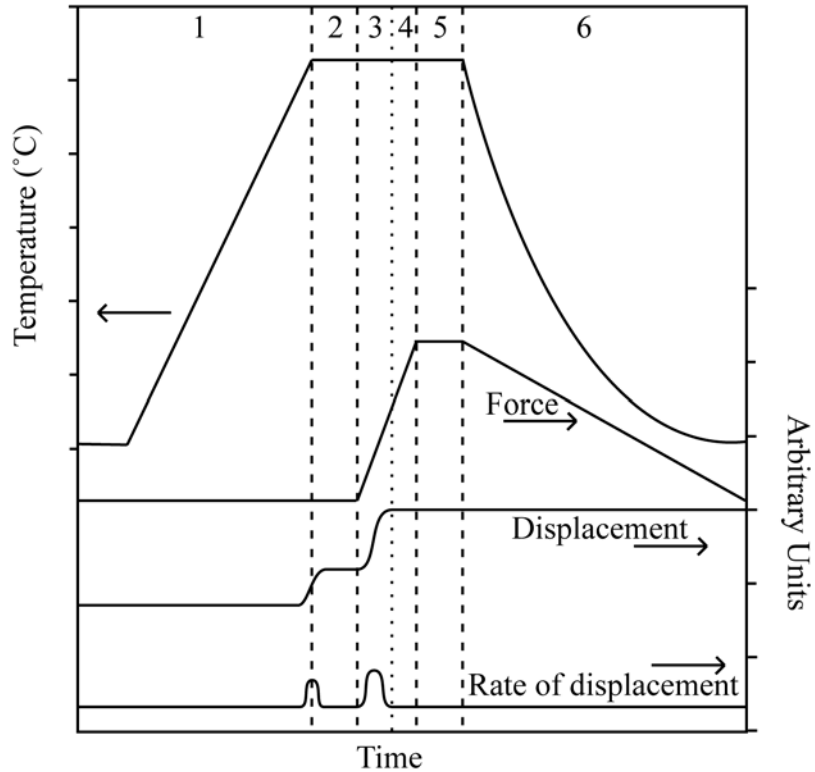


Figure 11. Schematic of the sintering profile for high pressure experiments.

C. Characterization

1. Powder

a. Dynamic Light Scattering

i. Precipitation Synthesis

Dried and ground powders made by all the precipitation techniques were characterized by a dynamic light scattering instrument (Nanotracer Ultra DLS, Microtrac, Montgomeryville, PA). Particle size was measured before and after heat treatment. Samples for DLS were prepared in three different solutions to determine the best dispersion characteristics. For each solution 0.015 g of powder was added to 25 mL of water, ethanol, or acetone. Background reading levels of the chosen suspension medium were taken before the particle size measurements. Five individual particle size measurements were taken and the average was calculated. The sample was analyzed five

times and an overall average was calculated. This gives an average value for 25 measurements.

ii. Reverse Micelle System Stability

Characterization of reverse micelle solution stability was completed by DLS. DLS was performed on all solutions to observe the effect of salt additions on micelle size and the effect of varying water-to-surfactant ratios on stability. Background reading levels of the isooctane were taken before the particle size measurements. Five individual particle size measurements were taken and the average was calculated. The sample was analyzed five times and an overall average was calculated. This gives an average value for 25 measurements. Particle size after synthesis and collection was also measured after each washing cycle of one ethanol wash and one water wash.

b. Thermogravimetric Analysis

For obtaining calorimetric measurements a thermogravimetric instrument (SDT 2960 Simultaneous DSC-TGA, TA Instruments, New Castle, DE) was used. TGA analysis required 10-25 mg of powder to be placed in an alumina crucible. In an air atmosphere a heating profile from room temperature to 1000°C with a heating rate of 15°C/min was used and the weight was monitored and recorded every 2 seconds.

c. X-ray Diffraction

An X-ray diffractometer (D2 Phaser, Bruker, Madison, WI) was used for XRD spectrum collection. To analyze the sample using XRD, powders were packed into a shallow sample holder and packed to obtain a flat surface. The sample was then placed into the X-ray diffractometer and analyzed using Cu K α radiation. Diffraction intensity was measured at 2θ values from 15-115°. Spectrum analysis was performed in X-ray diffraction pattern analysis software (Jade, Materials Data, Inc., Livermore, CA).

i. Phase separation

For determining the level of phase separation during centrifugation a series of XRD experiments were performed. Powders were collected from the top and bottom of the centrifuge vial for 5 different centrifuging times. The powders were dried, crushed, then heat-treated at 600°C for 1 hour. X-ray characterization was performed on each extracted sample.

ii. Time-resolved XRD at Varying Temperatures

Time-resolved X-ray diffraction was performed using an X-ray diffraction apparatus with hot stage (D9, Bruker, Madison, WI). A small amount of uncalcined spray precipitation powder was dispersed with a small amount of methanol and spread upon a sapphire plate. The powder was then allowed to dry and the plate was then placed into the instrument. Diffraction intensity spectra was collected between 15 and 150°2 θ and collected at 30°C, 100°C, 200°C, 300°C, 310°C, 320°C, 330°C, 340°C, 350°C, 400°C, 500°C, 600°C, 700°C, 800°C, 900°C, and 1000°C. Thermal expansion calibration z-offset values were programmed into the instrument to ensure constant sample surface position during the cycle.

d. Brunauer, Emmitt, and Teller (BET) Surface Area

A surface area and porosity analyzer (TriStar, Micromeritics, Norcross, GA) was used for surface area measurements, with multi-point analysis of 11 points. Powders were degassed and placed into the instrument. Liquid nitrogen was used to cool the sample. Nitrogen was used as the absorption gas.

e. High Resolution Imaging

i. Transmission Electron Microscopy

A transmission electron microscope (2010, JEOL, Peabody, MA) was used for powder imaging. Powders were dispersed in ethanol and a TEM grid was passed through the solution to gather powders. Samples were then imaged using an accelerating potential of 200 kV.

ii. Scanning Electron Microscopy

Scanning electron microscopes (SU70, Hitachi, Krefeld, Germany) (Quanta 200F, FEI, Hillsboro, OR) were used for sintered specimen imaging. Fracture surfaces were carbon coated to minimize charging during analysis. Relatively low accelerating potentials (<10 keV) produced the clearest images.

A digital image analysis software (ImageJ, National Institutes of Health, Bethesda, MD) was used to measure grain sizes. Numerous horizontal lines were drawn across each micrograph. The grains that were located on the line were then used for the measurement and calculation of the average grain size for each sample. An average

linear intercept length was determined after the analysis of 200 grains for each sintered specimen. This length is referred to as grain size herein.

f. Density Measurements

A water immersion density measurement technique (ASTM C20) was used to determine the density of the sintered specimens.¹³⁰ Samples were boiled in water for 2 hours and allowed to cool and soak overnight. The dry weight, suspended weight, and saturated weight were used in the calculations to determine density.

RESULTS

A. Chemical Precipitation Synthesis

Chemical synthesis of magnesium oxide, yttrium oxide, and a composite of the two was successful by hydroxide precipitation. Understanding the synthesis and characteristics of the individual components of a composite material is helpful when designing the experiments for composite synthesis. This method may provide insight on any difficulties early on, so that they can be avoided in the synthesis of the final desired composite powder.

1. Magnesium Oxide

After synthesis, the collected hydroxide powders were washed once with ethanol. The powders were calcined to crystallize into the stable desired phase. To understand the decomposition and crystallization temperatures TGA analysis was completed. TGA analysis of the as-synthesized powders showed a small weight loss around 100°C, a large weight loss around 400°C, and a slow continual loss of weight up to 1000°C, as seen in Figure 12. The first weight loss around 100°C is attributed to the evaporation of water on the surface of the powders. The second weight loss that occurs around and after 400°C is attributed to the decomposition of the hydroxide to the oxide. Weight loss continues at the higher temperatures due to a continuation of the decomposition reaction. For XRD analysis, the heat treatment temperature was chosen to be 500°C for 1 hour, to ensure complete decomposition and crystallization.

Powders heat treated at 500°C (Figure 13) show phase pure magnesium oxide in cubic form as compared with PDF 00-045-0946. Using X-ray line broadening techniques, namely Williamson-Hall technique in the Jade XRD analysis software, crystallite size was determined to be 15.3 ± 2.5 nm.

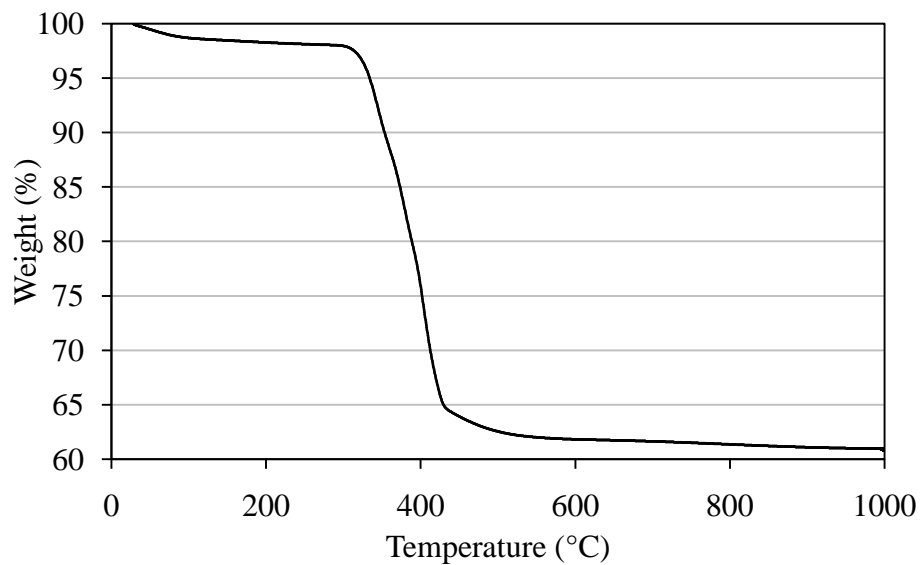


Figure 12. TGA plot showing the weight loss with respect to temperature, indicating decomposition temperature of magnesium hydroxide into magnesium oxide.

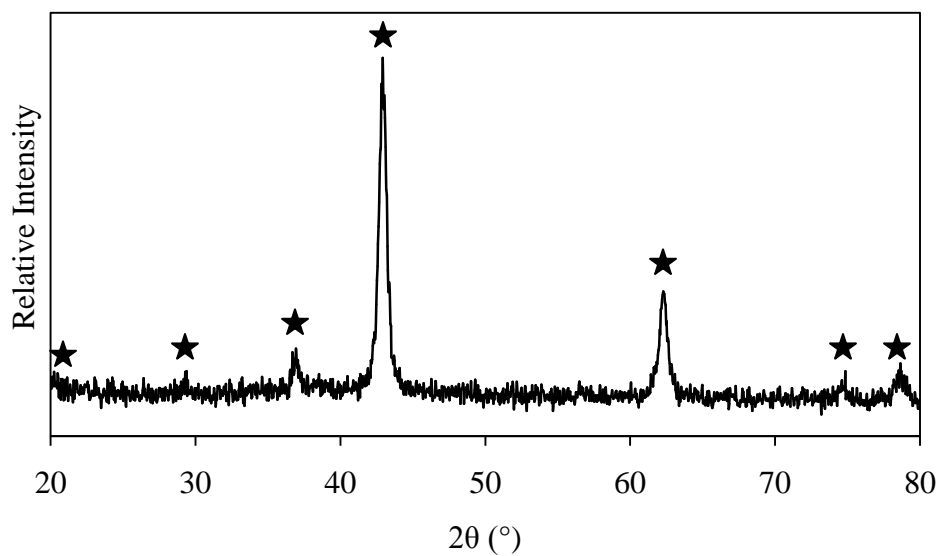


Figure 13. XRD pattern showing the crystallinity and mineralogy of heat-treated MgO. Peaks indicated by circles are representative peaks for the MgO PDF 00-045-0946.

Particle size was determined by DLS. The suspension medium plays an important role in the dispersion of the powders and ultimately the measurement of particle size. It can be seen in Figure 14 that water is the least effective at dispersing, followed by acetone. Ethanol provides the greatest dispersion characteristics. Ethanol is used herein as the dispersion medium for DLS of powders.

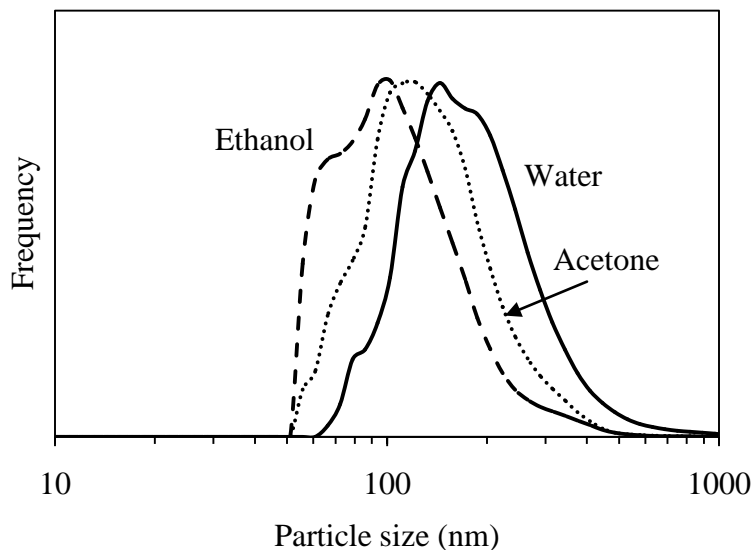


Figure 14. DLS data of MgO dispersed in water, acetone, and ethanol.

Figure 15 shows the DLS data of the as-synthesized magnesium hydroxide and calcined magnesium oxide powders. The calcined powders have a smaller mean particle size of about 70 nm compared to the as-synthesized powders of about 300 nm.

Transmission electron microscopy (TEM) was used to determine the morphology of the particles. Displayed in Figure 16, the as-synthesized powders are large and agglomerated, which is also evident in the DLS data. After heat treatment, the particles are less agglomerated and much smaller. The morphology of the particle appears to consist of multiple crystallites agglomerated together with rounded edges.

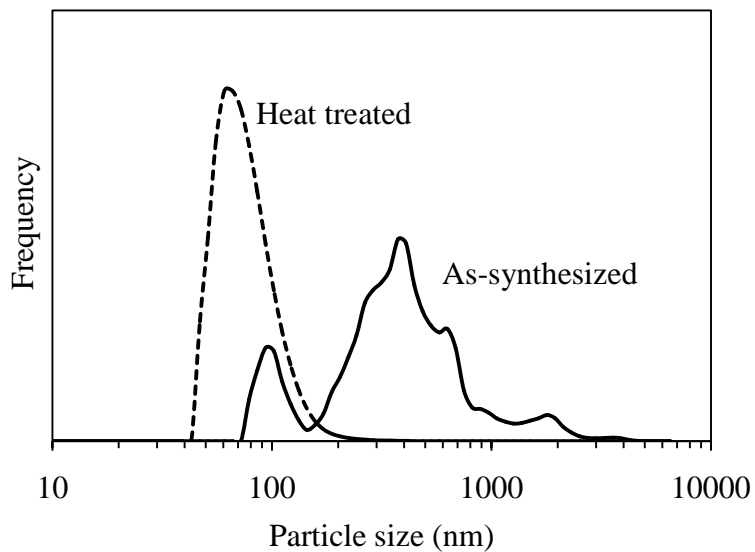


Figure 15. DLS of MgO synthesized by chemical precipitation before and after heat treatment.

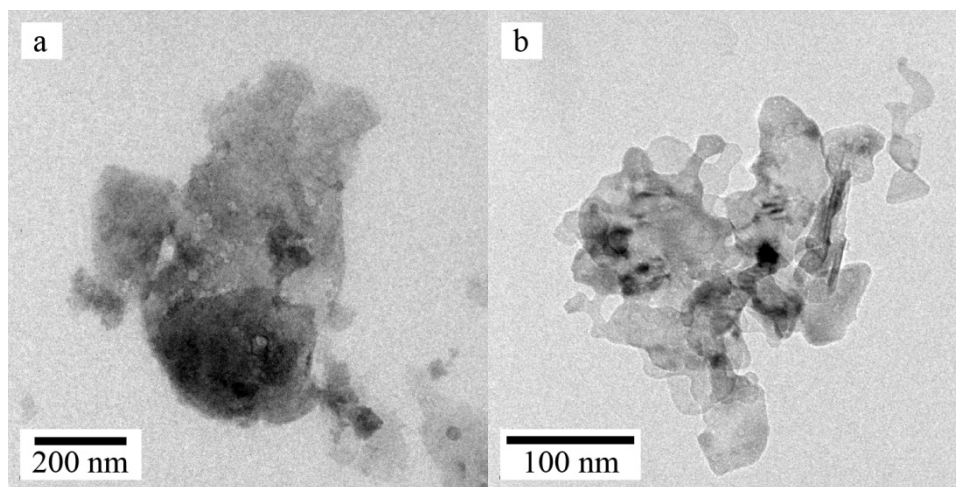


Figure 16. TEM of as-synthesized and heat-treated MgO synthesized by chemical precipitation method.

Using BET surface analysis techniques the surface area of the precipitated, calcined, MgO powders was determined to be $72.8 \text{ m}^2/\text{g}$. The estimated particle size, from the surface area relationship (Equation 1), was 21.4 nm. This does not correlate to the particle size as measured by DLS, but it does correlate well to the crystallite size by XRD. This means that the particles are agglomerates composed of many small crystallites.

$$d(nm) = \frac{6000}{\rho * SA} \quad (1)$$

2. Yttrium Oxide

The pure Y_2O_3 was synthesized in the same manner as the MgO and the same characterization steps were performed. The as-synthesized powders were agglomerated, as shown from DLS in Figure 17. The TGA data shows two major weight loss events, displayed in Figure 18, with complete decomposition occurring around $560^\circ C$. The first event is attributed to the crystallization of monoclinic yttria, the second is attributed to the crystallization of cubic yttria. The heat treatment temperature was chosen to be $600^\circ C$ for 1 hour, to ensure full decomposition and crystallization for XRD analysis. Figure 19 shows the XRD pattern of calcined Y_2O_3 . The pattern is comparable to the PDF 00-041-1105, the star pattern for cubic Y_2O_3 . Crystallite size was found to be 17.0 ± 1.6 nm. Calcined Y_2O_3 has a mean particle size around 85 nm, as displayed in Figure 17.

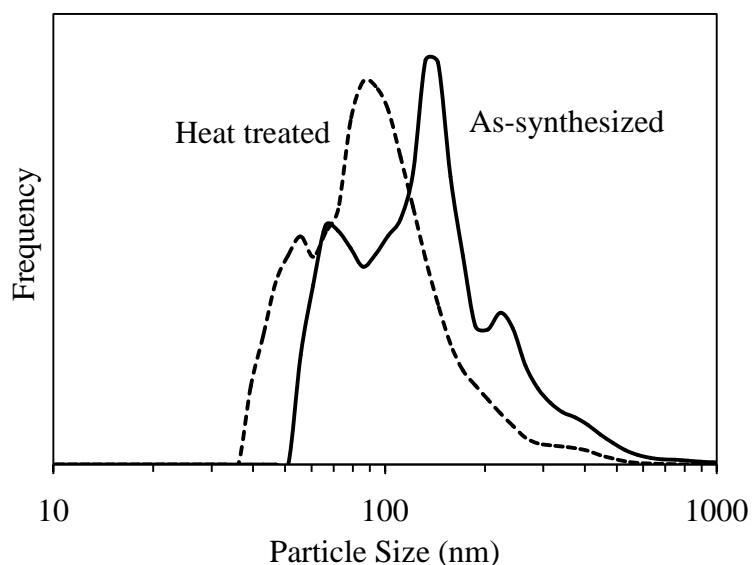


Figure 17. DLS data of as-synthesized and heat-treated Y_2O_3 synthesized by chemical precipitation method.

Both MgO and Y_2O_3 have been successfully synthesized by a conventional hydroxide precipitation method. The synthesis of the individual components proves that

this method results in pure nanometer-sized powders. Therefore, it seemed logical that a composite of these two materials could be produced by a co-precipitation method.

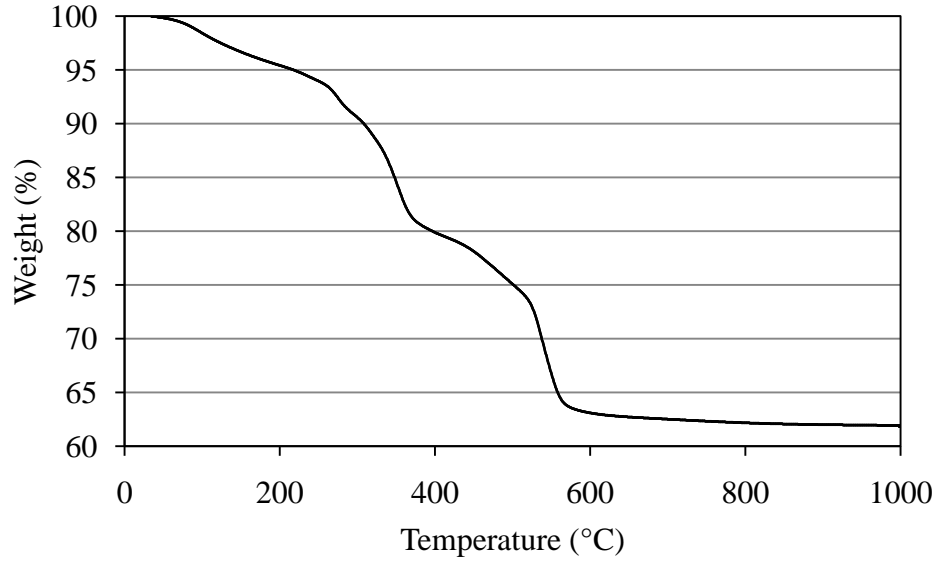


Figure 18. TGA plot showing the weight loss with respect to temperature, indicating decomposition temperature of yttrium hydroxide into yttrium oxide.

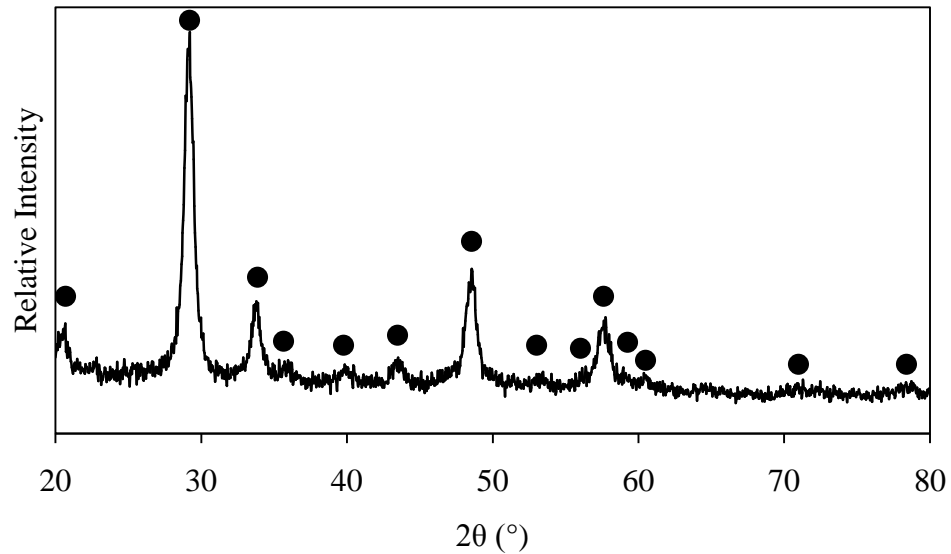


Figure 19. XRD pattern showing the purity, crystallinity, and mineralogy of heat-treated Y₂O₃ synthesized by chemical precipitation method. Peaks indicated by circles are representative peaks for the Y₂O₃ PDF 00-041-1105 with intensities of four or greater.

3. Magnesium Oxide-Yttrium Oxide Composite

To synthesize the desired MgO-Y₂O₃ composite material, with good homogeneity, a co-precipitation procedure was developed. Using the proper mixture ratio for the desired composite material ratio, the MgO and Y₂O₃ were precipitated simultaneously.

As-synthesized particles were agglomerated as indicated by DLS in Figure 20. TGA analysis, displayed in Figure 21, revealed similar decomposition temperatures to those seen for MgO and Y₂O₃ (Figure 12 and Figure 18, respectively).

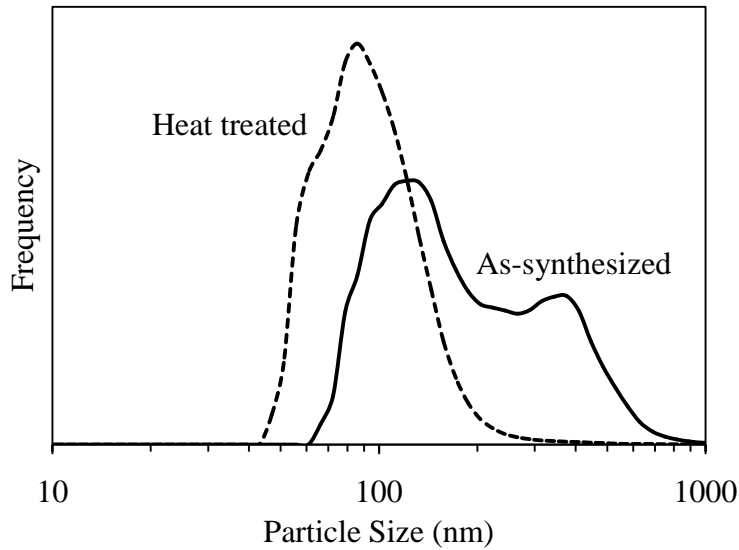


Figure 20. DLS data of as-synthesized and heat-treated MgO-Y₂O₃ composite powders synthesized by chemical precipitation method.

Powders heat-treated to 600°C for 1 hour showed a biphasic crystalline pattern containing cubic MgO and cubic Y₂O₃, confirmed by XRD in Figure 22. These phases can be compared to the same PDF cards as before. Crystallite size analysis showed that MgO had a crystallite size of 24.7±6.5 nm and Y₂O₃ had a crystallite size of 7.6±1.1 nm.

After heat-treatment the particle size decreased, seen by the DLS data in Figure 20. The average particle size was around 105 nm. TEM imaging was also done on these powders before and after heat-treatment. The micrographs are shown in Figure 23. Large agglomerates can be seen in both as-synthesized and heat-treated powders. The

heat-treated powders, however, exhibit crystalline structure and are about half the size. Evidence of platelets can also be seen in the heat-treated powder images.

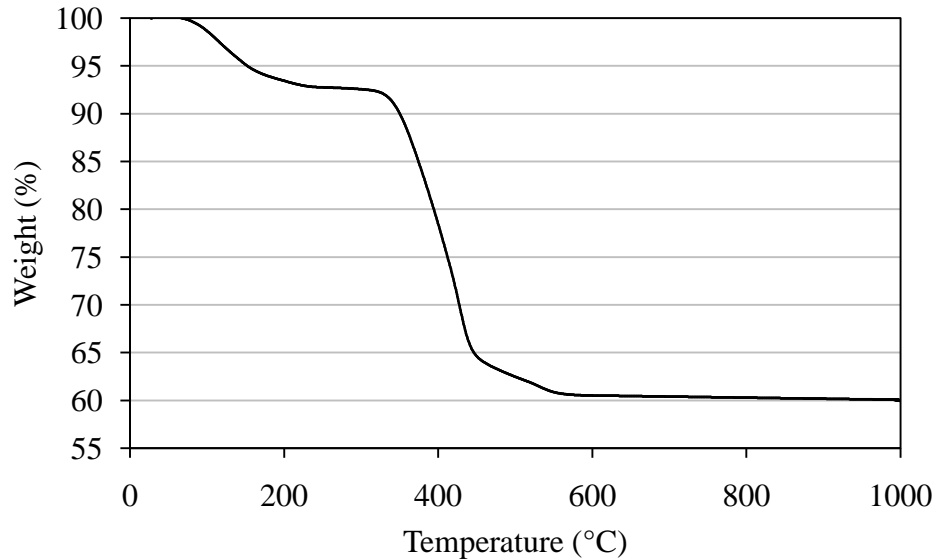


Figure 21. TGA plot showing the weight loss with respect to temperature, indicating decomposition temperature of the composite hydroxides into the MgO-Y₂O₃ composite powders synthesized by chemical precipitation.

Using BET surface analysis techniques the surface area of the precipitated, heat-treated, MgO-Y₂O₃ composite powders was determined to be 55.03 m²/g. Using this surface area the estimated particle size was about 28 nm. This value is closer to that of the crystallite size, meaning the powders are agglomerated and contain many crystallites.

Chemical precipitation and co-precipitation synthesis methods were proven to be successful for the preparation of MgO, Y₂O₃, and MgO-Y₂O₃ composite materials. However, the particle size of final powders was larger than desired for the continuation of optimization and processing. Therefore, an alternative method was used to produce powders with a smaller final particle size.

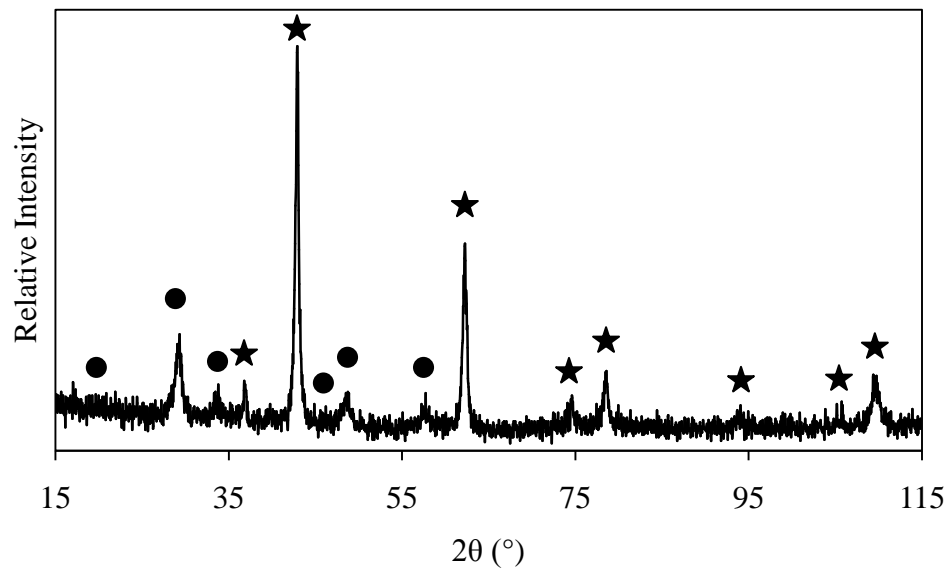


Figure 22. XRD pattern showing the purity, crystallinity, and biphasic nature of heat-treated MgO-Y₂O₃ composite powders. Peaks indicated by circles are representative peaks for the Y₂O₃ PDF 00-041-1105 with intensities of eight or greater. Peaks indicated by stars are representative peaks for the MgO PDF 00-045-0946.

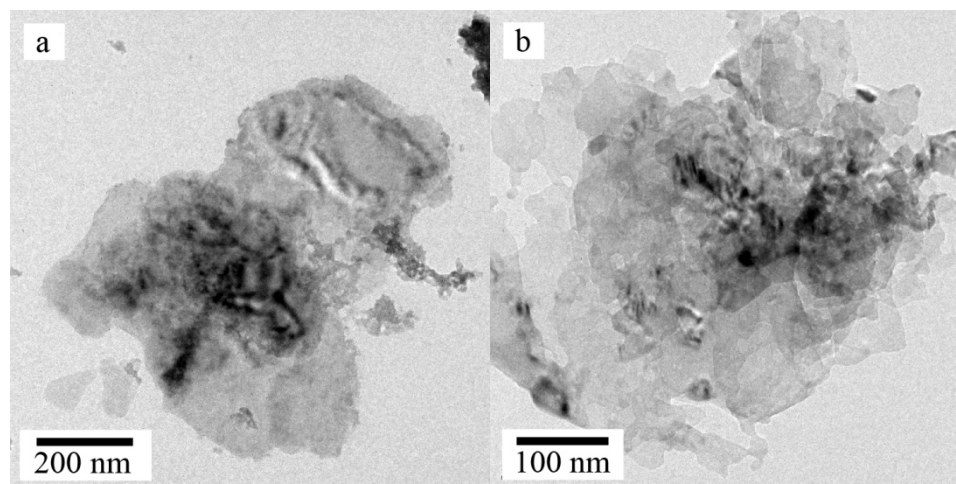


Figure 23. TEM micrographs of as-synthesized and heat-treated MgO-Y₂O₃ composite powders synthesized by normal precipitation, showing morphology.

B. Spray Precipitation Synthesis

Uncalcined powders were agglomerated as indicated by the DLS data in Figure 24. TGA analysis revealed similar decomposition temperatures to those seen in the previous method, shown in Figure 25. A heat treatment temperature of 1000°C for one hour was used. This ensures the complete decomposition and crystallization of the powders and produces the best powder characteristics for sintering.

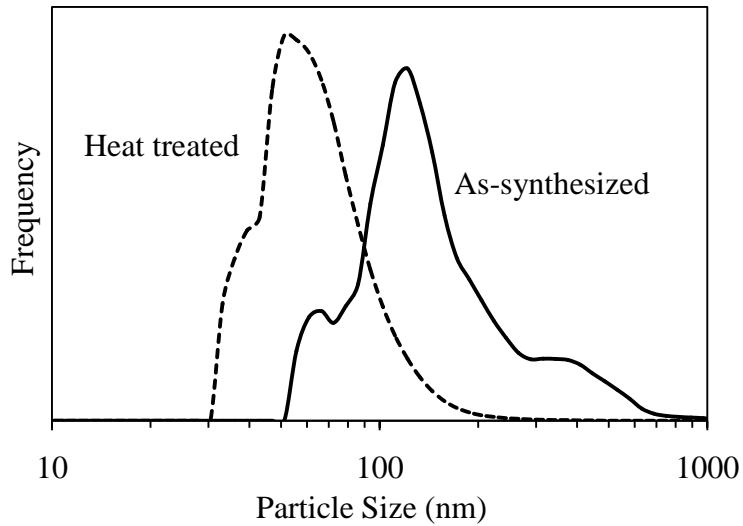


Figure 24. DLS of as-synthesized and heat-treated MgO-Y₂O₃ composite powders synthesized by spray precipitation.

After calcination the particle size decreased, seen by the DLS data in Figure 24. The mean particle size is about 60 nm, which is more desirable than the previous method. XRD in Figure 26 shows the composite material is phase pure and biphasic, containing cubic MgO and cubic Y₂O₃. The crystallite size of MgO is 32.1±3.2 nm and that of Y₂O₃ is 20.2±0.9 nm.

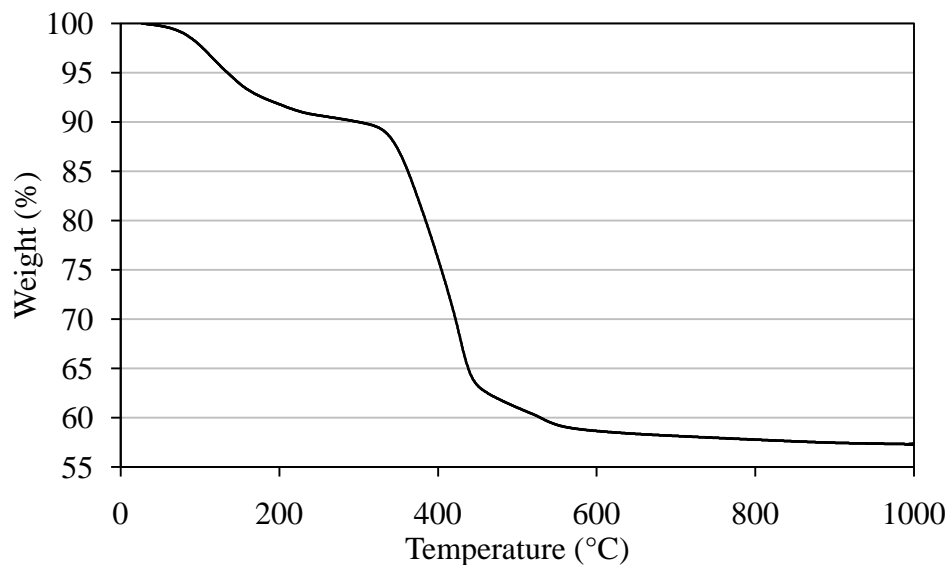


Figure 25. TGA plot showing the weight loss with respect to temperature, indicating decomposition temperature of the composite hydroxides into MgO-Y₂O₃ composite powders synthesized by spray precipitation.

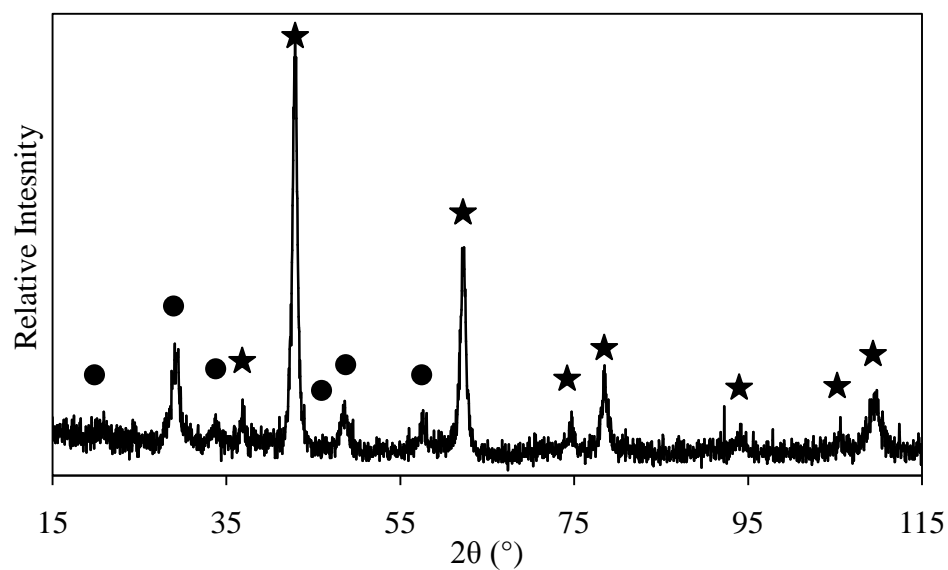


Figure 26. XRD pattern showing the purity, crystallinity and biphasic nature of heat-treated MgO-Y₂O₃ composite powders synthesized by spray precipitation. Peaks indicated by circles are representative peaks for the Y₂O₃ PDF 00-041-1105 with intensities of eight or greater. Peaks indicated by stars are representative peaks for the MgO PDF 00-045-0946.

To further understand the phase transitions from a hydroxide to an oxide, time-resolved XRD at various temperatures was performed. Figure 27 shows the data collected at various temperatures, compiled into one figure. From room temperature up to about 300°C the hydroxide phase is present. At about 310°C the MgO starts to form. Around 320°C is when monoclinic Y₂O₃ forms. Between 600°C and 700°C monoclinic Y₂O₃ transforms into cubic Y₂O₃.

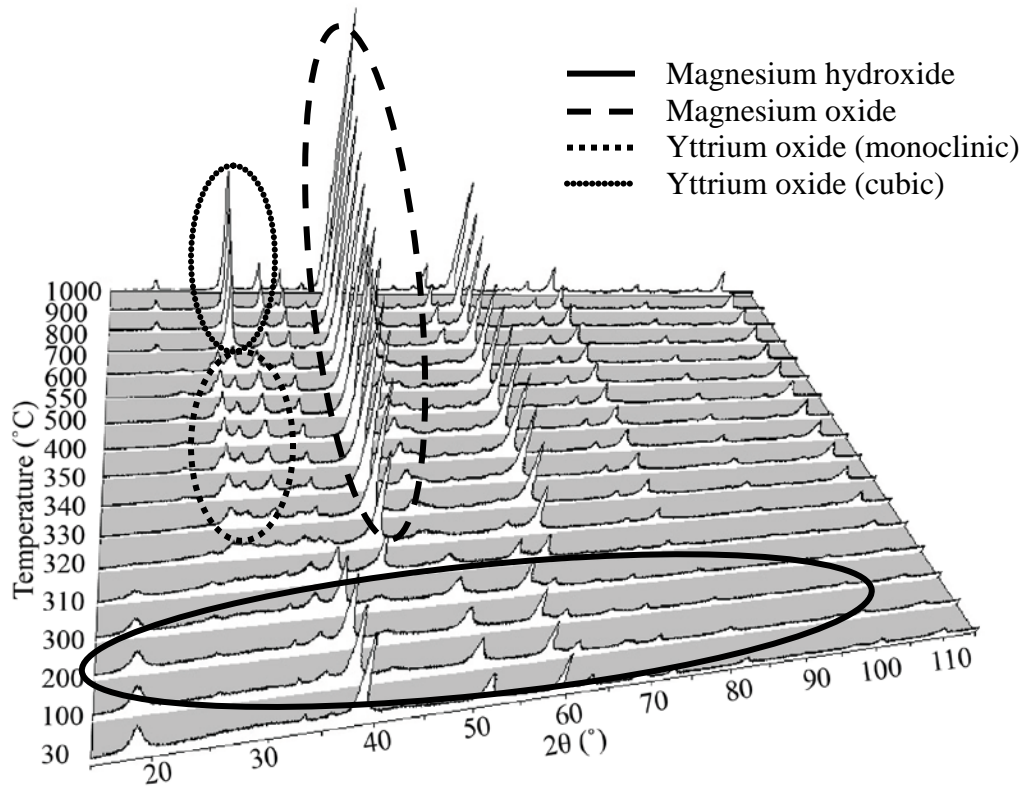


Figure 27. In-situ XRD patterns of as-synthesized MgO-Y₂O₃ composite powders synthesized by spray precipitation technique. Circled peaks indicate peaks corresponding to a particular phase and mineralogy as shown in the legend.

Figure 27 shows that the uncalcined powders (30°C pattern) are a crystalline form of the magnesium hydroxide compared to PDF 00-044-1482. Processing the powders in methanol crystallizes the amorphous hydroxide. Also, the monoclinic phase of Y₂O₃ is seen at temperatures below 600°C compared to PDF 00-044-0399. The heat treatment temperature was chosen above this temperature since phase transformations during

sintering could lead to complications. At the explored temperatures, the MgO and Y₂O₃ do not interact, meaning it is a true two-phase composite. Crystallite sizes were analyzed and plotted in Figure 28. As expected the crystallite size increases as temperature increases.

TEM imaging was also done on these powders before and after heat-treatment. The micrographs can be seen in Figure 29. Agglomerates can be seen in both as-synthesized and calcined powders. The heat-treated powders exhibit defined crystalline structure and platelet-like morphology. These powders show a more defined angular and crystalline structure than those synthesized by the chemical precipitation method, which is due to the higher heat treatment temperature.

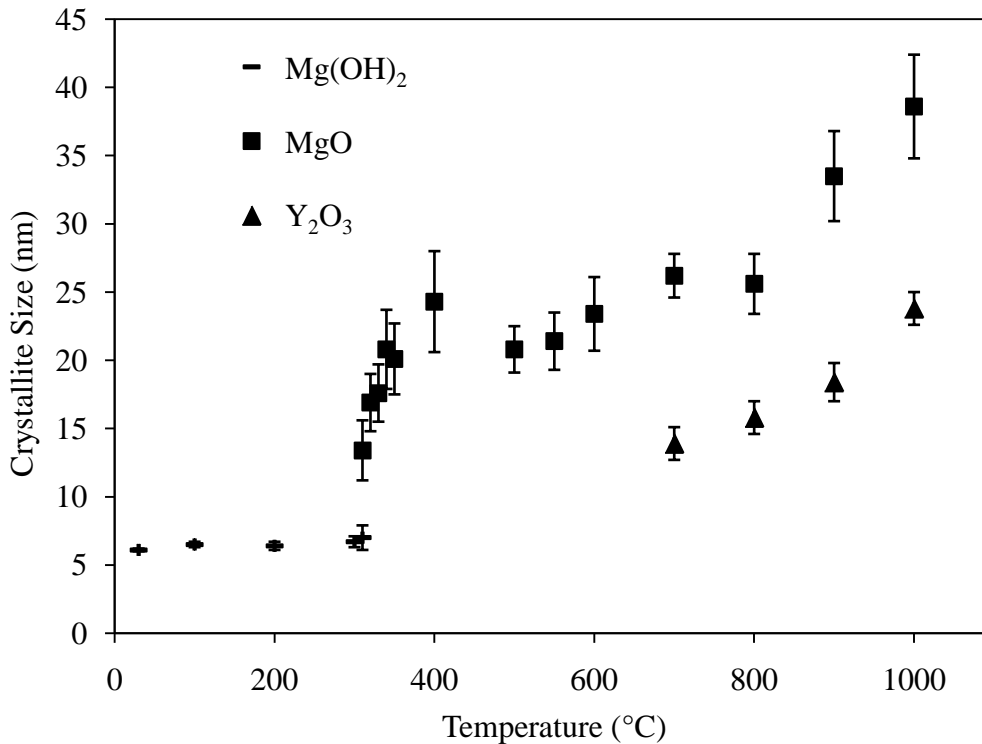


Figure 28. Graph displaying the crystallite growth, from XRD, with respect to temperature.

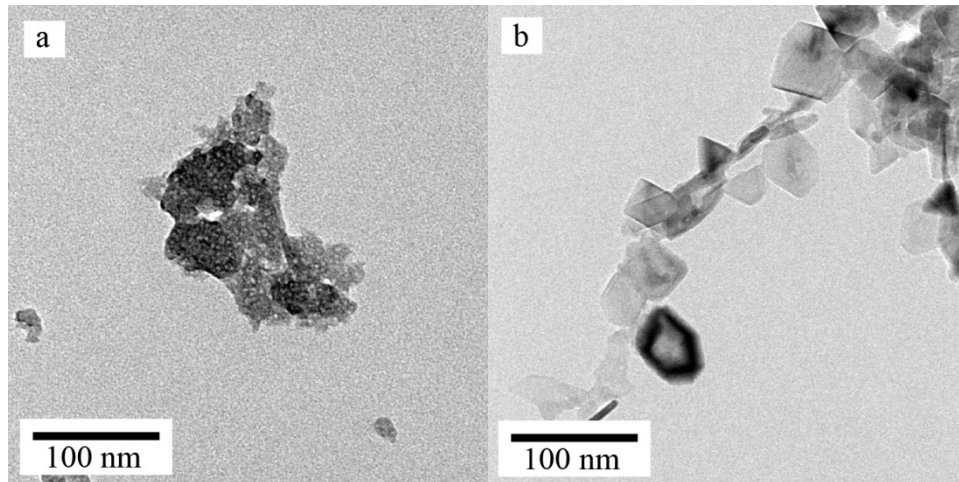


Figure 29. TEM micrographs of as-synthesized and heat-treated MgO-Y₂O₃ composite powders synthesized by spray precipitation, showing morphology.

Using BET surface analysis techniques the surface area of the spray precipitated, calcined, MgO-Y₂O₃ composite powders was determined to be 58.2 m²/g. Using the surface area relationship to particle size, the estimated particle size is 26.8 nm. This value correlates well with crystallite size, but not the particle size from DLS. This likely means the particles are composed of agglomerated groups of crystallites.

After the SEM investigation of preliminary SPS sintered specimens, it was evident through the use of backscatter electron detection mode, that the homogeneity of powders was poor. Figure 30 shows a micrograph of the sintered specimen, where islands (bright areas) of high Y₂O₃ concentration can be seen. The phase separation originates in the washing/centrifugation procedure. Quantitative XRD analysis techniques were used to determine the ratio of phases present in samples collected from the bottom and top of a centrifuge vial for multiple centrifugation times, it can be seen that phase concentration differs depending on location. The graph in Figure 31 shows that the top of the vial has a lower concentration of Y₂O₃ than the bottom of the vial, consistent with segregation due to density differences.

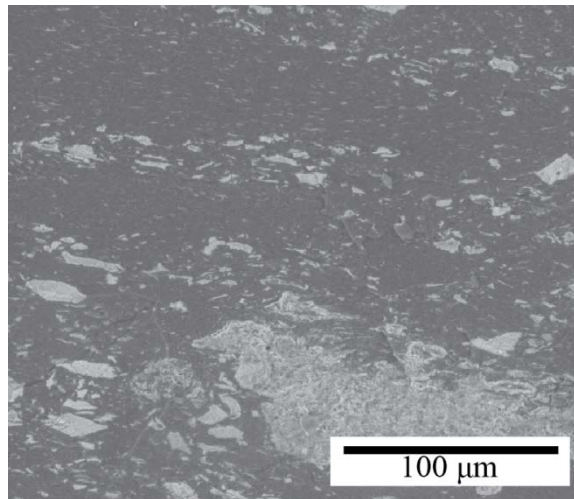


Figure 30. SEM of sintered specimen showing inhomogeneity as a result of poor dispersion of starting powders.

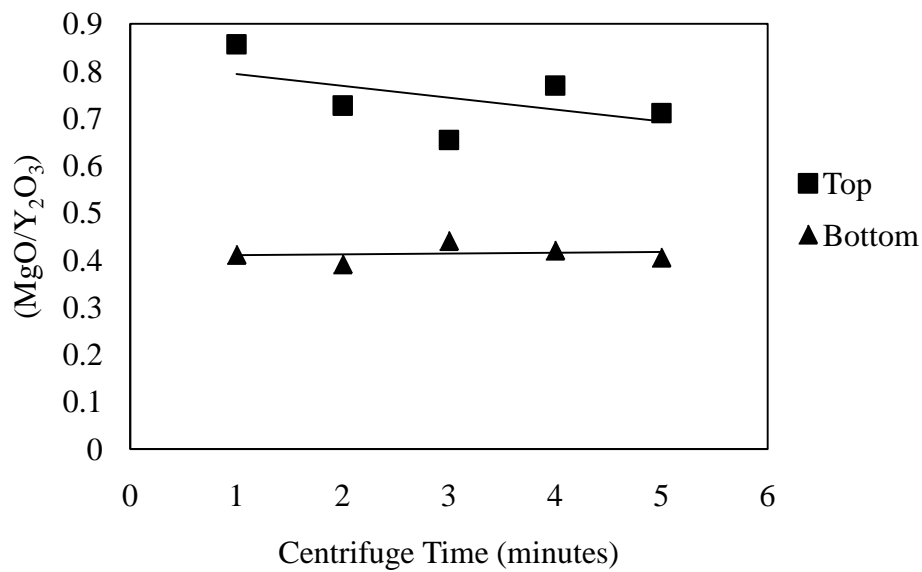


Figure 31. Graph showing the relative amounts of MgO and Y₂O₃ as collected from the top and bottom of centrifuge vials.

A milling procedure was required to increase homogeneity. The milling procedure was performed in anhydrous methanol. After milling, the solvent was evaporated and powders were crushed and calcined. The powders were still agglomerated after milling and before calcination, but after calcination they decreased in size. The mean particle size was roughly the same as unmilled powders. The milled and

calcined mean particle size was about 70 nm, as seen from DLS (Figure 32). The homogeneity was improved as seen in Figure 33.

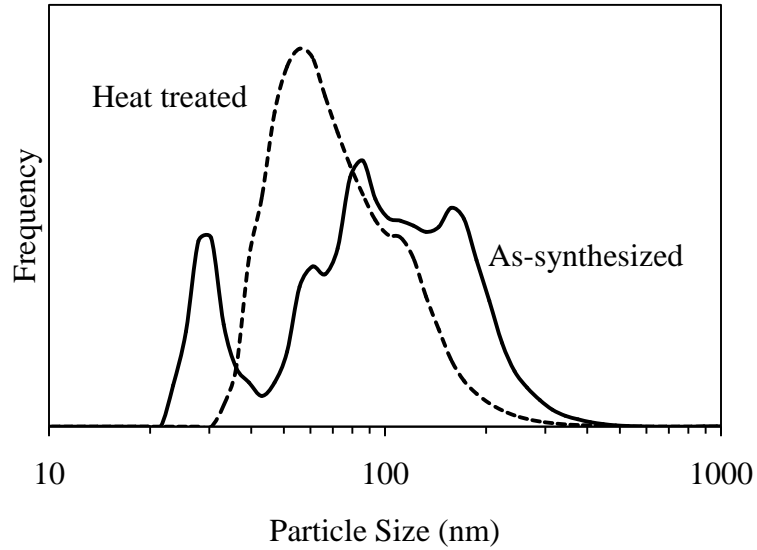


Figure 32. DLS after milling, before and after heat treatment of the MgO-Y₂O₃ composite powders synthesized by spray precipitation.

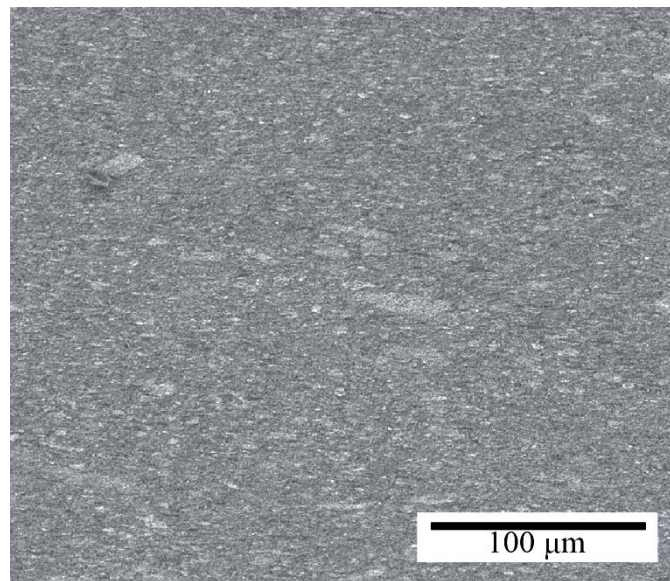


Figure 33. SEM of sintered specimen showing improved homogeneity after milling of the MgO-Y₂O₃ composite powders synthesized by spray precipitation.

C. Reverse Micelle Synthesis

1. Stability Studies

Before the reverse micelle system can be used for the synthesis of materials, the stability of the system in the presence of salts must be studied and understood. Dynamic light scattering is an essential tool in the understanding of stability. However, visual observations also play an important role.

For the study of stability for a constant water-to-surfactant ratio ($\omega_o=10$), magnesium nitrate was added to reverse micelle solutions in multiple concentrations. The stability of the system was determined by DLS and visual observation. The DLS data in Figure 34 displays the trend that micelle size decreases as ion concentration increases. Figure 35 displays the change in micelle size with relation to molarity of magnesium nitrate. The concentration at which micelle size does not change with increasing molarity is defined as the instability point, concentrations less than that are stable. As molarity increases the amount of charged ions in the water droplet increases.

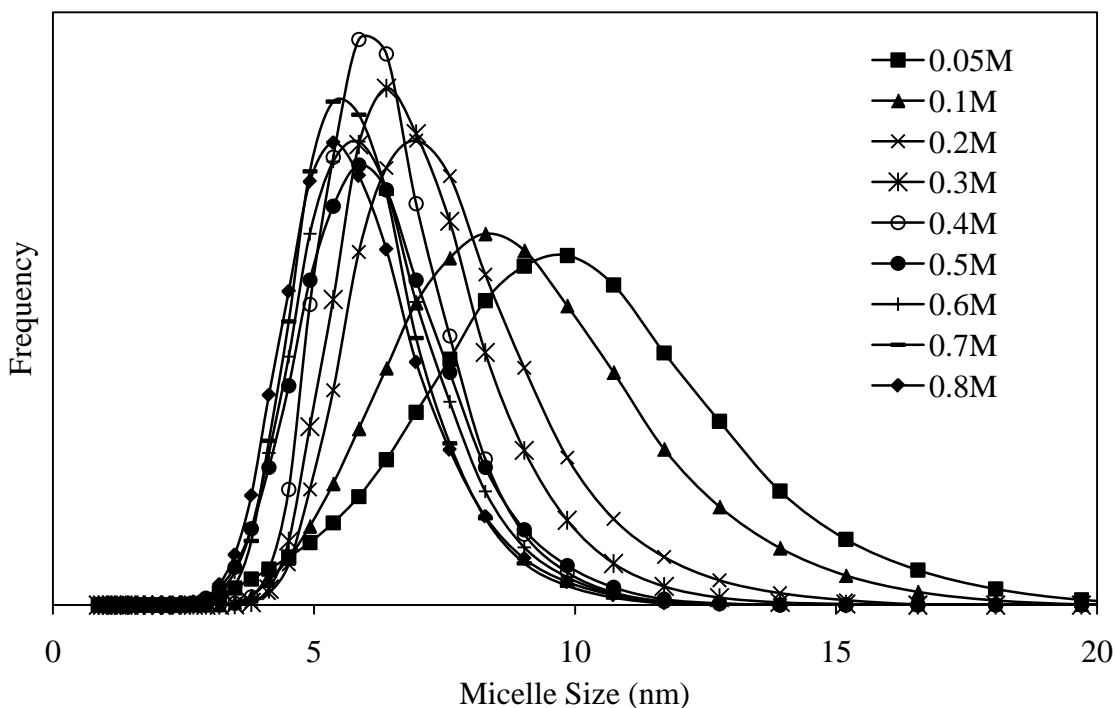


Figure 34. DLS data showing the effect of ion concentration of magnesium nitrate on the size of a reverse micelle in the AOT-isooctane-water system.

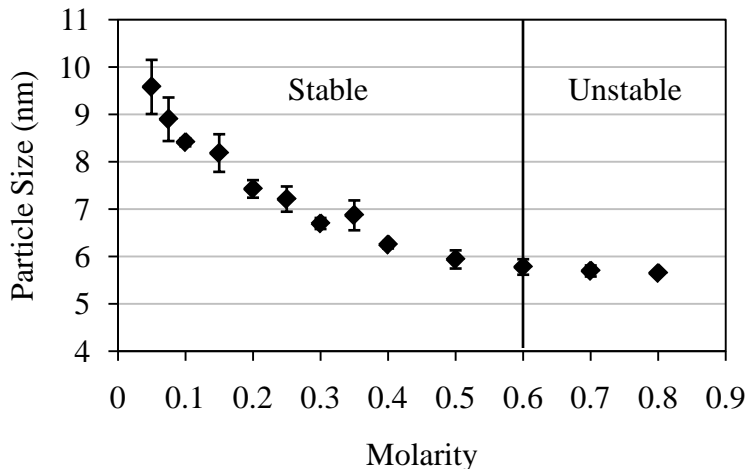


Figure 35. Graph displaying the change of micelle size with varying magnesium nitrate salt concentrations in the AOT-isooctane- water system with a $\omega_o=10$.

When system instability is present, it is often visibly apparent. A picture of an unstable solution can be seen in Figure 36. A destabilized solution will look cloudy as opposed to a clear solution. Often times water droplets can be seen in the bottom of the beaker.

Another factor that influences the destabilization concentration of the reverse micelle system is water-to-surfactant ratio. By using yttrium nitrate as the ion containing solution, three different water-to-surfactant ratios and their destabilization concentrations were explored. Figure 37 displays the change of particle size with varying yttrium nitrate concentrations, for different water-to-surfactant ratios. For this case, visual observation was used to determine the concentration of destabilization. For a $\omega_o=10$, $\omega_o=12.5$, and $\omega_o=15$ the concentration of destabilization was 0.3 M, 0.2 M, and 0.1 M, respectively.

To stay within the stable region during synthesis of the composite powders, an overall concentration of 0.3 M was chosen for the metal nitrate solution. This molarity allows for the addition of ammonium hydroxide to the system, for precipitation, and still stays within the stable concentration region.

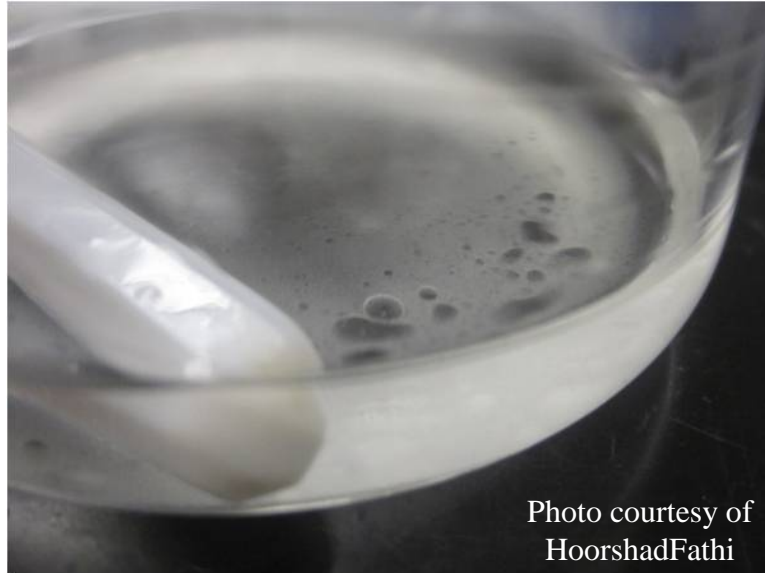


Photo courtesy of
HoorshadFathi

Figure 36. Representative picture of unstable reverse micelle solutions, for a molarity greater than 1, showing water coalescence on the bottom of beaker.

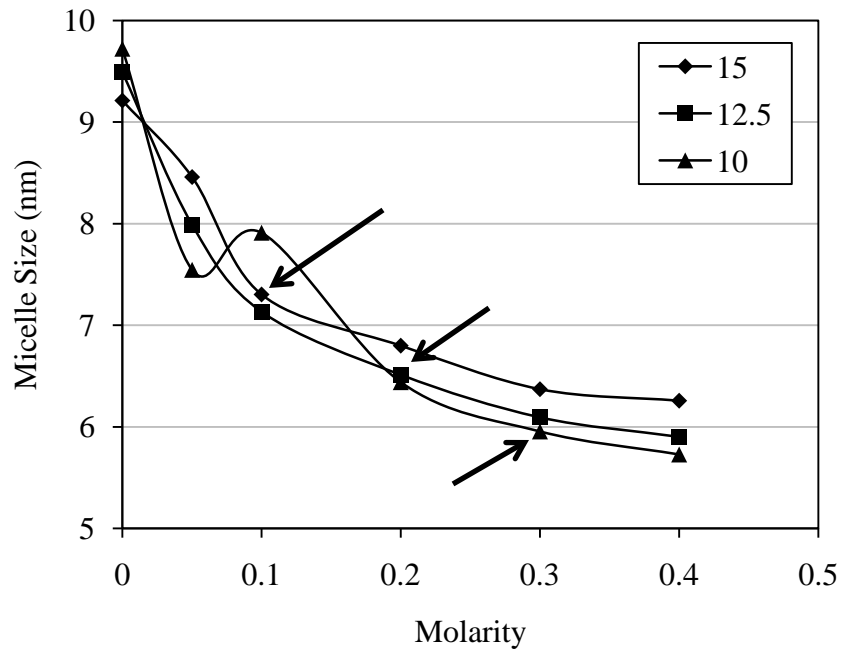


Figure 37. The effect of yttrium nitrate concentration on micelle size for $\omega_0=10$, $\omega_0=12.5$, and $\omega_0=15$. Arrows pointing to the concentration at which the solution is unstable for the particular ω_0 .

2. Precipitation in Reverse Micelles and Characterization

After the addition of the precipitation solution (isooctane and ammonium hydroxide) to the nitrate containing micelle solution, the solution should remain transparent, indicating stability is maintained. DLS was completed to confirm stability of the micelle system and the change in micelle size after precipitation can be seen in Figure 38. The size of the micelle does change by a significant amount.

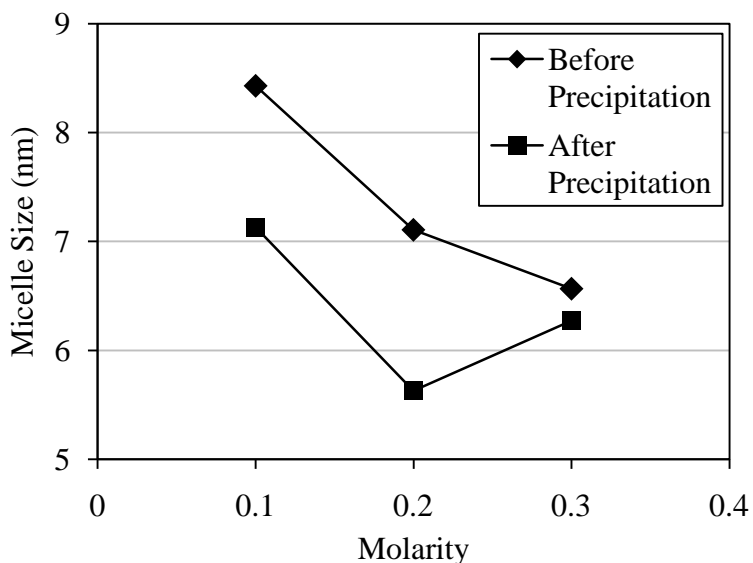


Figure 38. Change of micelle size after MgO-Y₂O₃ composite synthesis at 0.1 M, 0.2 M, and 0.3 M.

After precipitation, collection and washing was performed through a series of rinsing and centrifugation steps. If water was used as the first washing step, the powders would disperse, but were impossible to collect afterwards; therefore, ethanol was chosen as the first washing solvent. The water wash removed surfactant and excess ions in solution. The ethanol re-disperses the particles, which occurs during washing in water. To understand the effect of washing on particle size, DLS was performed after each washing step. One washing step refers to one wash with ethanol followed by one wash with water. As seen in Figure 39, one wash yields a large particle size. The particle size decreases as the number of washes increases. However, subsequent washes after the third wash lead to a re-agglomeration of the particles. This trend is seen before and after

calcination (Figure 39). Therefore, three washing cycles were chosen as sufficient for the de-agglomeration of the particles.

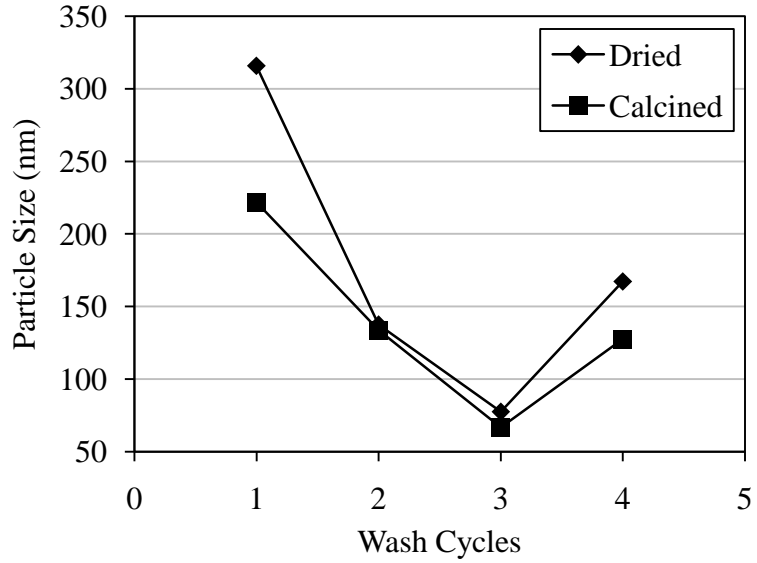


Figure 39. The influence of washing cycles on the mean particle size of synthesized MgO-Y₂O₃ composite powders synthesized by reverse micelle technique. (a) before calcination (dried), (b) after calcination at 1000°C.

Decomposition temperatures were comparable to those seen in previous synthesis methods. TGA data is shown in Figure 40. To ensure complete decomposition and densification, the powders were calcined at 1000°C for one hour.

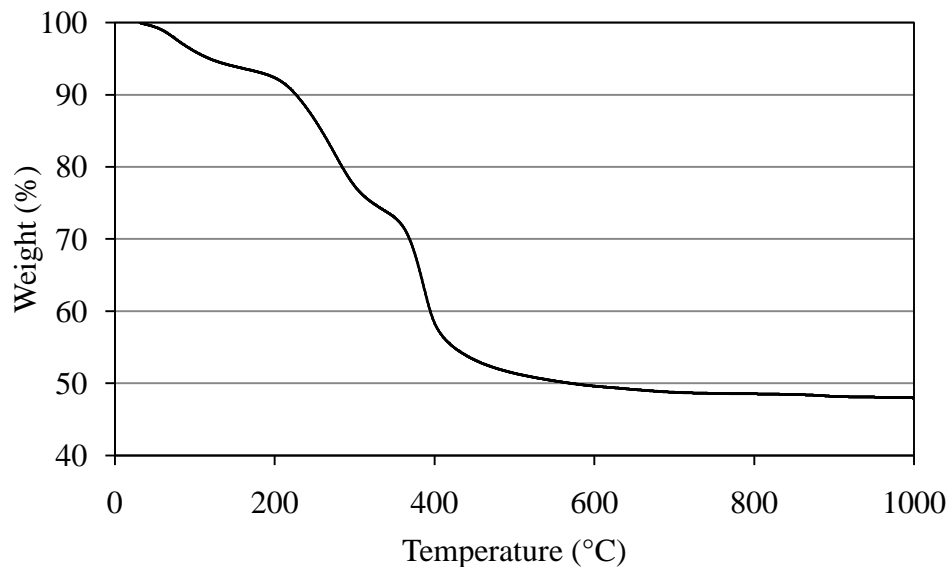


Figure 40. TGA plot showing the weight loss with respect to temperature, indicating decomposition of the composite hydroxides into MgO- Y_2O_3 composite powders synthesized by reverse micelle technique.

To further understand the phase transitions from a hydroxide to an oxide, in-situ high temperature XRD was performed. Figure 41 shows the data collected at various temperatures, compiled into one figure. From room temperature up to about 320°C the hydroxide phase is present. At a temperature of about 330°C the MgO starts to form. At temperatures around 550°C a monoclinic Y_2O_3 phase is seen. Using crystal structure analysis techniques in Jade software the mineralogy is determined to be monoclinic.

As seen before in the previous time-resolved XRD data in Figure 27, the uncalcined powders are a crystalline form of the hydroxide. At the explored temperatures, the MgO and Y_2O_3 do not interact, meaning it is a true two-phase composite. The results are similar to those seen before, however the Y_2O_3 is stabilized into a monoclinic structure. Crystallite sizes were analyzed and plotted on a chart, seen in Figure 42. As expected the crystallite size increases as temperature increases. The crystallite size of the Y_2O_3 could not be analyzed since peak overlap was present.

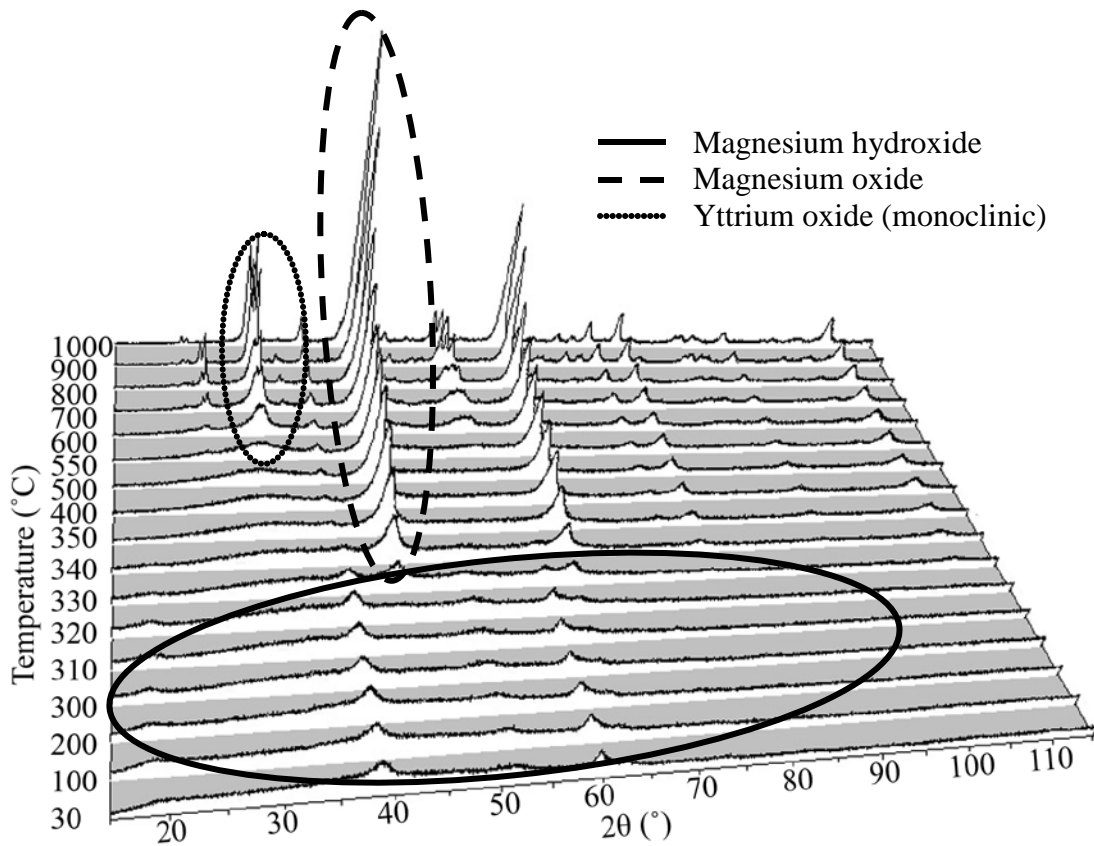


Figure 41. In-situ high-temperature (ranging from room temperature to 1000°C) XRD patterns of as-synthesized MgO-Y₂O₃ composite powders synthesized by reverse micelle technique. Circled peaks indicate peaks corresponding to a particular phase and mineralogy as shown in the legend.

After performing a heat treatment at 1000°C for one hour XRD analysis was conducted to obtain accurate crystallite sizes. The XRD pattern is shown in Figure 43. The crystallite size of MgO was calculated to be 20.8 ± 4.3 nm. Y₂O₃ could not be analyzed since the spectra did not contain significant peaks that were not overlapping.

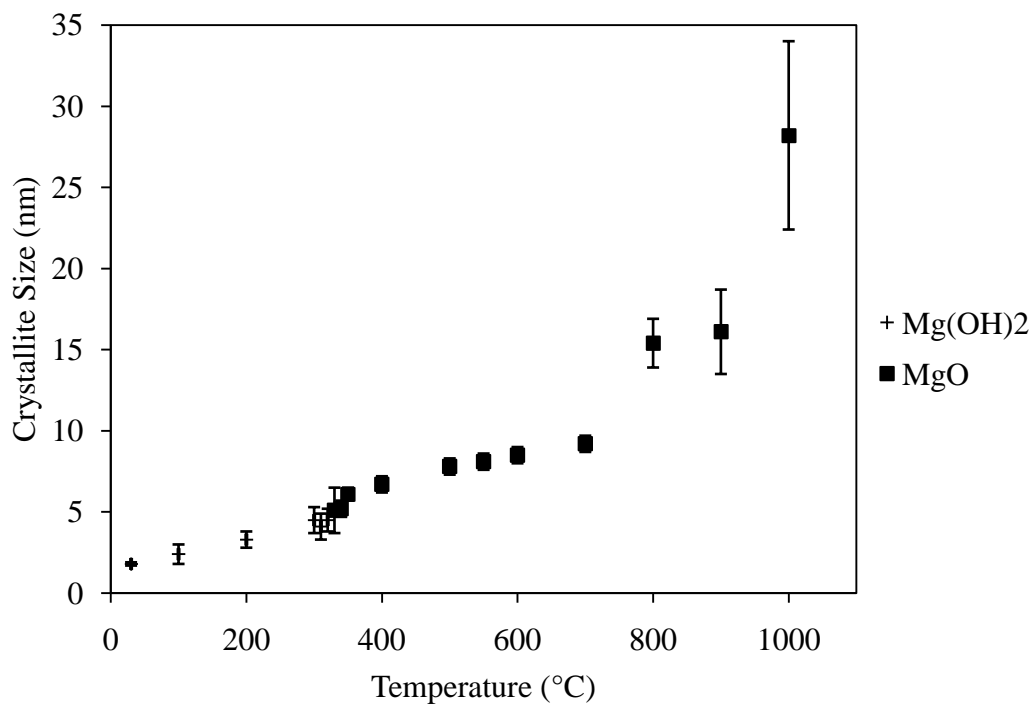


Figure 42. Graph displaying the crystallite growth, from XRD, with respect to temperature.

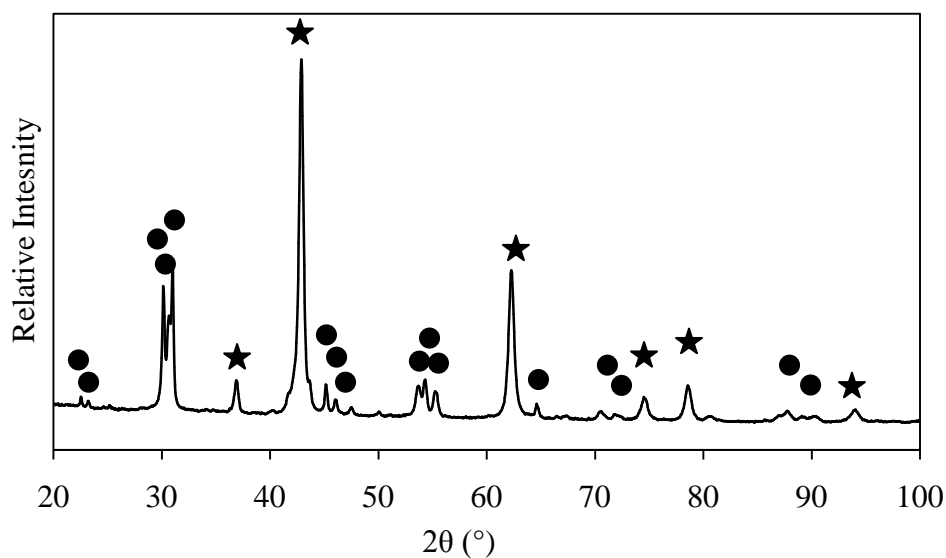


Figure 43. XRD pattern of calcined MgO- Y_2O_3 composite powders synthesized by reverse micelle technique calcined at 1000°C for one hour. Peaks indicated by circles are representative peaks for the monoclinic phase of Y_2O_3 . Peaks indicated by stars are representative peaks for the MgO PDF 00-045-0946.

Particle size analysis of heat-treated powders reveals a mean particle size of about 60 nm. The DLS data can be seen in Figure 44.

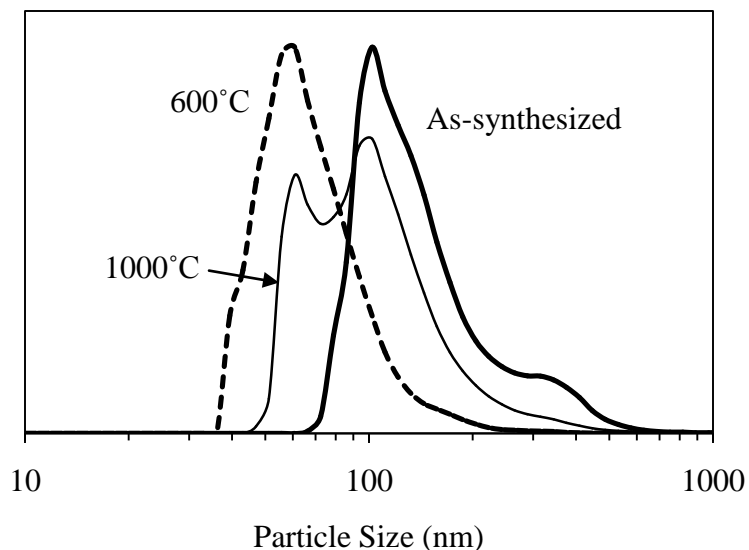


Figure 44. DLS of as-synthesized and heat-treated (600°C and 1000°C) MgO- Y_2O_3 composite powders synthesized by reverse micelle technique.

To gain a better understanding of the powder's morphology TEM was performed on as-synthesized, 600°C calcined, and 1000°C calcined powders, shown in Figure 45. The as-synthesized powders look large, amorphous, and agglomerated. Clear images of the nano-scale structure of as-synthesized powders was difficult to obtain.

After calcination, the powders were crystalline and showed less of this porous structure. These particles are smaller than the as-synthesized powders, due to crystallization and densification. When this happens the agglomerates break up into smaller particles. Heat treatment at higher temperatures leads to a slight amount of necking and coarsening of the particles, shown in Figure 45(c). Agglomerates are mostly seen throughout the powders, but small particles around the size of a micelle have been found, as presented in Figure 46.

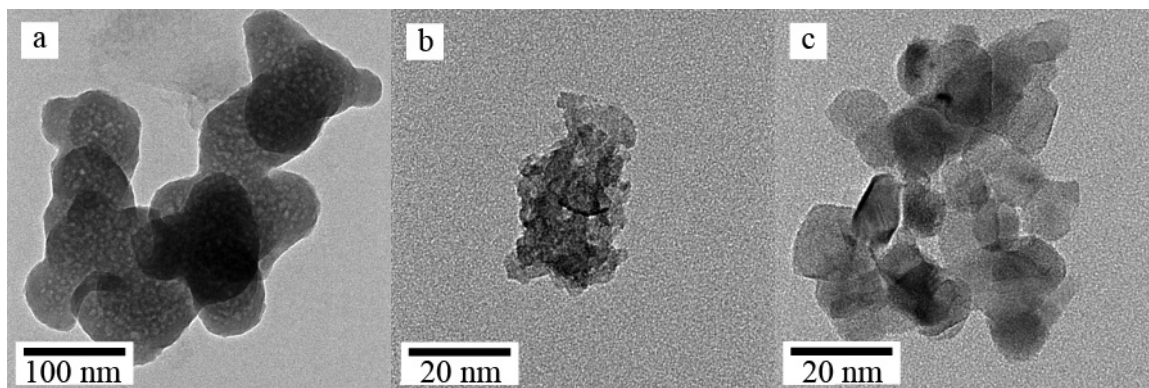


Figure 45. TEM micrographs of (a) as-synthesized and (b) 600°C and (c) 1000°C calcined MgO-Y₂O₃ composite powders synthesized by reverse micelle technique.

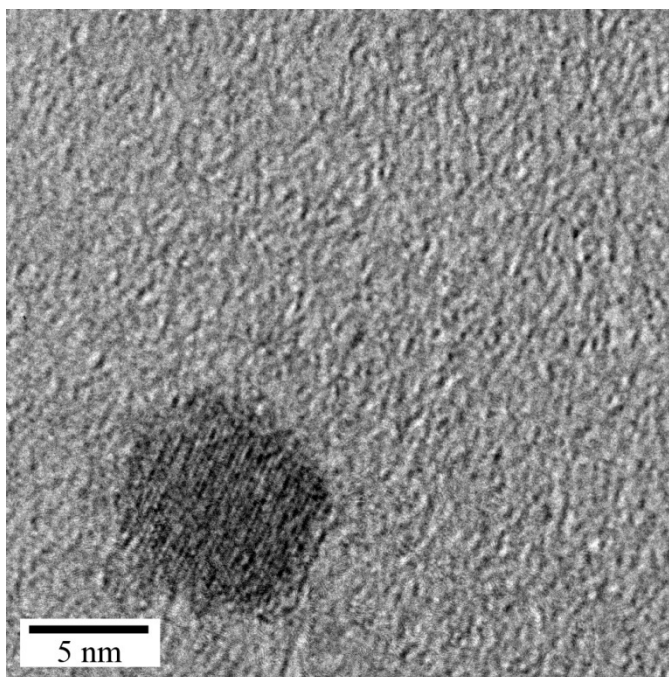


Figure 46. TEM micrograph of a composite powder particle with the size of a reverse micelle.

The surface area of as-synthesized powders is 150 m²/g, by BET. Particle size is estimated to be 10 nm. The surface area of heat-treated powders is 80 m²/g. The estimated particle size is about 19 nm.

D. Spark Plasma Sintering

1. Low Pressure Sintering

Spark plasma sintering experiments using graphite dies were difficult. Optimum sintering parameters were not determined for this die configuration. Using moderate pressures (<100 MPa), dense samples (>90%) could only be obtained using high temperatures. This however was undesired since the grains grew quite large and full density could still not be obtained. An example of this can be seen in Figure 47.

To increase final sintered density and smaller grain sizes higher pressures were needed. This particular graphite die configuration cannot withstand pressures much greater than 130 MPa at elevated temperatures. Not surprisingly, when using pressures greater than 100 MPa to sinter the composite material, die failure was seen almost every time.

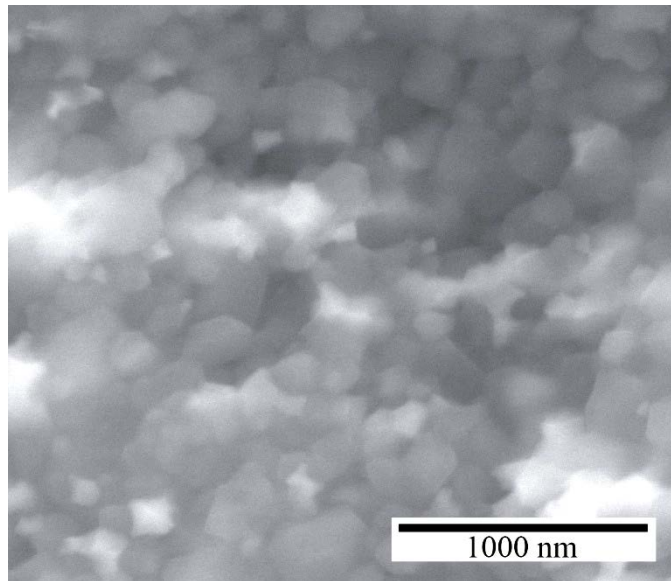


Figure 47. BSE SEM of SPS sintered composite, synthesized by spray precipitation. A temperature of 950°C and pressure of 75 MPa was used. Density is 85% and grain size is about 90 nm.

Sintering the spray precipitated composite powders to full density and small grain size with normal graphite dies was unsuccessful. High pressures using the conventional graphite die setup were not consistently obtainable and higher temperatures were not desired. A method of obtaining higher pressures had to be explored.

2. High Pressure Sintering

By using a double die design as shown in Figure 12, pressures up to 500 MPa were obtained. Silicon carbide has a much higher compression strength than graphite at temperature, therefore, higher pressures can be used. Since graphite components are still being used, the pressure application method is still important. After many trial and error attempts, it was determined that the sintering procedure described in the experimental procedure and illustrated in Figure 13 was the only procedure that would result in consistently successful sintering cycles.

Five samples were sintered using the spray precipitation composite powders at 1000°C and pressures of 300-500 MPa in 50 MPa increments. High-resolution SEM micrographs for each sample can be seen in Figure 48. One sample was sintered following the same heating profile, but at 38 MPa (the minimum pressure applied during segments one and two of Figure 13). One sample of the reverse micelle synthesized composite powders was sintered at 1000°C and 500 MPa, to be compared with the spray precipitation composite powders. A representative micrograph of this sample is displayed in Figure 49.

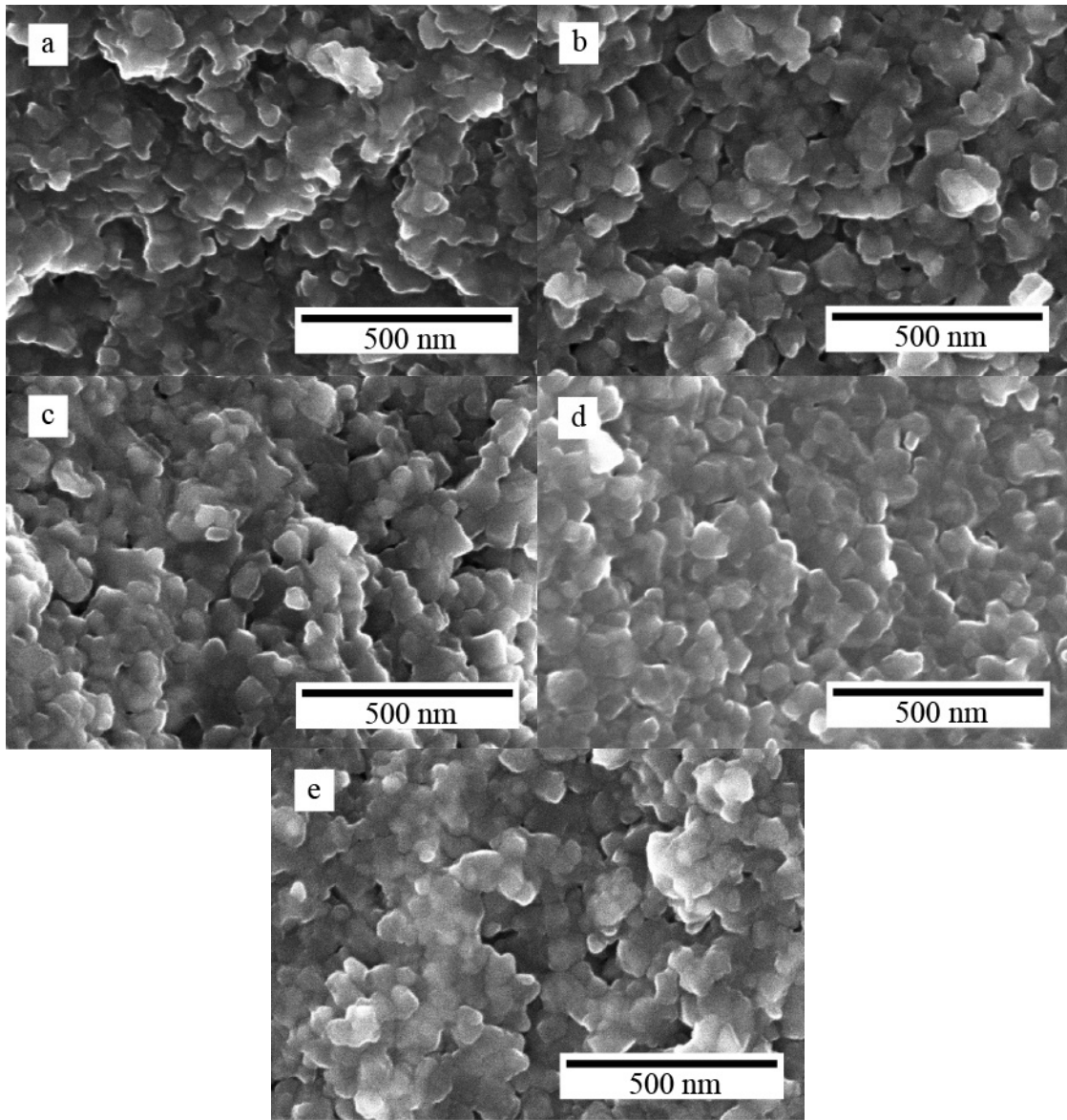


Figure 48. Fracture surface SEM of MgO-Y₂O₃ composite powders synthesized by spray precipitation, sintered using high-pressure SPS technique at (a) 300 MPa, (b) 350 MPa, (c) 400 MPa, (d) 450 MPa, and (e) 500 MPa.

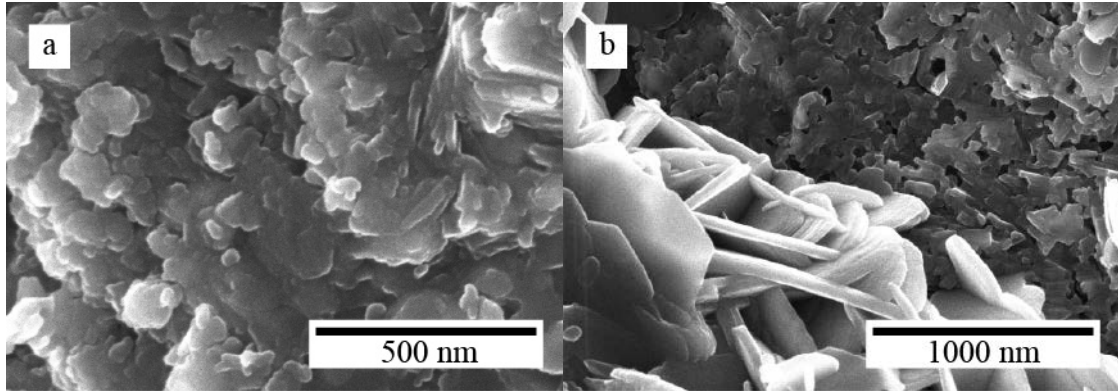


Figure 49. Fracture surface SEM of MgO-Y₂O₃ composite powders synthesized by reverse micelle technique, sintered using high-pressure SPS technique at 500 MPa (a) small grain microstructure (b) mixed microstructure.

Density of the samples is illustrated in Figure 50. It is noted that the samples sintered at pressures above 300 MPa hover around 90% density. There is a definite increase in density from 38 MPa to 300 MPa. To increase the final sintered density the sintering profile must be optimized. Nevertheless these high pressures were able to keep grain growth to a minimum. Final grain sizes for the spray precipitation powders has been measured, averaged, and presented in Figure 51. In all instances the average grain size is around 60 nm, which is the starting mean particle size of the powders.

The sintered specimen of the reverse micelle synthesized powders displays some peculiar results. As seen in Figure 49(b), the microstructure contains two very different regions. One region has small grains with an average size of 35 nm. The other region contains large plate-like grains, with an average thickness of 75 nm and average width of 700 nm.

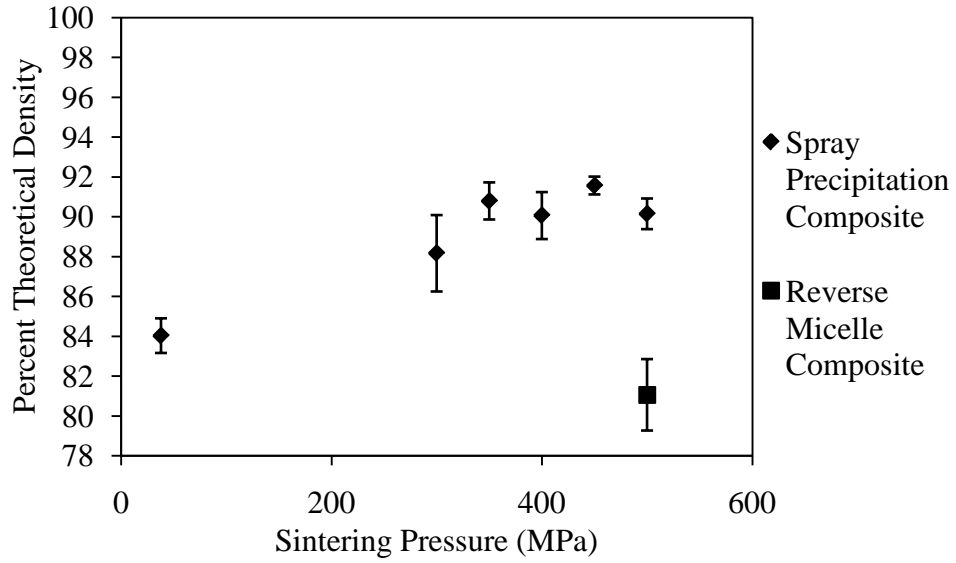


Figure 50. Graph showing the effect of pressure on the density of high-pressure SPS sintered samples.

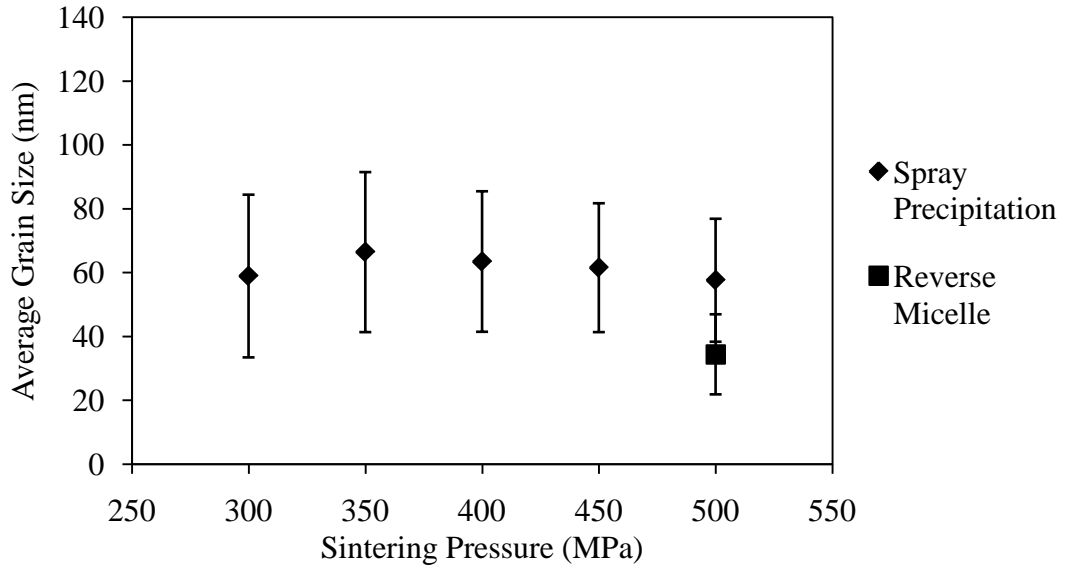


Figure 51. Graph showing the effect of pressure on the final grain size of high-pressure SPS sintered samples.

DISCUSSION

A. Reverse Micelle Stability

Before discussing synthesis results, the stability of the reverse micelle system must be understood. This is done by studying the effect of ion concentration in the micelle as well as changing the water to surfactant ratio.

By adding metal ion containing salts to the water droplets in a reverse micelle, the hydrodynamic radius changes. By increasing the positive ion concentration the size of the micelle decreases, displayed in Figure 34, Figure 35, and Figure 37. The surfactant heads are negatively charged, so when the positive charge inside the micelle increases the surfactant is drawn closer to the center. A point is reached where the micelles cannot shrink any further due to the repulsion of the surfactants being too close together. An illustration of this effect can be seen in Figure 52. In this instance, the concentration for instability is 0.6 M for magnesium nitrate and 0.3 M for yttrium nitrate. These points of instability are defined as the concentrations where micelle size does not change after higher concentrations are added and coalescence of water droplets can be seen. An unstable reverse micelle solution can be seen in Figure 36. Yang and Chen,⁸⁴ using DLS characterization techniques, witnessed the trend of decreasing micelle size with increasing ion concentration, however specific results were not presented and no indication of stability was mentioned.

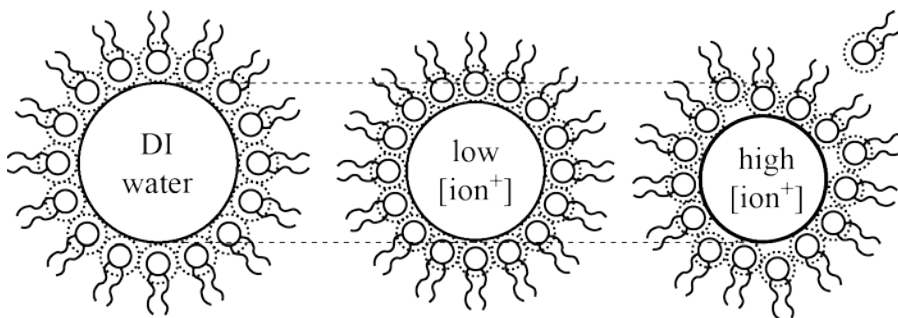


Figure 52. Diagram of a reverse micelle shrinking in size due to charge effects, eventually causing an unstable micelle solution.

To change the water-to-surfactant ratio, the water concentrations remained the same and the amount of surfactant was changed. In this case, visual observation was used to determine the concentration of instability. For a $\omega_o=10$, $\omega_o=12.5$, and $\omega_o=15$ the concentration of instability was 0.3 M, 0.2 M, and 0.1 M, respectively. Yttrium nitrate was used as the ion containing salt. Bohidar *et al.*⁸³ studying the same isooctane-AOT-water system used DLS characterization as a method to determine micelle size with respect to water-to-surfactant ratio between 1 to 50. They discovered micelle size increases with an increase of water to surfactant ratio. They did not, however, give insight on stability or study the effect of metal ions in the water domains. The trend seen in Figure 37 shows a decrease of micelle size with an increase of water-to-surfactant ratio. The contradictory trend is due to the ions in the micelle. Depending on the ion concentration, the reverse micelle solution stabilizes to a particular size, due to the charge effects of the ions on the surfactant. When water-to-surfactant ratio is increased, less surfactant is present in the system and the micelle solution cannot stabilize at the desired micelle size, due to the lack of surfactant.

When performing the synthesis reaction in the reverse micelle, the stability of the solution is vital to produce unimodal and consistent materials. When adding the precipitation agent, the system's properties must not change significantly, to ensure controlled synthesis. The ammonium hydroxide contains 72% water, as indicated by the supplier. Water is immiscible in isooctane, so it will remain at the bottom of the solution when mixed together. This excess water will create issues if added to micelle solutions. Care must be taken to avoid the addition of this small amount of water. After the addition of the precipitating solution the reverse micelle size decreases slightly, seen in Figure 38. A metal ion concentration of 0.3 M inside a reverse micelle solution with a $\omega_o=10$ was well within stability to perform synthesis.

B. Collection and Washing

1. Importance of Solvents

After synthesis, the collected hydroxide powders were washed once with ethanol. Figure 53 is a diagram that shows the different interaction of water and ethanol on the surface of a hydroxide, which is then calcined to form an oxide.¹³¹ When water is on the

surface of a hydroxide it can form links that bridge the particles together, due to the polar forces the water molecules contain. Ethanol creates hydrogen-terminated surfaces on the particles. When the hydroxide is calcined, the water or organics will vaporize. In the case of water, the surface is left with an oxygen bridge, causing agglomeration, whereas ethanol on the surface leads to a hydrogen terminated bond, which is less likely to result in bridging bonds and lead to agglomeration. Since the use of ethanol will help limit the agglomeration of powders, the powders are washed once in ethanol to remove all water from the surface of the powders after synthesis in water. By dispersing MgO in different solvents, Figure 14 shows ethanol is a better dispersing solvent than acetone and water.

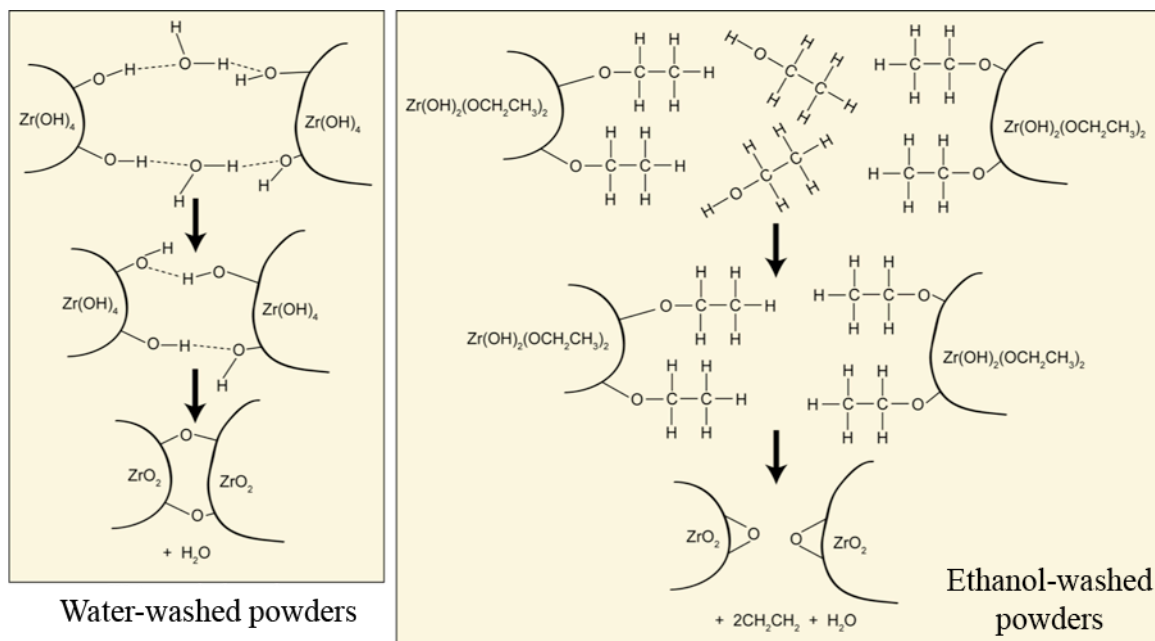


Figure 53. Proposed mechanisms of agglomeration when surfaces of a hydroxide contain water versus ethanol.¹³¹

2. Inhomogeneity

During collection and cleaning, phase separation occurred, making the powders inhomogeneous. Yttrium hydroxide is more dense than magnesium hydroxide; therefore, it will settle out of suspension faster. With extended centrifugation times the yttrium hydroxide will also be forced further to the bottom of the vial, increasing the severity of phase separation. Quantitative XRD, Figure 31, shows the ratio of MgO to Y₂O₃ is

different at the top and bottom of a centrifuge vial after centrifugation, with more Y_2O_3 at the bottom. The powders are hand ground using a pestle and mortar after drying and calcination, however this method is not efficient enough to homogenize the powder. Therefore, a milling procedure was implemented. Ball milling is the most common process to break agglomerates and improve homogeneity, proven to be effective for composite materials.¹³² Methanol is a hygroscopic solvent, meaning it will absorb water. It is used as the suspension medium in the milling procedure to further remove water from the surface of the particles. Figure 30 is a representative SEM image of a sintered sample from poorly mixed powders. Figure 33 confirms homogeneity is improved after milling in methanol.

3. Reverse Micelle Washing

The reverse micelle synthesis technique is theoretically able to fabricate unimodally-sized and shaped materials around the size and shape of a reverse micelle. This, however, was proven difficult since collection and cleaning of the precipitated material impacts the agglomeration of the final powders. It was seen in the work by Singh and Graeve¹⁰⁰ that the solvent used during cleaning influenced the purity of the final powders. They found that hydrogen peroxide was effective at removing the AOT from the surface of the particles. However, the centrifugation steps cause agglomeration into larger particles.

The influence of washing is seen in Figure 39. The powders are agglomerated due to a tangling of the surfactant, but with significant washing the surfactant is removed and agglomeration is lessened. Subsequent washing leads to a re-agglomeration of the powders, due to excess centrifugation and forced agglomeration. Therefore, a careful washing procedure is required to obtain pure and unagglomerated powders.

C. Calcination Studies

1. Thermogravimetric Analysis

The decomposition of magnesium hydroxide into magnesium oxide (Figure 12) occurs at temperatures seen in literature, between 300-400°C.⁴⁶ The decomposition of yttrium hydroxide into yttrium oxide (Figure 18) also occurs at temperatures seen in the

literature, between 400-600°C.⁵⁸ The composite hydroxide is expected to decompose into the oxide around the same temperature and be fully decomposed at 600°C, and is confirmed by TGA as seen in Figure 21, Figure 25, and Figure 40. The overall weight loss of the reverse micelle synthesized powders (Figure 40) is about 10% greater than the chemical precipitation methods. This extra weight loss is attributed to removal of residual organics or hydrocarbons from the surface of the particles. The powders have a larger surface area, so there will be more organics absorbed on the surfaces. Also, due to the synthesis method, more organics could be present in the system.

2. X-ray Diffraction

Figure 27 and Figure 41, the in-situ high temperature XRD patterns, show that the uncalcined powders are a crystalline form of the hydroxide. This is due to the sample preparation in methanol. The methanol removes water from the hydroxide and forms a crystalline hydroxide phase on the surface of the particles.¹³³ High-temperature XRD of the spray precipitation powders (Figure 27) shows a monoclinic phase of Y_2O_3 at temperatures below 600°C. The cubic phase is stabilized after heat treatment to higher temperatures. At the tested temperatures, the MgO and Y_2O_3 do not interact, meaning it is a true two-phase composite. In Figure 42, the in-situ high temperature XRD data of the reverse micelle powders, the peaks corresponding to the yttria phase do not fit any available PDF cards. By using crystal structure analysis, in the Jade software, from the peaks available, the yttria pattern data represents a monoclinic phase. One possible explanation for the different Y_2O_3 phase development is due to preferential crystal growth on the alumina substrate, as well as the specimen's surface cracking which results in uneven surfaces during decomposition and densification during heating, since decomposition and crystallization is occurring during the experiment.

3. Importance of Calcination Temperature

It was discovered that magnesium oxide and yttrium oxide powders calcined to 1000°C have optimum sintering characteristics.^{54,56} Since the goal is to have a highly sinterable powder, powder processing is important. The use of a higher temperature than 1000°C is not optimal since it will lead to exaggerated crystallite growth and necking between particles. Necking between particles is not desired, since this is considered hard

agglomeration. Unagglomerated particles can be pressed to higher green densities allowing for full densification at lower temperatures and shorter times, compared to agglomerated, low green density samples.^{23,24}

As-synthesized powders have a larger particle size than the calcined powders. This trend is presented in Figure 54 for all the powders synthesized. Imaging of the powders by TEM also confirms this, seen in Figure 16, Figure 23, Figure 29, and Figure 45. This is because the as-synthesized powders are hydroxides. During calcination the hydroxyls are eliminated and increase density, resulting in a smaller size. Also, crystallization of the powders leads to cracking of the particles that further decreases the size. Literature has yet to confirm this trend that particle size decreases when a hydroxide is calcined into an oxide for these materials by DLS, but Green³⁵ has discussed this trend in MgO and Huang *et al.*⁵⁶ witnessed this in SEM for Y₂O₃.

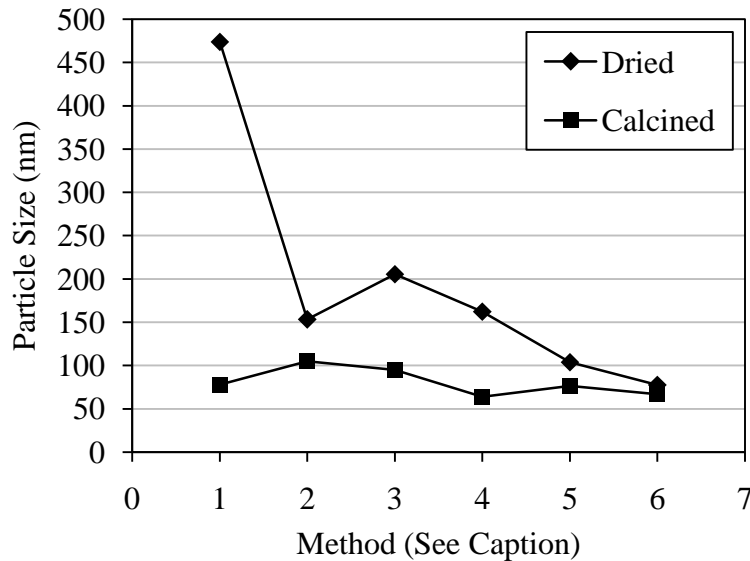


Figure 54. Change in mean particle size before and after characterization for (1.) MgO by chemical precipitation (2.) Y₂O₃ by chemical precipitation (3.) MgO-Y₂O₃ by chemical precipitation (4.) MgO-Y₂O₃ by spray precipitation (5.) MgO-Y₂O₃ by spray precipitation, milled (6.) MgO-Y₂O₃ by reverse micelle synthesis

As-synthesized powders synthesized by the reverse micelle technique have a greater surface area than calcined powders since the as-synthesized powders are highly

porous, made from agglomerated particles around the size of a micelle. As the powder is heat-treated it densifies and the particles coarsen, lessening the surface area.

After calcination of the composite material, the yttria component had a smaller crystallite size compared to magnesia. The concentration of yttrium ions during the precipitation procedure is much less than the magnesium ions. Therefore, the higher dispersion and lower concentration of yttrium ions in solution leads to the formation of smaller crystallites. A comparison of particle size and crystallite size for the given synthesis techniques is displayed in Figure 55.

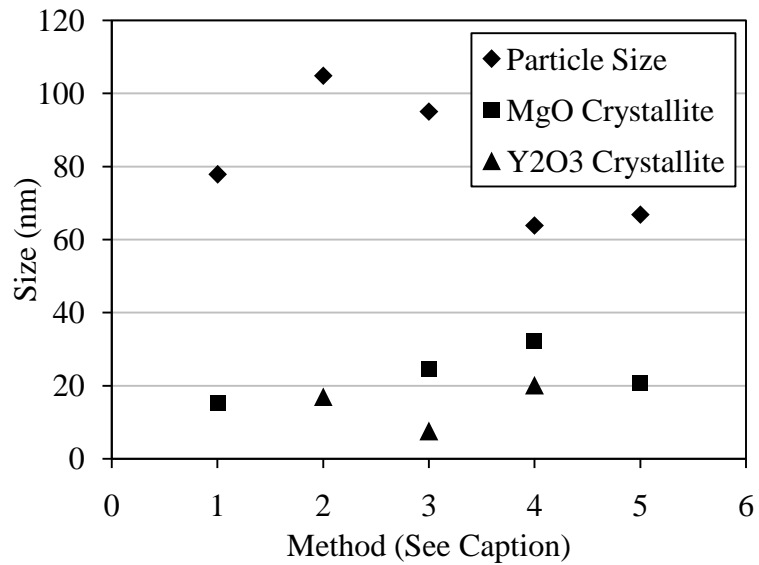


Figure 55. Comparison of particle size to crystallite size for (1.) MgO by chemical precipitation (2.) Y₂O₃ by chemical precipitation (3.) MgO-Y₂O₃ by chemical precipitation (4.) MgO-Y₂O₃ by spray precipitation (5.) MgO-Y₂O₃ by reverse micelle synthesis (Note: Y₂O₃ crystallite size was not measured)

D. Comparison of Powders by Different Synthesis Methods

Literature shows MgO and Y₂O₃ synthesized via chemical precipitation routes result in platelet-like morphologies.^{50,58} The conventional chemical precipitation method yields results which are comparable to those seen in literature. However, this method yields particles which are larger than desired.

By spraying the nitrate solution using an ordinary spray bottle, the solution was atomized and formed tiny ion-containing droplets. The droplets come into contact with the dilute ammonium hydroxide solution and the precipitate was formed. Due to the small droplet size of dilute nitrate solution and the dilute solution of ammonium hydroxide a small amount of Mg^{2+} and Y^{3+} ions are in the vicinity of OH^- ions. Therefore the precipitated particles are smaller than those made by a conventional precipitation technique.

By utilizing the reverse micelle system for controlling the size of precipitated powders, smaller particles can be synthesized. This method is difficult, however, because the washing and collection leads to agglomeration of the powders, resulting in a particle size that is similar to that of the spray precipitation powders.

Of the three methods investigated for the synthesis of the composite material, the one which resulted in the smallest particle size, obtained by DLS, were the powders synthesized by spray precipitation. A comparison of the final powders can be seen in Figure 56.

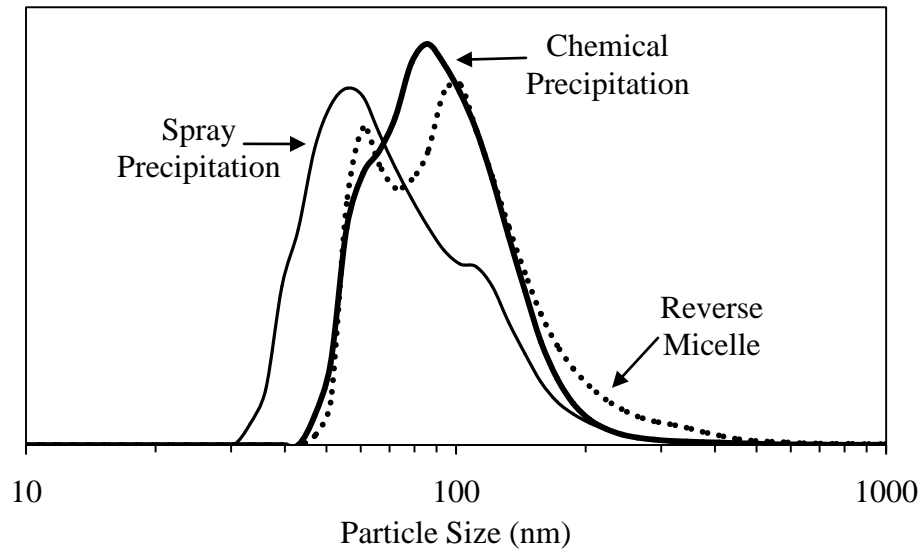


Figure 56. DLS comparison of the final composite powders synthesized by all three methods.

The particle size of spray precipitation powders is the smallest, but the crystallite sizes of the reverse micelle powders are smaller, Figure 56 and Figure 55. This leads to

the assumption that the reverse micelle powders have a slightly higher level of agglomeration. The severity of agglomeration, meaning hard or soft, is important since it will affect the sinterability of the powders. Softly agglomerated powders could possibly break apart under high pressure. Whereas hard agglomerated powders, coarsened with necks combining adjacent particles, will be more difficult to break and rearrange even with high pressure.

E. Spark Plasma Sintering

1. Low Pressure SPS

Common graphite SPS dies have a maximum limit of approximately 150 MPa, which is nearing the compressive strength of the graphite supplied. Application of pressure at different times during the sintering profile plays an important role on the die's ability to survive. When the full pressure was applied at the beginning of the sintering run, failure occurred at some point during heating. Application of the full pressure at final sintering temperature also proved to be unsuccessful. This is also undesired since particle necking and grain growth can occur at elevated temperatures when high pressures are not applied, increasing the difficulty of densification.

The best results were when pressure was applied slowly over the temperature ramp step. This can be seen in Figure 11. Graphite exhibits an increase of strength with increasing temperature. This is why applying pressure slowly and only obtaining the high pressures at elevated temperatures will result in less die failures. In any instance when the die did not break and a sample with a greater density than 90% was achieved, the specimen always came out of the die in many fractured pieces.

The phenomenon of broken samples was seen in Jiang and Mukherjee's work.⁷⁰ They identified a temperature range in which desired samples were obtained, but a temperature greater than that lead to the fracture of samples and a temperature lower than that was unable to densify the compact. An explanation of the occurrence was not given. One explanation can be due to constrained cooling. The CTE of the composite material is greater than that of graphite. When a force is maintained on the specimen while cooling occurs, the specimen contracts more than the graphite, however, the sample contraction is restricted by the force imparted by the graphite punches. Cracks are

formed in the sample to relieve the strain. To minimize the cracking of samples, one method could be to minimize the pressure at high temperature and then allow the sample to cool.

The sintering profile shown in Figure 11 is split into five sections. The first and second section is the simultaneous application of temperature and pressure. During the second segment displacement begins, this marks the beginning of densification. In segment three, the sintering temperature has been reached and densification continues during this dwell. Section four marks the completion of densification and the remaining dwell is to ensure densification has concluded. The length of this segment must be minimized to reduce grain growth. The fifth and final segment is the cooling segment. The power is turned off, force is released slowly and the die is allowed to cool naturally.

Sintering the spray precipitated composite powders to full density and small grain size with normal graphite dies was unsuccessful. High enough pressures were not consistently obtainable and higher temperatures were not desired due to the large grain growth observed. A method of obtaining higher pressures was necessary.

2. High Pressure SPS

The setup described and shown in Figure 12 was successful at obtaining pressures up to 500 MPa. A similar but smaller setup (inner die of 5 mm) has been recorded to obtain pressures nearing 1 GPa, however an inner die of 10 mm has only been seen in the literature and maximum pressures of 400 MPa are reported.^{111,113} This proposed die setup and sintering profile allows for a maximum pressure of 500 MPa.

The application of pressure for this setup was important, as it was for the common graphite die setup. Figure 13 is a graphical representation of the sintering profile as well as displacement information commonly seen in high pressure SPS. The figure has six regions, separated by dotted lines, where different events occur. The first region is the heating segment. In this segment, displacement begins just below the sintering temperature and the rate of displacement is fastest at the final sintering temperature (start of segment two). The pressures at this point are quite low (38 MPa), so full densification does not occur, and the displacement slows and stops shortly after the final sintering temperature is reached. The second region is a dwell at sintering temperature. This step is needed for the temperature equilibration of the large die. The third and fourth region is

where high pressures are applied. In the third region densification is seen by the change in displacement. The fourth region shows no change in densification, but a continuing increase of force. At this point, the majority of densification has occurred and the effects of the higher pressure are not known. The fifth region is a dwell at high pressure to ensure densification is concluded. The sixth region is the cooling segment. Power is turned off, the pressure is slowly released and the die is allowed to cool naturally.

3. Comparison of Results

Liu *et al.*⁶⁷ were able to achieve densities of 93.0-99.4% theoretical density of a MgO-Y₂O₃ composite with a different mixture ratio. The temperatures they used were slightly higher and pressures were much lower than used in these experiments. They discovered that temperature played the largest role on final density and grain size, both increased significantly with an increase in temperature. An increase of dwell time, at sintering temperature, lead to a slight increase in final density and a large increase in grain size. By increasing pressure, density increased significantly but grain size changes were not reported.

Jiang and Mukherjee⁷⁰ also studied the effect of temperature on the density and grain size of the same composite. Using a pressure of 80 MPa throughout their experiments, they discovered that 1200°C was sufficient in obtaining a sintered sample density of 99.1%. When increasing temperature from 1200-1600°C the grain size grew from 90 nm to 800 nm. The dwell had no effect on density and grain size trends were not recorded.

The powders synthesized by spray precipitation were unable to be sintered to full density by using similar parameters discussed in the literature. A representative SEM image of an often seen microstructure is shown in Figure 47, of a sample sintered at 950°C with a pressure of 75 MPa with a final density of ~85% and a grain size of ~90 nm. The powder morphologies were different in that the spray precipitation powders were more plate-like. This difference in morphology may result in poor particle packing and ultimately effect sintering. The type of agglomeration, hard or soft, cannot be compared and confirmed for certain, but it may also be an influencing factor on the inability to sinter to full density. Exploration of higher pressures may prove beneficial for the sintering to full density and limiting of grain growth.

According to Tamburini *et al.*,¹²⁸ the pressures required to obtain a sample with a relative density of 95% increases exponentially when temperature is decreased. For the case of 8 mol% yttria stabilized zirconia (YSZ) 30 MPa is required at 1350°C, but 530 MPa only requires 850°C. This decrease in temperature also drives the grain size down, near that of the starting powder's grain size, grain size of higher temperature samples is not stated. In the case of YSZ the starting powder grain size is 6.6 nm and the final grain size of a >98% dense sample, sintered at 850°C and 530 MPa is 15.5 nm.

In the sintering of the composite material the density only slightly increases with increasing pressure. Figure 50 charts the densities achieved by sintering at pressures of 38 MPa and between 300-500 MPa. A sample was sintered at 38 MPa, to be used as a baseline, and the density achieved was around 85%. A greater increase of density was expected when using higher pressures, but the inability to achieve densities greater than 90% is most likely attributed to the dwell at sintering temperature before high pressures are applied. This step (segment two in Figure 13) is possibly causing a presintering of the powders in a porous, coarsened, microstructure that is difficult to sinter even when high pressures are applied. Non-densifying sintering mechanisms, such as surface diffusion and surface lattice diffusion, create hard necks between adjacent particles. After the high pressure is applied, the densifying sintering mechanisms, such as grain boundary diffusion, lattice diffusion from the grain boundary, and plastic deformation are unable to achieve full densification and pore elimination. To increase the final sintered density the sintering profile must be optimized. This means shortening the initial dwell at sintering temperature, and also exploring slightly higher sintering temperatures.

Nevertheless these high pressures are able to keep grain growth to a minimum. This can be seen in the SEM micrographs of Figure 48 and Figure 49, as well as the chart displaying grain size with samples sintered at pressures of 300-500 MPa seen in Figure 51. If this is able to provide any insight on the importance of pressure, it should be that higher pressures could help limit grain growth during sintering, but other parameters must be optimized, specifically powder properties and sintering parameters.

Sintering of the reverse micelle composite powders, by high pressure SPS, shows two regions of very different microstructure, shown in Figure 49. The areas that contain small grains have an average grain size that is less than the starting powder mean particle

size. This could mean that the starting powders are softly agglomerated and when high pressures are applied these agglomerates break apart and the final sintered grain size is closer to that of the crystallite size. The other region contains large plate-like grains, it is hard to pinpoint what is the origin of the large plate-like grains, but it could be attributed to a variation in the synthesis method over time. The synthesis could be occurring outside of the micelle droplets, forming platelets similar to those seen in conventional chemical precipitation. Also, insufficient cleaning could lead to impurities and ultimately a difference in composition, resulting in a different sintering behavior. The massive inhomogeneity of the microstructure is likely the reason for the inability to sinter to a higher density.

SUMMARY AND CONCLUSIONS

To create optimum final ceramic products an understanding of the starting materials is paramount for successful and knowledgeable processing. In an ideal setting, the material properties can be tailored for certain applications. This was the aim of this project, with focus on nano-powder synthesis, processing, sintering, and characterization. Starting powders of the smallest size obtainable are important for the processing of optical ceramics that require extremely small final sintered grain sizes. Pure magnesium oxide, yttrium oxide, and composite powders can be synthesized by a normal precipitation method that yields mean particle sizes around 70, 85, and 105 nm, respectively.

To synthesize the composite powder with a smaller mean particle size, around 70 nm, a spray precipitation technique can be used. The slow addition, in the form of spray droplets, of the magnesium and yttrium ions to the dilute ammonium hydroxide solution allow for small particles to precipitate and stabilize in a less-agglomerated fashion. Powders synthesized using this method are pure, have an average crystallite size of less than 32 nm, and a platelet-like morphology.

This composite powder can also be synthesized by a reverse micelle technique that yields particles with a size around 60 nm, crystallite size of less than 20 nm, and somewhat agglomerated rounded-edge morphology. Stability of the reverse micelle system is extremely important for the synthesis of the ceramic composite. Since the water droplets inside the reverse micelles are the domains where precipitation reactions occur, the entire system must be stable throughout the process to ensure consistency and control over particle morphology. For the AOT-isooctane-water reverse micelle system a water-to-surfactant ratio of 10 and ion concentration less than 0.6 M is adequate to maintain stability for magnesium nitrate and 0.3 M for yttrium nitrate. This synthesis technique has such small yields that so many batches must be made to have enough powder for further characterization. Synthesizing multiple batches leads to variations in process and ultimately powder characteristics. A continuous synthesis method is one possibility for consistent results.

Spark plasma sintering can be used to sinter the composite material. This technique is much different than conventional methods because it uses fast heating rates, with constant application of uniaxial pressure. To keep the grain size small and limit grain growth, low sintering temperatures must be used. When high pressures are applied during sintering, the densification occurs more rapidly and at lower temperatures than conventional sintering methods.

Common pressures seen in SPS are less than 130 MPa, which is approaching the physical capability of the common graphite die configuration. A special die design, using silicon carbide components, was successful in applying pressures up to 500 MPa.

Powders synthesized by both methods can be sintered by high-pressure SPS to densities around 90% theoretical. By using high pressures during sintering the final sintered grain size can be related to that of the starting powder's particle and crystallite size. Depending on the severity of agglomeration, final sintered grain size may be driven towards crystallite size or particle size. For example, powders synthesized by the spray precipitation technique had a grain size of about 60 nm, whereas powders synthesized by reverse micelle technique had a grain size of about 30 nm (excluding the plate-like areas). Powders with soft agglomerates are proposed to break apart under high pressure, therefore final sintered grain sizes could be closer to that of crystallite size. Powders with harder agglomerates are likely to yield final sintered grain sizes closer to that of the initial powder mean particle size.

Densities greater than 90% were not achieved by SPS since optimized sintering parameters were not attained. Once the optimum heating and pressure profile is determined, higher densities are predicted to be achievable. The high pressures are proposed to limit the grain growth to the point where the final grain size is close to the starting particle size or even crystallite size. This trend is seen in the sintered specimens shown, however once higher densities are achieved the trend could be different. To reach full density, one method is to use higher temperatures. The current die setup was only capable of performing under the given parameters, so different temperatures could not be explored. Optical materials require extremely high densities, since any porosity will only act as a scattering sight and attenuate light transmission. Once full density is achieved optical and mechanical characterization can be performed.

FUTURE WORK

There are a few issues that must be addressed for further investigation in this project. The synthesis methods must be reevaluated to lessen agglomeration and improve phase mixing. The centrifugation step is likely attributing to agglomeration and phase separation. The excessive g-forces necessary for simple collection are forcing agglomeration of the powders. The chemical co-precipitation technique should theoretically achieve high levels of phase mixing due to the atomic mixing of the metal ions in solution. However, the centrifugation step is also causing the segregation of phases due to density differences. A less aggressive centrifugation step could be explored, or the supernatant could be evaporated, so that centrifugation is skipped altogether. In that case, the extent of milling necessary is reduced.

The reverse micelle synthesis technique has a few things that must be addressed. This method theoretically allows for the synthesis of materials with a controlled particle size. After the synthesis reaction occurs within the micelle, they must be collected and cleaned. The collection and cleaning step was performed using centrifugation, but this method has shown to agglomerate the powders, resulting in a large particle size. If the centrifugation is causing the micelle to rupture, lower g-forces could be used for longer times. Another method to collect these powders could be through the use of membranes, in an osmosis technique, to separate the synthesized powders from the solvent. The reverse micelle synthesis method also has very low yield. Synthesis scale-up experiments should be performed, perhaps with a continuous process. Also, to reduce costs associated with the oil and surfactant, recycling of the precursors should be explored.

Before the optical and mechanical properties of the material can be assessed, the material must be sintered to full density. The high pressure sintering cycle, shown in Figure 13, must be optimized for complete densification. The dwell after achieving 1000°C was necessary to allow the die to come to thermal equilibrium. This dwell should be shortened. Before modifications to the die are considered, one method to attempt for the final densification of the material is to increase the temperature. After the high pressure has been applied at 1000°C, the temperature can then be increased further

to activate the sintering mechanisms which dominate densification and the elimination of pores.

Modifications to the die which can aid in the optimization of the sintering cycle can be made. The inner die and outer die wall thicknesses can be reduced, so that the thermal mass is lessened and the thermal gradients are reduced. Also, silicon carbide is only conductive at high temperature. This means that the current flow is only through the graphite components at low temperatures. This will create large thermal gradients in the die. Using a material such as tungsten carbide, which is more conductive at lower temperatures, will allow for the current flow through all the components, hopefully allowing for current flow through the sample. The improved heating path with a lower thermal mass will allow for the application of high pressures after a shorter dwell when sintering temperature is reached. These physical modifications to the die configuration should allow for shortening of the dwell before high pressure is applied. This will minimize the particle necking and coarsening before high pressures are seen, so that higher densities can be achieved.

A study on the effects of particle size and agglomeration characteristics on the sintering of this powder system would be a significant contribution to the literature. An experiment could be performed that involves monomodal, highly dispersed, powders. The powders could then be heat treated at various temperatures and times to coarsen the powders and increase the severity of necking between the particles, effectively changing the agglomeration characteristics of the powders. The sintering behavior of these powders can then be studied using SPS to understand the effect of agglomeration on the ability to achieve full density and its influence on final grain size.

REFERENCES

1. D.C. Harris, "Durable 3-5 μm transmitting infrared window materials," *Infrared Phys. Technol.*, **39** [4], 185-201 (1998).
2. C.R. Seward, E.J. Coad, C.S.J. Pickles, and J.E. Field, "Liquid impact resistance of a range of IR-transparent materials," *Wear*, **186-187** [2], 375-83 (1995).
3. H.G. Blackwell, E.M. Waddell, D.R. Gibson, and P. McDermott, "Broadband IR transparent rain and sand erosion protective coating for the AV8-B and GR-7 Harrier forward-looking infrared germanium window," *Proc. SPIE*, **2776**, 144-58 (1996).
4. P. Klocek, J.T. Hoggins, and M. Wilson, "Broadband IR transparent rain erosion protective coating for IR windows," *Proc. SPIE*, **1760** [1], 210-23 (1992).
5. K.L. Lewis, C.J. Kelly, and B.C. Monachan, "Recent progress in the development of boron phosphide as a robust coating material for infra-red transparencies," *Proc. SPIE*, **1112**, 407-16 (1989).
6. E.M. Waddell, D.R. Gibson, and M. Wilson, "Broadband IR transparent rain and sand erosion protective coating for the F14 aircraft infrared search and track germanium dome," *Proc. SPIE*, **2286**, 376-85 (1994).
7. J. Szanyi, "The origin of haze in CVD tin oxide thin films," *Appl. Surf. Sci.*, **185** [3-4], 161-71 (2002).
8. J.A. Savage, *Infrared Optical Materials and Their Antireflection Coatings*; pp. 1-270. Taylor & Francis, Bristol, Boston, MA, 1985.
9. P. Klocek, *Handbook of Infrared Optical Materials*; pp. 1-630 Marcel Dekker, New York, NY, 1991.
10. D.W. Roy and G.G. Martin Jr., "Advances in spinel optical quality, size/shape capacity, and applications," *Proc. SPIE*, **1760**, 2 (1992).
11. S. Seal, S.C. Kuiry, P. Georgieva, and A. Agarwal, "Manufacturing nanocomposite parts: Present status and future challenges," *MRS Bull.*, **29** [1], 16-21 (2004).
12. M.J. Mayo, D.C. Hague, and D.J. Chen, "Processing nanocrystalline ceramics for applications in superplasticity," *Mater. Sci. Eng. A*, **A166** [1-2], 145-59 (1993).
13. Y.Z. S. Wang, X. Li, Y. Li, and K. Wang, "Coprecipitation of MgO-Doped ZrO₂ Nano Powder," *J. Am. Ceram. Soc.*, **89**, 3577-81 (2006).

14. O.A. Graeve and J.O. Corral, "Preparation and characterization of rare-earth-doped Y_2O_3 luminescent ceramics by the use of reverse micelles," *Opt. Mater.*, **29** [1], 24-30 (2006)
15. O.A. Graeve, H. Singh, and A. Clifton, "Synthesis and Consolidation of Zirconia Nanopowders via A Unique Reverse Micelle Synthesis Process and Spark Plasma Sintering," pp. 209-23 in *Pulse Electric Current Synthesis and Processing of Materials*. Edited by Z.A. Munir, M. Ohyanagi, M. Tokita, M. Khor, T. Hirai, U. Anselmi-Tamburini, John Wiley & Sons, Inc., New York, NY 2006.
16. V.V. Srdic, M. Winterer, and H. Hahn, "Sintering behavior of nanocrystalline zirconia doped with alumina prepared by chemical vapor synthesis," *J. Am. Ceram. Soc.*, **83** [8], 1853-60 (2000).
17. O.A. Graeve, S. Varma, G. Rojas-George, D.R. Brown, and E.A. Lopez, "Synthesis and characterization of luminescent yttrium oxide doped with Tm and Yb," *J. Am. Ceram. Soc.*, **89** [3], 926-31 (2006).
18. C. Li, T. Liang, and T. Luo, "Preparation of ZrO_2 nano-particles by the hydrolysis of $ZrOCl_2$ solution in the reverse micelles," *J. Univ. Sci. Technol. Beijing*, **13** [4], 355-8 (2006).
19. A. Pouchelon, J. Meunier, D. Langevin, and A.M. Cazabat, "Light scattering from oil-water interfaces: Measurements of low interfacial tensions," *J. phys. Lett.*, **41** [10], 239-42 (1980).
20. U. Anselmi-Tamburini, J.E. Garay, and Z.A. Munir, "Fast low-temperature consolidation of bulk nanometric ceramic materials," *Scr. Mater.*, **54** [5], 823-8 (2006).
21. U. Anselmi-Tamburini, J.E. Garay, Z.A. Munir, A. Tacca, F. Maglia, and G. Spinolo, "Spark plasma sintering and characterization of bulk nanostructured fully stabilized zirconia: Part I. Densification studies," *J. Mater. Res.*, **19** [11], 3255-62 (2004).
22. W. Chen, U. Anselmi-Tamburini, J.E. Garay, J.R. Groza, and Z.A. Munir, "Fundamental investigations on the spark plasma sintering/synthesis process: I. Effect of DC pulsing on reactivity," *Mater. Sci. Eng., A*, **394** [1-2], 132-8 (2005).
23. J.R. Groza and R.J. Dowding, "Nanoparticulate materials densification," *Nanostruct. Mater.*, **7** [7], 749-68 (1996).
24. J.R. Groza, "Nanosintering," *Nanostruct. Mater.*, **12** [5], 987-92 (1999).
25. J. Dutkiewicz, J. Kusnierz, W. Maziarz, M. Lejkowska, H. Garbacz, M. Lewandowska, A.V. Dobromyslov, and K.J. Kurzydowski, "Microstructure and mechanical properties of nanocrystalline titanium and Ti-Ta-Nb alloy

- manufactured using various deformation methods," *Phys. Status Solidi A*, **202** [12], 2309-20 (2005).
26. K. Morita, K. Hiraga, B.N. Kim, H. Yoshida, and Y. Sakka, "Synthesis of dense nanocrystalline ZrO_2 - $MgAl_2O_4$ spinel composite," *Scr. Mater.*, **53** [9], 1007-12 (2005).
 27. J. Hong, L. Gao, S.D.D.L. Torre, H. Miyamoto, and K. Miyamoto, "Spark plasma sintering and mechanical properties of $ZrO_2(Y_2O_3)$ - Al_2O_3 composites," *Mater. Lett.*, **43** [1-2], 27-31 (2000).
 28. U. Anselmi-Tamburini, J.E. Garay, Z.A. Munir, A. Tacca, F. Maglia, G. Chiodelli, and G. Spinolo, "Spark plasma sintering and characterization of bulk nanostructured fully stabilized zirconia: Part II. Characterization studies," *J. Mater. Res.*, **19** [11], 3263-9 (2004).
 29. W.H. MacIntire, "Process for Obtaining MgO and $CaCO_3$ from Dolomitic Materials," U.S. Pat. 2,137,675, November 1938.
 30. B.B.G. William S. Ainscow, Sulzer Brothers Limited, "Process for Producing Magnesium Oxide," U.S. Pat. 4,720,375 January 1988.
 31. H.A. M. Yildirim, "Preparation of Magnesium Oxide (MgO) from Dolomite by Leach-Precipitation-Pyrohydrolysis Process," *Physicochem. Probl. Miner. Process.*, [44], 257-72 (2009).
 32. E. Alvarado, L.M. Torres-Martinez, A.F. Fuentes, and P. Quintana, "Preparation and characterization of MgO powders obtained from different magnesium salts and the mineral dolomite," *Polyhedron*, **19** [22-23], 2345-51 (2000).
 33. A. Bhargava, J.A. Alarco, I.D.R. Mackinnon, D. Page, and A. Ilyushechkin, "Synthesis and characterization of nanoscale magnesium oxide powders and their application in thick films of $Bi_2Sr_2CaCu_2O_8$," *Mater. Lett.*, **34** [3-6], 133-42 (1998).
 34. F.C. Gilbert, W.C. Gilpin, "Production of magnesia from sea water and dolomite," British Periclase Company. Hartelpool, England, 1951.
 35. J. Green, "Calcination of precipitated $Mg(OH)_2$ to active MgO in the production of refractory and chemical grade MgO ," *J. Mater. Sci.*, **18** [3], 637-51 (1983).
 36. Y.C. Hong and H.S. Uhm, "Synthesis of MgO nanopowder in atmospheric microwave plasma torch," *Chem. Phys. Lett.*, **422** [1-3], 174-8 (2006).
 37. Y. Hao, G. Meng, C. Ye, X. Zhang, and L. Zhang, "Kinetics-driven growth of orthogonally branched single-crystalline magnesium oxide nanostructures," *J. Phys. Chem. B*, **109** [22], 11204-8 (2005).

38. J.L. Boldu O, L.A. Boatner, and M.M. Abraham, "Characterization of textured ceramics by electron paramagnetic resonance spectroscopy. II, formation and properties of textured MgO," *J. Am. Ceram. Soc.*, **73** [8], 2345-59 (1990).
39. R.B.J. Quincy, "Preparation of high-purity magnesium oxide," Oak Ridge National Lab, Oak Ridge, TN, 1962.
40. T.J. Gardner and G.L. Messing, "Preparation of MgO powder by evaporative decomposition of solutions," *Am. Ceram. Soc. Bull.*, **63** [12], 1498-501-504 (1984).
41. K. Chhor, J.F. Bocquet, and C. Pommier, "Syntheses of submicron magnesium oxide powders," *Mater. Chem. Phys.*, **40** [1], 63-8 (1995).
42. R. Portillo, T. Lopez, R. Gomez, Bokhimi, A. Morales, and O. Novaro, "Magnesia synthesis via sol-gel: Structure and reactivity," *Langmuir*, **12** [1], 40-4 (1996).
43. L. Znaidi, K. Chhor, and C. Pommier, "Batch and semi-continuous synthesis of magnesium oxide powders from hydrolysis and supercritical treatment of $Mg(OCH_3)_2$," *Mater. Res. Bull.*, **31** [12], 1527-35 (1996).
44. S. Chakrabarti, D. Ganguli, and S. Chaudhuri, "Preparation of hydroxide-free magnesium oxide films by an alkoxide-free sol-gel technique," *Mater. Lett.*, **57** [29], 4483-92 (2003).
45. Y. Du and D. Inman, "Synthesis of MgO powders from molten salts," *J. Mater. Sci.*, **32** [9], 2373-9 (1997).
46. F. Meshkani and M. Rezaei, "Effect of process parameters on the synthesis of nanocrystalline magnesium oxide with high surface area and plate-like shape by surfactant assisted precipitation method," *Powder Technol.*, **199** [2], 144-8 (2010).
47. D. Chen and E.H. Jordan, "Synthesis of porous, high surface area MgO microspheres," *Mater. Lett.*, **63** [9-10], 783-5 (2009).
48. W. Wang, X. Qiao, and J. Chen, "The role of acetic acid in magnesium oxide preparation via chemical precipitation," *J. Am. Ceram. Soc.*, **91** [5], 1697-9 (2008).
49. R. Llamas, C. Jimenez-Sanchidrian, and J.R. Ruiz, "Environmentally friendly Baeyer-Villiger oxidation with H_2O_2 /nitrile over $Mg(OH)_2$ and MgO," *Appl. Catal. B*, **72** [1-2], 18-25 (2007).
50. C. Henrist, J.P. Mathieu, C. Vogels, A. Rulmont, and R. Cloots, "Morphological study of magnesium hydroxide nanoparticles precipitated in dilute aqueous solution," *J. Cryst. Growth*, **249**, 321-30 (2003).

51. W. Wang, X. Qiao, J. Chen, and H. Li, "Facile synthesis of magnesium oxide nanoplates via chemical precipitation," *Mater. Lett.*, **61** [14-15], 3218-20 (2007).
52. D. An, X. Ding, Z. Wang, and Y. Liu, "Synthesis of ordered arrays of magnesium hydroxide nanoparticles via a simple method," *Colloids Surf. A*, **356** [1-3], 28-31 (2010).
53. S.W. Bain, Z. Ma, Z.M. Cui, L.-S. Zhang, F. Niu, and W.G. Song, "Synthesis of micrometer-sized nanostructured magnesium oxide and its high catalytic activity in the Claisen-Schmidt condensation reaction," *J. Phys. Chem. C*, **112** [30], 11340-4 (2008).
54. A.G. Allison, E.C. Sesler, N.L. Haldy, and W.H. Duckworth, "Sintering of high-purity magnesia," *J. Am. Ceram. Soc.*, **39** [4], 151-4 (1956).
55. C.J.J. Tool and E.H.P. Cordfunke, "Influence of precipitation on the microstructure and sinterability of yttria," *Solid State Ionics*, **32-33** [2], 691-7 (1989).
56. Z. Huang, X. Sun, Z. Xiu, S. Chen, and C.-T. Tsai, "Precipitation synthesis and sintering of yttria nanopowders," *Mater. Lett.*, **58** [15], 2137-42 (2004).
57. S. Sohn, Y. Kwon, Y. Kim, and D. Kim, "Synthesis and characterization of near-monodisperse yttria particles by homogeneous precipitation method," *Powder Technol.*, **142** [2-3], 136-53 (2004).
58. L. Wen, X. Sun, Q. Lu, G. Xu, and X. Hu, "Synthesis of yttria nanopowders for transparent yttria ceramics," *Opt. Mater.*, **29** [2-3], 239-45 (2006).
59. Y. Du and Z. Jin, "Thermodynamic assessment of the Y_2O_3 -MgO system," *J. Alloys Compd.*, **176** [1], L1-L4 (1991).
60. G.A. Chow and K.E. Gonslaves, "Particle Synthesis by Chemical Routes"; pp 55-7 in *Nanomaterials: Synthesis, Properties and Applications*. Edited by A. S. Edelstein, R. C. Cammarata. Taylor & Francis Group, New York, NY, 1996.
61. C.K. Muoto, E.H. Jordan, M. Gell, and M. Aindow, "Effects of precursor chemistry on the structural characteristics of Y_2O_3 -MgO nanocomposites synthesized by a combined sol-gel/thermal decomposition route," *J. Am. Ceram. Soc.*, **94** [2], 372-81 (2011).
62. J. Wang, E. Jordan, and M. Gell, "Plasma sprayed dense MgO- Y_2O_3 nanocomposite coatings using sol-gel combustion synthesized powder," *J. Therm. Spray Technol.*, **19** [5], 873-8 (2010).
63. J. Wang, D. Chen, E.H. Jordan, and M. Gell, "Infrared-transparent Y_2O_3 -MgO nanocomposites using sol-gel combustion synthesized powder," *J. Am. Ceram. Soc.*, **93** [11], 3535-8 (2010).

64. C.K. Muoto, E.H. Jordan, M. Gell, and M. Aindow, "Phase homogeneity in Y_2O_3 -MgO nanocomposites synthesized by thermal decomposition of nitrate precursors with ammonium acetate additions," *J. Am. Ceram. Soc.*, **94** [12], 4207-17 (2011).
65. C.H. Chen, J.K.M. Garofano, C.K. Muoto, A.L. Mercado, S.L. Suib, M. Aindow, M. Gell, and E.H. Jordan, "A foaming esterification sol-gel route for the synthesis of magnesia-yttria nanocomposites," *J. Am. Ceram. Soc.*, **94** [2], 367-71 (2011).
66. D.C. Harris, "Diamond and sapphire for infrared windows and domes" *Int. SAMPE Symp. Exhib.*, **42** [1] 641-51 (1997).
67. J. Liu, W. Yao, B. Kear, and A.K. Mukherjee, "Microstructure and IR transmittance of yttria-magnesia (50:50 vol.%) nano-composites consolidated from agglomerated and ultrasonic horn treated nano-powders," *Mater. Sci. Eng. B*, **171** [1-3], 149-54 (2010).
68. B.H. Kear, R. Sadangi, V. Shukla, T. Stefanik, and R. Gentilman, "Submicron-grained transparent yttria composites," *Proc. SPIE*, **5786**, 227-33 (2005).
69. R.G. T. Stefanik, and P. Hogan, "Nanocomposite optical ceramic for infrared windows and domes," *Proc. SPIE*, **6545**, 65450A1-5 (2007).
70. D. Jiang and A.K. Mukherjee, "Spark plasma sintering of an infrared-transparent Y_2O_3 -MgO nanocomposite," *J. Am. Ceram. Soc.*, **93** [3], 769-73 (2010).
71. F.F. Lange, M.L. Balmer, and C.G. Levi, "Diffusion limited crystallization and phase partitioning in ZrO_2 -metal oxide binary systems," *J. Sol-Gel Sci. Technol.*, **2** [1], 317-21 (1994).
72. B.L. Cushing, V.L. Kolesnichenko, and C.J. O'Connor, "Recent advances in the liquid-phase syntheses of inorganic nanoparticles," *Chem. Rev.*, **104** [9], 3893-946 (2004).
73. V. Uskokovic and M. Drofenik, "Synthesis of materials within reverse micelles," *Surf. Rev. Lett.*, **12** [2], 239-77 (2005).
74. J. Eastoe, M.J. Hollamby, and L. Hudson, "Recent advances in nanoparticle synthesis with reversed micelles," *Adv. Colloid Interface Sci.*, **128-130**, 5-15 (2006).
75. B.H. Robinson, "Colloid chemistry: Applications of microemulsions," *Nature*, **320** [6060], 309- (1986).
76. J. Eastoe and B. Warne, "Nanoparticle and polymer synthesis in microemulsions," *Curr. Opin. Colloid Interface Sci.*, **1** [6], 800-5 (1996).
77. M.-P. Pileni, "The role of soft colloidal templates in controlling the size and shape of inorganic nanocrystals," *Nat. Mater.*, **2** [3], 145-50 (2003).

78. *Structure and reactivity in reverse micelles (Studies in physical and theoretical chemistry)*; pp. 1-379. Edited by M. P. Pileni. Elsevier, Amsterdam, 1989.
79. C. Petit, P. Lixon, and M.P. Pileni, "In situ synthesis of silver nanocluster in AOT reverse micelles," *J. Phys. Chem.*, **97** [49], 12974-83 (1993).
80. N. Moumen, J. Cizeron, C. Petit, L. Motte, I. Lisiecki, and M.P. Pileni, "Synthesis 'in situ' of nanoparticles in reverse micelles," pp. 1-9 in Progress in Colloid Polymer Science, Vol. 93, *Trends in Colloid and Interface Science VII*. Edited by P. Lagginger and O. Glatter. Steinkopff, Dresden, Germany, 1993.
81. M.P. Pileni, I. Lisiecki, and L. Motte, "Nanometer particles synthesis in reverse micelles. Influence of the size and the surface on the reactivity," *Res. Chem. Intermed.*, **17** [2], 101- (1992).
82. M.P. Pileni, "Reverse micelles as microreactors," *J. Phys. Chem.*, **97** [27], 6961-73 (1993).
83. H.B. Bohidar and M. Behboudnia, "Characterization of reverse micelles by dynamic light scattering," *Colloids Surf. A*, **178** [1-3], 313-23 (2001).
84. C.F. Yang and J.Y. Chen, "Synthesis of stabilized zirconia ultrafine powders using AOT-isooctane-water reverse micelles," *J. Mater. Sci. Lett.*, **16** [11], 936-8 (1997).
85. S. Vaidya, J. Ahmed, and A.K. Ganguli, "Controlled synthesis of nanomaterials using reverse micelles," *Def. Sci. J.*, **58** [4], 531-44 (2008).
86. V. Ervithayasuporn and Y. Kawakami, "Synthesis and characterization of core-shell type Fe₃O₄ nanoparticles in poly(organosilsesquioxane)," *J. Colloid Interface Sci.*, **332** [2], 389-93 (2009).
87. J.-L. Lemyre, S. Lamarre, A. Beaupre, and A.M. Ritcey, "A new approach for the characterization of reverse micellar systems by dynamic light scattering," *Langmuir*, **26** [13], 10524-31 (2010).
88. W. Haertl, C. Beck, M. Roth, F. Meyer, and R. Hempelmann, "Nanocrystalline metals and oxides II: reverse microemulsions," *Phys. Chem. Chem. Phys.*, **101** [11], 1714-7 (1997).
89. M.P. Pileni, "Nanosized particles made in colloidal assemblies," *Langmuir*, **13** [13], 3266-76 (1997).
90. M.P. Pileni, J. Tanori, and A. Filankembo, "Biomimetic strategies for the control of size, shape and self- organization of nanoparticles," *Colloids Surf. A*, **123-124**, 561-73 (1997).

91. V. Chhabra, M. Lal, A.N. Maitra, and P. Ayyub, "Preparation of ultrafine high density gamma ferric oxide using aerosol OT microemulsions and its characterization," *Colloid Polym. Sci.*, **273** [10], 939-46 (1995).
92. D. Ingert and M.-P. Pileni, "Limitations in producing nanocrystals using reverse micelles as nanoreactors," *Adv. Funct. Mater.*, **11** [2], 136-9 (2001).
93. T. Kawai, Y. Usui, and K. Kon-No, "Synthesis and growth mechanism of GeO₂ particles in AOT reversed micelles" *Colloids Surf., A*, **149**, 39-47 (1999).
94. A. Gardner, V.R. Vásquez, A. Clifton, and O.A. Graeve, "Molecular dynamics analysis of the AOT/water/isooctane system: Effect of simulation time, initial configuration, and model salts," *Fluid Phase Equilib.*, **262** [1-2], 264-70 (2007).
95. X. Chen, Q. Cai, J. Zhang, Z. Chen, W. Wang, Z. Wu, and Z. Wu, "Synthesis and growth of germanium oxide nanoparticles in AOT reversed micelle," *Mater. Lett.*, **61** [2], 535-7 (2007).
96. V.C. Manjari Lal, Pushan Ayyub, Amarnath Maitra, "Preparation and characterization of ultrafine TiO₂ particles in reverse micelles by hydrolysis of titanium di-ethylhexyl sulfosuccinate," *J. Mater. Res.*, **13** [5], 1249-54 (1998).
97. S. Li, L. Liu, V.T. John, C.J. O'Connor, and V.G. Harris, "Cobalt-ferrite nanoparticles: Correlations between synthesis procedures, structural characteristics and magnetic properties," *IEEE Trans. Magn.*, **37**, 2350-2 (2001).
98. W. Sun, L. Xu, Y. Chu, and W. Shi, "Controllable synthesis, characterization and catalytic properties of WO₃/ZrO₂ mixed oxides nanoparticles," *J. Colloid Interface Sci.*, **266** [1], 99-106 (2003).
99. J.C. Linehan, J.G. Darab, D.W. Matson, and J.L. Fulton, "High yield reverse micelle synthesis of catalysts and catalyst precursors" *Adv. Tech. Catal. Prep.*, **40**, 91-2 (1995).
100. H. Singh and O.A. Graeve, "Reverse micelle synthesis of zirconia powders: The use of hydrogen peroxide as washing solvent," *Mater. Res. Soc. Symp. Proc.*, **879**, 233-8 (2005).
101. S.A. Morrison, C.L. Cahill, E.E. Carpenter, and V.G. Harris, "Production scaleup of reverse micelle synthesis," *Ind. Eng. Chem. Res.*, **45** [3], 1217-20 (2006).
102. G. Bernard-Granger, N. Monchalín, and C. Guizard, "Comparisons of grain size-density trajectory during spark plasma sintering and hot-pressing of zirconia," *Mater. Lett.*, **62** [30], 4555-8 (2008).
103. Z.A. Munir, D.V. Quach, and M. Ohyanagi, "Electric current activation of sintering: A review of the pulsed electric current sintering process," *J. Am. Ceram. Soc.*, **94** [1], 1-19 (2011).

104. F. Guillard, A. Allemand, J.D. Lulewicz, and J. Galy, "Densification of SiC by SPS-effects of time, temperature and pressure," *J. Eur. Ceram. Soc.*, **27** [7], 2725-8 (2007).
105. R. Chaim and Z. Shen, "Grain size control by pressure application regime during spark plasma sintering of Nd-YAG nanopowders," *J. Mater. Sci.*, **43** [14], 5023-7 (2008).
106. Y. Makino, M. Sakaguchi, J. Terada, and K. Akamatsu, "Consolidation of ultrafine alumina powders with SPS method," *Funtai Oyobi Fummatsu Yakin*, **54** [4], 219-25 (2007).
107. D.V. Quach, H. Avila-Paredes, S. Kim, M. Martin, and Z.A. Munir, "Pressure effects and grain growth kinetics in the consolidation of nanostructured fully stabilized zirconia by pulsed electric current sintering," *Acta Mater.*, **58** [15], 5022-30 (2010).
108. R. Chaim and M. Margulis, "Densification maps for spark plasma sintering of nanocrystalline MgO ceramics," *Mater. Sci. Eng. A*, **407** [1-2], 180-7 (2005).
109. L. Stanciu, V. Kodash, and J. Groza, "Effects of heating rate on densification and grain growth during field-assisted sintering of α -Al₂O₃ and MoSi₂ powders," *Metall. Mater. Trans. A*, **32** [10], 2633-8 (2001).
110. Z. Shen, M. Johnsson, Z. Zhao, and M. Nygren, "Spark plasma sintering of alumina," *J. Am. Ceram. Soc.*, **85** [8], 1921-7 (2002).
111. H.B. Zhang, B.N. Kim, K. Morita, H. Yoshida, J.H. Lim, and K. Hiraga, "Optimization of high-pressure sintering of transparent zirconia with nano-sized grains," *J. Alloys Compd.*, **508** [1], 196-9 (2010).
112. S. Grasso, B.-N. Kim, C. Hu, G. Maizza, and Y. Sakka, "Highly Transparent Pure Alumina Fabricated by High-Pressure Spark Plasma Sintering," *J. Am. Ceram. Soc.*, **93** [9], 2460-2 (2010).
113. B.-N. Kim, K. Hiraga, S. Grasso, K. Morita, H. Yoshida, H. Zhang, and Y. Sakka, "High-pressure spark plasma sintering of MgO-doped transparent alumina," *J. Ceram. Soc. Jpn.*, **120** [1399], 116-8 (2012).
114. K.Q. Dang, S. Takei, M. Kawahara, and M. Nanko, "Pulsed electric current sintering of transparent Cr-doped Al₂O₃," *Ceram. Int.*, **37** [3], 957-63 (2011).
115. M. Stuer, Z. Zhao, U. Aschauer, and P. Bowen, "Transparent polycrystalline alumina using spark plasma sintering: Effect of Mg, Y and La doping," *J. Eur. Ceram. Soc.*, **30** [6], 1335-43 (2010).
116. C. Wang and Z. Zhao, "Transparent polycrystalline ruby ceramic by spark plasma sintering," *Mater. Res. Bull.*, **45** [9], 1127-31 (2010).

117. N. Frage, S. Kalabukhov, N. Sverdlov, V. Ezersky, and M.P. Dariel, "Densification of transparent yttrium aluminum garnet (YAG) by SPS processing," *J. Eur. Ceram. Soc.*, **30** [16], 3331-7 (2010).
118. R. Chaim, R. Marder-Jaeckel, and J.Z. Shen, "Transparent YAG ceramics by surface softening of nanoparticles in spark plasma sintering," *Mater. Sci. Eng. A*, **429** [1-2], 74-8 (2006).
119. R. Chaim, M. Kalina, and J.Z. Shen, "Transparent yttrium aluminum garnet (YAG) ceramics by spark plasma sintering," *J. Eur. Ceram. Soc.*, **27** [11], 3331-7 (2007).
120. G. Bonnefont, G. Fantozzi, S. Trombert, and L. Bonneau, "Fine-grained transparent MgAl₂O₄ spinel obtained by spark plasma sintering of commercially available nanopowders," *Ceram. Int.*, **38** [1], 131-40 (2012).
121. C. Wang and Z. Zhao, "Transparent MgAl₂O₄ ceramic produced by spark plasma sintering," *Scr. Mater.*, **61** [2], 193-6 (2009).
122. Z.Y. Fu, J.F. Liu, H. Wang, D.H. He, and Q.J. Zhang, "Spark plasma sintering of aluminium nitride transparent ceramics," *Mater. Sci. Technol.*, **20** [9], 1097-9 (2004).
123. M. Eriksson, Y. Liu, J. Hu, L. Gao, M. Nygren, and Z. Shen, "Transparent hydroxyapatite ceramics with nanograin structure prepared by high pressure spark plasma sintering at the minimized sintering temperature," *J. Eur. Ceram. Soc.*, **31** [9], 1533-40 (2011).
124. G. Zhang, Y. Wang, Z. Fu, H. Wang, W. Wang, J. Zhang, S.W. Lee, and K. Niihara, "Transparent mullite ceramic from single-phase gel by Spark Plasma Sintering," *J. Eur. Ceram. Soc.*, **29** [13], 2705-11 (2009).
125. L. An, A. Ito, and T. Goto, "Two-step pressure sintering of transparent lutetium oxide by spark plasma sintering," *J. Eur. Ceram. Soc.*, **31** [9], 1597-602 (2011).
126. R. Chaim, Z. Shen, and M. Nygren, "Transparent nanocrystalline MgO by rapid and low-temperature spark plasma sintering," *J. Mater. Res.*, **19** [9], 2527-31 (2004).
127. H. Mingsheng, L. Jianbao, L. Hong, G. Gangfeng, and L. Long, "Fabrication of transparent polycrystalline yttria ceramics by combination of SPS and HIP," *J. Rare Earths*, **24** [1], 222-4 (2006).
128. Z.A.M. Umberto Anselmi-Tamburini, Javier E. Garay, The Regents of the University of California, "Preparation of Dense Nanostructured Functional Oxide Materials with Fine Crystallite Size by Field Activation Sintering," USA Pat. 7601403 B2, 2009.

129. U. Anselmi-Tamburini, J.N. Woolman, and Z.A. Munir, "Transparent Nanometric Cubic and Tetragonal Zirconia Obtained by High-Pressure Pulsed Electric Current Sintering," *Adv. Funct. Mater.*, **17** [16], 3267-73 (2007).
130. "Standard Test Methods for Aparent Porosity, Water Absorption, Aparent Specific Gravity, and Bulk Density of Burned Refractory Brick and Shapes by Boiling Water," ASTM Designation C 20-00. American Society for Testing and Materials, West Conshohocken, PA, 2000.
131. M.S. Kaliszewski and A.H. Heuer, "Alcohol Interaction with Zirconia Powders," *J. Am. Ceram. Soc.*, **73** [6], 1504-9 (1990).
132. S.A. Hassanzadeh-Tabrizi and E. Taheri-Nassaj, "Effects of Milling and Calcination Temperature on the Compressibility and Sinterability of a Nanocrystalline $\text{Al}_2\text{O}_3\text{-Y}_3\text{Al}_5\text{O}_{12}$ Composite Powder," *J. Am. Ceram. Soc.*, **91** [11], 3546-51 (2008).
133. S.L. Jones and C.J. Norman, "Dehydration of Hydrous Zirconia with Methanol," *J. Am. Ceram. Soc.*, **71** [4], C-190-C-1 (1988).